JAEA-Review
2013-057

JAEA-Tokai Tandem Annual Report 2012
April 1, 2012 – March 31, 2013

Department of Research Reactor and Tandem Accelerator

Nuclear Science Research Institute
Tokai Research and Development Center

March 2014

Japan Atomic Energy Agency | 日本原子力研究開発機構

JAEA-Review

本レポートは独立行政法人日本原子力研究開発機構が不定期に発行する成果報告書です。
本レポートの入手並びに著作権利用に関するお問い合わせは、下記あてにお問い合わせ下さい。
なお、本レポートの全文は日本原子力研究開発機構ホームページ（http://www.jaea.go.jp）
より発信されています。

独立行政法人日本原子力研究開発機構　研究技術情報部　研究技術情報課
〒319-1195　茨城県那珂郡東海村白方白根 2 番地 4
電話 029-282-6387, Fax 029-282-5920, E-mail:ird-support@jaea.go.jp

This report is issued irregularly by Japan Atomic Energy Agency.
Inquiries about availability and/or copyright of this report should be addressed to
Intellectual Resources Section, Intellectual Resources Department,
Japan Atomic Energy Agency.
2-4 Shirakata Shirane, Tokai-mura, Naka-gun, Ibaraki-ken 319-1195 Japan
Tel +81-29-282-6387, Fax +81-29-282-5920, E-mail:ird-support@jaea.go.jp

JAEA-Review 2013-057

JAEA-Tokai Tandem Annual Report 2012
April 1, 2012 – March 31, 2013

Department of Research Reactor and Tandem Accelerator

Nuclear Science Research Institute
Tokai Research and Development Center
Japan Atomic Energy Agency
Tokai-mura, Naka-gun, Ibaraki-ken

(Received December 9, 2013)

The JAEA-Tokai tandem accelerator complex has been used in various research fields such as nuclear science and material science by researchers not only of JAEA but also from universities, research institutes and industrial companies. This annual report covers developments of accelerators and research activities carried out using the tandem accelerator and superconducting booster from April 1, 2012 to March 31, 2013. Thirty-one summary reports were categorized into seven research/development fields:

(1) accelerator operation and development
(2) nuclear structure
(3) nuclear reaction
(4) nuclear chemistry
(5) nuclear theory
(6) atomic physics and solid state physics
(7) radiation effects in materials.

This report also lists publications, meetings, personnel, committee members, cooperative researches and common use programs.

Keywords : JAEA-Tokai Tandem Accelerator, Operation Results, Nuclear Structure, Nuclear Reaction, Nuclear Chemistry, Nuclear Theory, Atomic Physics, Solid State Physics, Radiation Effects in Materials, Progress Report

---

Editors: Katsuhisa NISHIO, Kazuaki TSUKADA, Norito ISHIKAWA,
Yosuke TOH, Hiroyuki KOURA and Makoto MATSUDA

JAEA-Review 2013-057

原子力機構東海タンデム加速器 2012 年度年次報告

日本原子力研究開発機構
東海研究開発センター原子力科学研究所
研究炉加速器管理部

(2013 年 12 月 9 日受理)

原子力機構東海タンデム加速器施設は、原子核科学や物質科学などの様々な分野において、原子力機構を始めとして、大学や公立研究機関、民間企業に利用されている。本年次報告書は、タンデム加速器およびブースター加速器を利用し、2012 年 4 月 1 日から 2013 年 3 月 31 日までの期間に実施された研究活動の英文要約をまとめたものである。総数 31 件の要約を下記の 7 部門に分類した。

（1）加速器の運転状況と開発
（2）原子核構造
（3）原子核反応
（4）核化学
（5）原子核理論
（6）原子物理及び固体物理
（7）材料の照射効果

また、発表論文と会議での口頭発表、タンデム加速器に関与した職員、タンデム加速器専門部会委員、大学等との共同研究課題、及び施設共用課題のリストを掲載した。

原子力科学研究所：〒319-1195　茨城県那珂郡東海村白方白根 2-4
編集者：西尾　勝久、塚田　和明、石川　法人、藤　暢輔、小浦　寛之、松田　誠

Foreword

This report covers research and development activities with the tandem accelerator and its superconducting booster at JAEA Tokai, for the period of FY 2012 (April 1, 2012 to March 31, 2013). The tandem accelerator was operated over a total of 113 days and delivered 20 different ion beams to experiments in the fields of nuclear physics, nuclear chemistry, atomic physics, solid state physics and radiation effects in materials. Thirty-five research programs were carried out in collaboration with a total of about 110 researchers from universities and research institutes. The tandem accelerator building cracked in the 2011 off the pacific coast of Tohoku Earthquake was repaired over about four months.

The following are the highlights in FY 2012:
In the field of accelerator development: The acceleration of the dual beam is successfully performed by the tandem accelerator in which an ECR ion source is mounted at the high voltage terminal. And the real-time RBS measurement of the heavy ion irradiation effect was performed using the dual beam which consist of 165MeV $^{132}Xe^{11+}$ ions and 15MeV $^{12}C^{+}$ ions.

In the field of nuclear structure: Alpha-gamma coincidence measurement for ^{261}Db has been carried out to establish the ground-state configuration of Db isotopes. The nucleus ^{261}Db was produced in the $^{248}Cm(^{19}F,6n)^{261}Db$ reaction. An α peak that should correspond to the α decay of ^{261}Db and several γ-rays in coincidence with the α particles were observed.

In the field of nuclear reactions: Multi-nucleon transfer induced fission was used to measure the fission fragment mass distributions and their dependence on the excitation energy of compound nucleus. In the reaction of $^{18}O + ^{238}U$, it was shown that data for more than 10 actinide nuclei were obtained in a single measurement.

In the field of nuclear chemistry: Medical use of RIs were produced at the tandem accelerator for diagnostic imaging studies and therapeutic applications. ^{95m}Tc emitting high energy gamma-rays is required for the development of the Compton camera which can realize high position resolution. ^{211}At has also been actively investigated as a promising α-emitter for cancer therapy.

In the field of nuclear theory: The evolution of the shell structure in antimony (Z=51) isotopes is studied under a shell model framework in the full $50 \leq Z \leq 82$ and $0 \leq N \leq 82$ valence space. Considering the nuclear tensor force, the energy levels of $5/2^{+}_{1}$, $7/2^{+}_{1}$, and $11/2^{-}_{1}$ were evaluated, and it reproduces well experimental trends. Furthermore, an existence of doubly-magic nuclei is predicted in the extremely superheavy nuclear mass region from spherical single-particle levels under one-particle mean-field potential. In the framework, we found that ^{298}Fl (Z=114) and ^{472}[164] are the possible doubly-magic nuclei which are stable against the beta-decay.

In the field of atomic physics and solid-state physics: The electron yields of convoy electron, Coster-Kronig transition, and binary electron for C_2^+ are compared with that for C^+ ion with same velocity. The cluster effect for the convoy electron yield is 4.3, which does not agree with the linearity reported for 0.5 MeV/atom C_n^+ ions. It is suggested that this value stems from both cluster effect and electron loss from projectile ion, because of rather thin carbon foil thickness.

In the field of radiation effects in materials: Recent development of scanning transmission electron microscope (STEM) enables us to characterize detailed defect structure of ion-irradiated ceramics, such as CeO_2 and Si_3N_4. The results for CeO_2 clearly show that the oxygen sublattice at the core of the damage region (2-3 nm ion-track region) is significantly disordered. The results for Si_3N_4 show that the density in the ion-track region is small relative to that in the matrix, while the peripheral of the ion-track region has slightly high density.

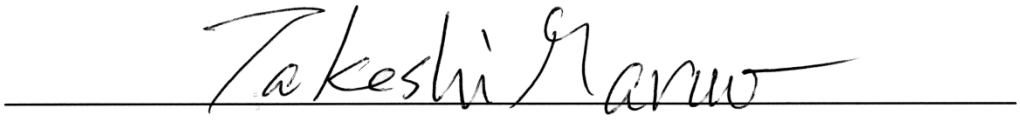

Takeshi MARUO, Director, Department of Research Reactor and Tandem Accelerator

Contents

目　　次

CHAPTER 1

Accelerator Operation and Development

This is a blank page.

1.1 Operation and usage of tandem accelerator and booster

A. Osa[1], S. Hanashima[1], S. Abe[1], T. Ishii[1], N. Ishizaki[1], H. Tayama[1], M. Matsuda[1],
T. Nakanoya[1], H. Kabumoto[1], M. Nakamura[1], K. Kutsukake[1], Y. Otokawa[1] and T. Asozu[1]

The tandem accelerator and booster were operated for experiments in the first half of FY (from April, 2012 to June) and in the second half of FY (from October to March, 2013). From November, 2012 to February, 2013, we repaired the tandem accelerator buildings from damages of the 2011 off the pacific coast of Tohoku Earthquake on March 11, 2011.

The total operation time of the tandem accelerator for FY2012 (from April 1, 2012 to March 31, 2012) was 113 days and 20 different beams were delivered for experiments. The experimental proposal for FY2013 and the usage of the beam times for FY2012 are summarized in Table 1 and Table 2, respectively.

Table 1. Experimental proposals.

Research proposals accepted by the program advisory committee:	
In-house staff proposals	6
Collaboration proposals	20
Number of experiments proposed	35
Total number of scientists participating in research	
from outside	108
in-house	43
Number of institutions presented	32

Table 2. Usage of beam-times in different research fields.

Research field		Beam time (days)	(%)
Nuclear physics		29	25.7
Nuclear chemistry		27	23.9
Atomic and materials sciences		36	31.9
Accelerator development		20	17.7
Industrial use		1	0.9
	total	113	100

Distributions of the terminal voltages and ion species for experiments are shown in Figure 1 and Figure 2, respectively. Half of the beams were extracted from three negative ion sources, SNICS-2. The proton, carbon, nitrogen, oxygen and rare gases were ionized and extracted from in-terminal ECR ion source (TIS). The ECR ion source was used as much as 48% of all the beam time.

The superconducting booster was operated for a total of 4 days to boost the energies of ^{90}Zr beams from the tandem accelerator, as is summarized in Table 3. These beams were used for experiments of nuclear physics.

[1] Japan Atomic Energy Agency (JAEA)

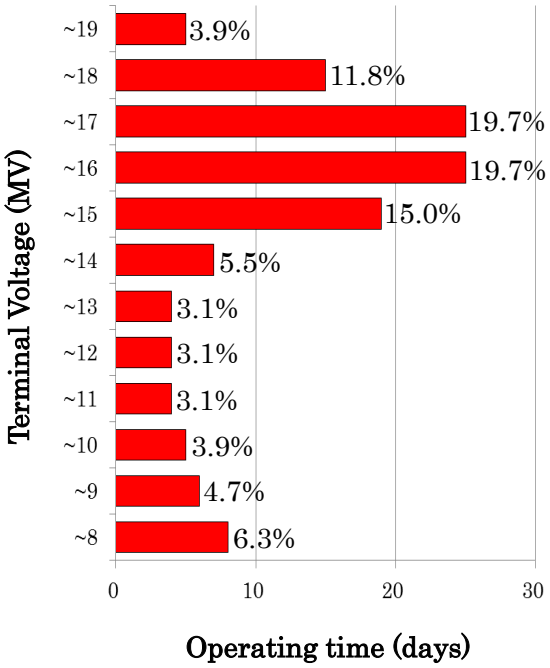

Fig. 1 Distribution of terminal voltages.

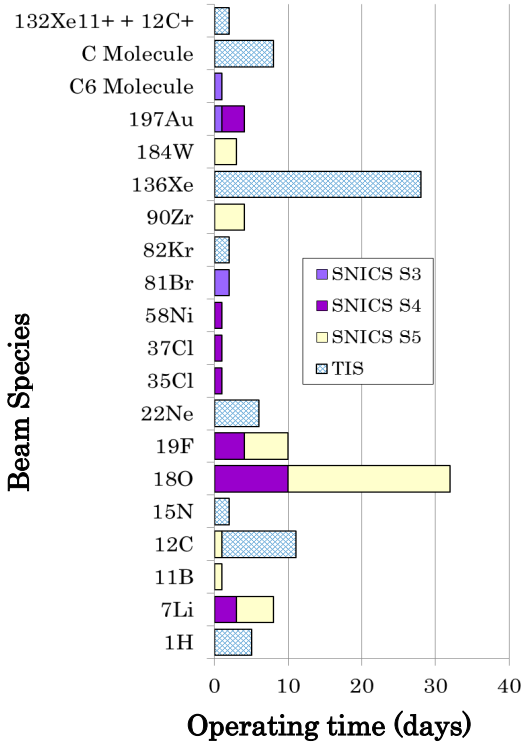

Fig. 2 Distribution of beam species accelerated for experiments.

Table 3. Boosted ion beams for experiments.

Beam species	Boosted energies (MeV)	Beam time (days)
^{90}Zr	354,420	4

1.2 Development of dual-beam system using an electrostatic accelerator

M. Matsuda[1] , T. Asozu[1] , M. Sataka[1] and A. Iwase[2]

We have developed the dual beam system which accelerates two kinds of ion beams simultaneously. The acceleration of the dual beam is performed by the tandem accelerator in which an ECR ion source is mounted at the high voltage terminal [1,2]. The multi-charged ions of two or more elements can be simultaneously generated from the ECR ion source, so dual-beam irradiation is achieved by accelerating ions with the same charge to mass ratio (for example, $^{132}Xe^{11+}$ and $^{12}C^{+}$).

The acceleration test was performed using the ions of $^{12}C^{+}$ and $^{132}Xe^{11+}$. Acceleration voltage was 15 MV and the energies of these ions were 15 MeV and 165 MeV, respectively. These beams were guided to L2 beam line of tandem accelerator facility. In the L2 beam line, the quartz plate for a beam viewer is located to 4.5 m downstream of magnetic quadrupole triplet (MQT) lens, and the target was installed at 1.1 m further downstream position. The beam profile observed by the beam viewer is shown in Fig. 1(center). It is found that the ion beam is separated into two components completely. Although the ions with same charge to mass ratio are transported through the same orbit, there is a slight difference in the ratio. The difference is about 0.07% between $^{12}C^{+}$ and $^{132}Xe^{11+}$. This difference caused the orbital difference at the viewer position. In order to observe the beam profile of ^{12}C and ^{132}Xe ion at a target position, Rutherford-Back-Scattering (RBS) analysis was performed while moving an inclined Au strip line across a beam cross section. We prepared an evaporated Au strip on Si substrate whose thickness and width are 300 nm and 1 mm, respectively. Silicon charged particle detector was set in 135 degrees to the beam axis. The beam profiles and beam intensities of both ions are obtained from the area of the scattering peak of ^{12}C and ^{132}Xe, and the position of a strip line corresponding to the obtained RBS spectrum. The beam profile at the target position acquired by this method is shown in Fig. 1. Separation of the beam position occurred mainly due to the energy analyzing magnet and the switching magnet of the tandem accelerator. In order to irradiate the same position, both beams were scanned with a beam scanning magnet. Horizontal(X) and vertical(Y) beam scanning magnet is installed in the 1.8 m downstream of MQT. Scanning frequency was 11.3 Hz in X direction and 90.9 Hz in Y direction. Such scanning enables us to irradiate a target uniformly. Both scanning width were 10 mm at the target position. An aperture of ϕ3 mm was installed at 0.6 m upper stream from the target. The beam which passed through the aperture was irradiated to the target.

The real-time measurement of the heavy ion irradiation effect was performed using the dual beam formed as mentioned above. We studied the atomic mixing at metal/oxide interfaces under swift heavy ion irradiation. Bismuth film on Al_2O_3 crystalline substrate was prepared by vapor deposition. The thickness of the evaporated layer was 300nm. Xe ions with the energy of 165 MeV were irradiated Bi-Al_2O_3 specimen and 15 MeV C ions were simultaneously irradiated for RBS analysis. Both of the beam currents of Xe and

[1] Japan Atomic Energy Agency
[2] Osaka Prefecture University

C ion were about 1 pnA (particle nano ampere). That is, both fluences for 10 minutes were estimated to be about $5x10^{12}$ ions/cm^2. These ion beams were simultaneously irradiated over 1 hour. RBS spectra were acquired every 10 minutes during the irradiation.

Obtained RBS spectra are shown in Fig. 2. It is found that Bi peaks of RBS spectra broadened to low energy side with the increase in the ion dose. In other words, part of the Bi atoms moved toward a deeper region of Al_2O_3. This result implies that the atomic mixing at Bi-Al_2O_3 interface was induced by swift heavy ion [3]. We also confirmed that no spectrum broadening occurred by C ion irradiation alone. Electronic stopping powers of 165 MeV Xe and 15 MeV C are 22 MeV/μm and 1.6 MeV/μm, respectively. It is possible that the energy elastically deposits by Xe ions into specimen. The estimated nuclear stopping power of C ion is one percent or less compared to Xe ion. We can conclude that the ion beam mixing at Bi-Al_2O_3 interface was induced with Xe irradiation by electronic excitation effect.

Using the dual beam of Xe and C ions, real-time analysis of the radiation effects was successfully performed. With this method developed here, the dose dependency of the effects due to heavy ion irradiation can be measured in detail by using only one sample. It is shown that the dual beam is useful for real-time ion beam analysis of the radiation effects study.

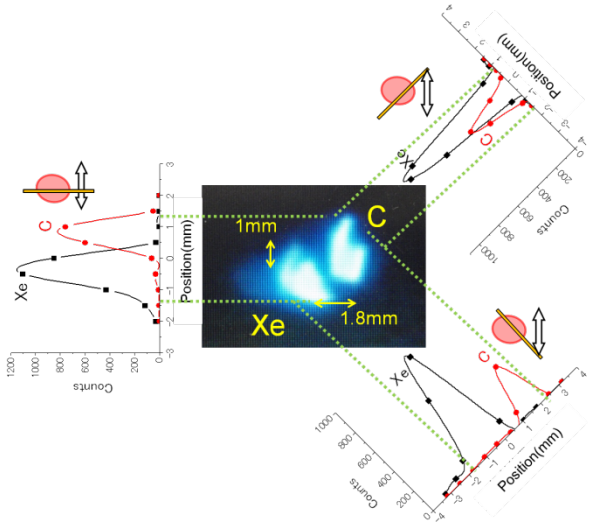

Fig. 1 Beam profile of the dual beam at a target position.

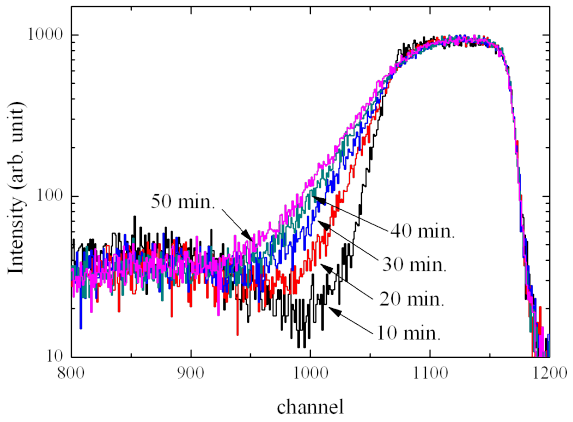

Fig. 2 Change in RBS spectra for Bi(300nm)-Al_2O_3 system by simultaneous irradiation with the dual beam.

References

[1] M. Matsuda et al., J. Phys. Conf. Series 163 (2009) 012112.
[2] M. Matsuda et al., Nucl. Instr. and Meth. A654 (2011) p.45.
[3] R. Nakatani et al., Nucl. Instr. and Meth. B230 (2005) p.234.

1.3 Acceleration response of the building of tandem accelerator in the earthquake "The 2011 off the Pacific coast of Tohoku Earthquake"

T. Asozu[1]

The JAEA-Tokai tandem accelerator has two triaxial accelerographs. They are installed on the top floor (8F) and the bottom floor (B2F) of the building. They measure acceleration response and record wave profiles of the directions; North-South (NS), East-West (EW), Down-Up (DU). A recording starts when they detect acceleration of over 5gal and goes on for 90 sec. We analyzed the acceleration wave profiles in the earthquake "The 2011 off the Pacific coast of Tohoku Earthquake" and researched the resistance of the building of the tandem accelerator.

1. The acceleration wave profiles of each floor

Figure 1 shows the acceleration wave profiles of main quake. The maximum acceleration is about 930 gal on the 8F and is about 220 gal on the B2F. Both of them are found in the waves of NS direction and at about 70 sec from the starting points. The maximum peaks in each direction are found at approximately the same time on the 8F. Their vector sum reaches 1000 gal which was over gravity acceleration. On the 8F, the wave's frequency is 2.8 Hz around the maximum peak. The maximum displacement is 6.5 cm in the direction of NS, which was calculated by integrating one period of the wave.

2. Frequency analysis

Figure 2 shows the acceleration response spectra whose analyzing range is 60 sec to 96 sec in Fig.1 and the sampling number is 4096. On the B2F, the main frequency is 2 Hz. On the other hand, there are 3 large peaks in the spectrum of 8F-NS, which are natural frequencies of the building. The frequencies are 2.8 Hz, 11 Hz and 20 Hz. If the natural frequency of the building was match lower, resonance had inflicted heavy damages. The lowest natural frequency of 2.8 Hz is high for this building whose floor space is 15 m × 15 m and height is 30 m. It is generally for a residence building with reinforced concrete which has a floor space of 30 m × 30 m and the same height. The highness of the frequency indicates the high resistance for earthquake. It is due to the thick radiation shielding walls of the tandem accelerator which are 1.3 m for upper from fifth floor and 1.5 m for lower than that.

References

[1] M. Takeuchi et al., Summaries of technical papers of annual meeting Architectural Institute of Japan, Structural and Construction Engineering 44 (1969) pp.653-654.

[1] Japan Atomic Energy Agency (JAEA)

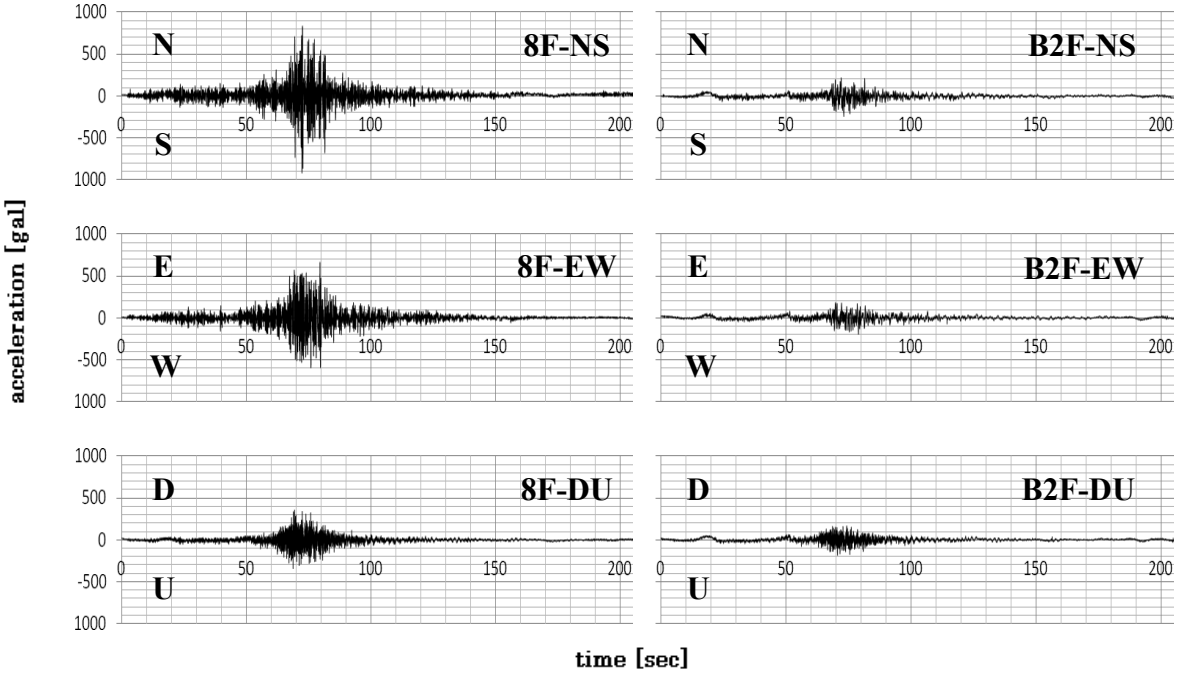

Fig.1 Acceleration wave profiles of the main quake.

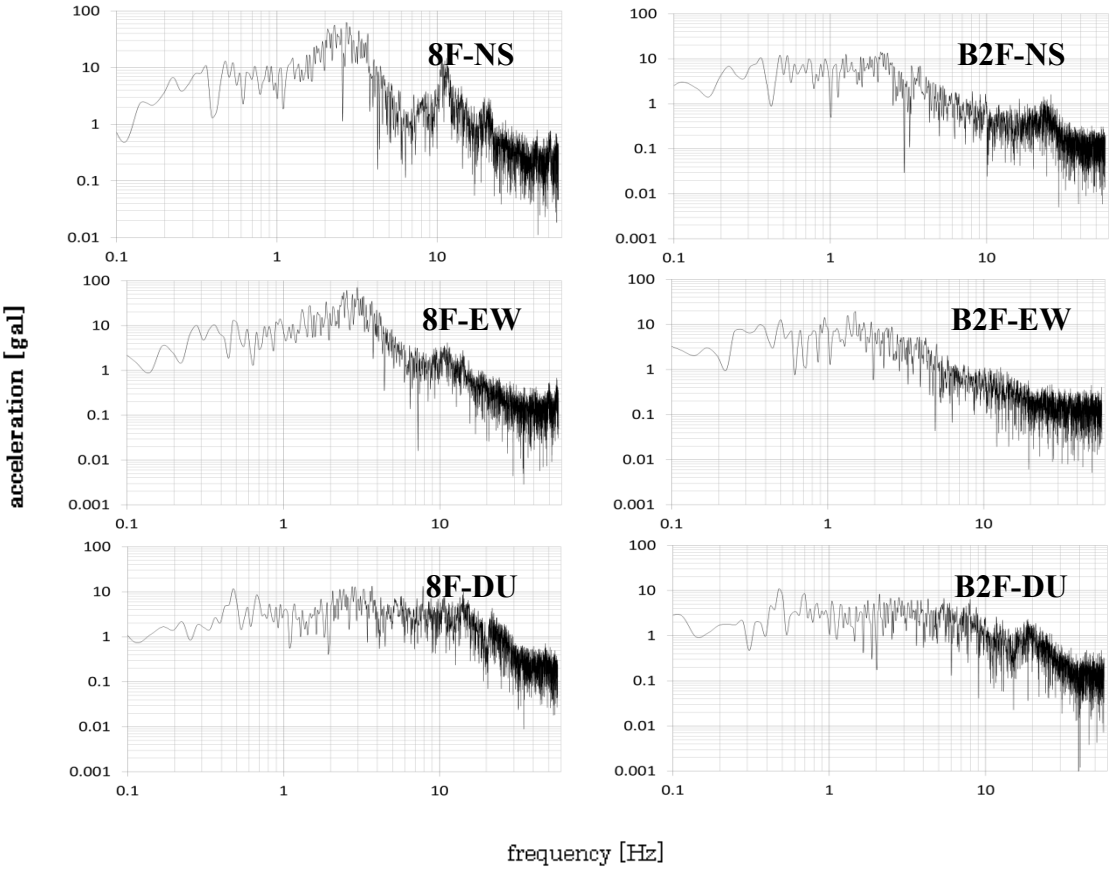

Fig.2 Acceleration response spectra
(the range is from 60sec to 96sec in Fig.1, the sampling number is 4096).

CHAPTER 2

Nuclear Structure

This is a blank page.

2.1 Alpha-gamma coincidence measurement for ^{261}Db

M. Asai[1], K. Tsukada[1], N. Sato[1], T.K. Sato[1], A. Toyoshima[1], S. Miyashita[1,2], K. Ooe[1,3], Y. Kaneya[1], T. Ishii[1], Y. Nagame[1] and M. Schädel[1]

The limit of existence of the heaviest elements essentially depends on nuclear shell structure. Theoretical calculations predict that the proton and neutron closed shells should appear at $Z = 114 \sim 126$ and $N \approx 184$ [1], which stabilizes the nucleus against fission and makes relatively-stable superheavy nuclei. Recent progress in experimental techniques has enabled us to approach this superheavy element region. However, our knowledge on the shell structure of superheavy nuclei is still very limited because of lack of experimental data. One of the most sensitive probes to clarify the shell structure are energy spacings and the order of proton and neutron single-particle orbitals. Thus, to unravel these features, spectroscopic studies for superheavy nuclei are highly desired. It is expected that three proton orbitals $7/2^-[514]$, $1/2^-[521]$, and $9/2^+[624]$ are lying closely around the Fermi surface in $Z = 101$, 103, and 105 isotopes [1]. The ground-state configurations of $Z = 101$ (Md) isotopes are known to be $7/2^-[514]$ which was established through α-decay spectroscopy [2]. Those of $Z = 103$ (Lr) isotopes are found to be either $7/2^-[514]$ or $1/2^-[521]$ depending on the isotopes [3]. The next proton orbital $9/2^+[624]$ is thus expected to become the ground state in $Z = 105$ (Db) isotopes, although there is no experimental data for Db isotopes. To establish the ground-state configuration of Db isotopes, we have carried out α-γ coincidence measurement for ^{261}Db.

The nucleus ^{261}Db was produced in the ^{248}Cm(^{19}F,6n)^{261}Db reaction. The beam energy was 113 MeV on target, and the average beam intensity was 0.6-particle μA. Reaction products recoiling out of the target were thermalized in He gas, transported through a 25-m long capillary with a He/KCl aerosol jet into a rotating-wheel α-γ detection system, and deposited on a set of 40 thin catcher foil mounted on the wheel. The wheel periodically rotated at 4.0-s intervals to move the deposited sources to two consecutive detector stations each of which was equipped with two Si detectors and two Ge detectors. Alpha-singles and α-γ coincidence events were recorded event by event together with time information. Details of the experimental setup are given in Ref. [4,5].

Figure 1 shows an α energy spectrum observed with the Si detector located at the first detector station. A small α peak was observed at 8930 keV, which exhibited a short half-life of < 4 s. This α peak should correspond to the α decay of ^{261}Db. The α-α time correlation analysis also showed the existence of the correlated α-α events between ^{261}Db and its daughter ^{257}Lr. We accumulated a total beam dose of 2.1×10^{18}, and observed approximately 40 α events of ^{261}Db. Several γ-ray events were also observed in coincidence with the α particles of ^{261}Db. To get a better statistics, we plan to continue this measurement.

[1] Japan Atomic Energy Agency
[2] Hiroshima University
[3] Niigata University

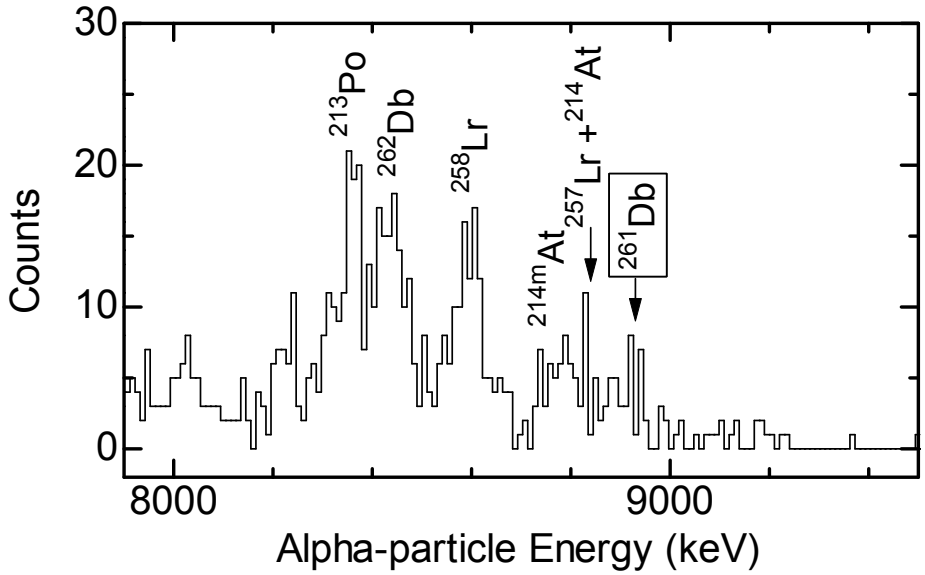

Fig. 1 α energy spectrum observed with the Si detector located at the first detector station.

References

[1] A. Sobiczewski and K. Pomorski, Prog. Part. Nucl. Phys., 58 (2007) p.292.

[2] F. P. Heßberger et al., Eur. Phys. J. A, 26 (2005) p.233.

[3] A. Chatillon et al., Eur. Phys. J. A, 30 (2006) p.397

; M. Asai et al., RIKEN Acc. Prog. Rep., 43 (2010) ix.

[4] M. Asai et al., Phys. Rev. Lett., 95 (2005) 102502.

[5] M. Asai et al., Phys. Rev., C 83 (2011) 014315.

2.2 Study of high-spin states in ^{35}S

S. Go[1], E. Ideguchi[2], R. Yokoyama[1], M. Kobayashi[1], K. Kisamori[1], S. Michimasa[1], S. Shimoura[1], M. Sugawara[3], M. Koizumi[4], Y. Toh[4], T. Shizuma[4], A. Kimura[4], H. Harada[4], K. Furutaka[4], S. Nakamura[4], F. Kitatani[4] and Y. Hatsukawa[4]

After the finding of superdeformed (SD) band in ^{152}Dy [1], SD structures in various mass regions have been systematically studied. Recently SD rotational bands in mass A ~ 40 region have been discovered in ^{36}Ar [2], ^{40}Ar [3], ^{40}Ca [4]. The occurrence of SD structures in this region was related to the existence of large energy gaps of deformed single particle energies. Woods-Saxon single particle diagram (see Fig. 4 of Ref [4]) shows the gaps at $\beta_2 \sim 0.5$ in Z = 18 and $\beta_2 \sim 0.6$ in Z = 20. The diagram also shows the candidate of the SD nuclei, $\beta_2 \sim 0.6$ in Z = 16. The existence of the SD band in ^{32}S (Z = 16) was predicted for a long time [5], but the SD structure has not been observed yet. Neutron-rich sulfur isotopes were also predicted as the candidate of SD nuclei by Skyrme-Hartree-Fock calculation and the SD local minimum in ^{36}S results from the combination of the gaps at Z = 16 and N = 20 [6]. Accordingly, the high-spin study of the neutron-rich sulfur isotopes has the importance to clarify the SD structure in Z = 16. In ^{35}S, the high-spin excited levels up to 7.18 MeV were found and the multipolarities of each gamma-ray transition were studied in our previous experiments [7, 8]. In order to find optimal beam energy and to investigate high-spin states in ^{35}S, an excitation function measurement was performed at the tandem accelerator facility of Japan Atomic Energy Agency (JAEA).

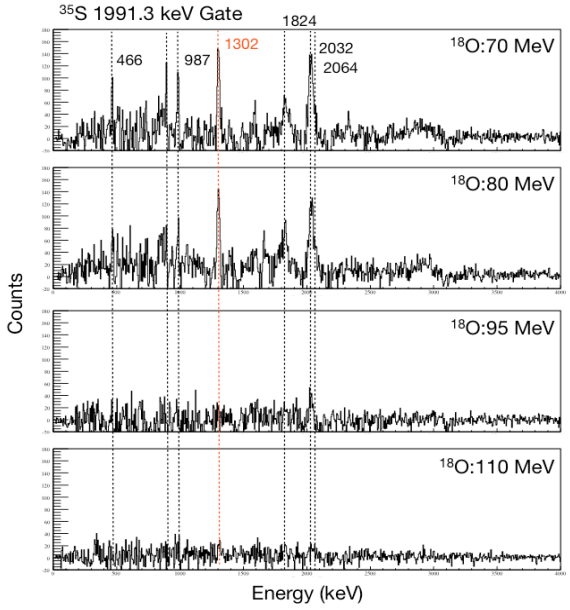

Fig. 1 Gamma-ray spectra gating the 1991 keV transition in ^{35}S were labeled.

High-spin states of ^{35}S was produced by the fusion evaporation reaction ^{26}Mg(^{18}O, 2α1n)^{35}S at ^{18}O beam energy of 70, 80, 95 and 110 MeV. A thin ^{26}Mg self-support target was used and fusion products go through the target. Gamma rays were measured by the GEMINI-Ⅱ array [9] with the BGO Compton suppressor shield. The 14 detectors were placed at 5 different angles, 47° (4 Ge's), 72° (2 Ge's), 90° (2 Ge's), 105° (4 Ge's) and 147° (2 Ge's). The ΔE of charged particles from compound nuclei were measured by the Si-Ball [10], a 4π array consisting of 11 Si detectors of 170 μm thickness. The most forward Si detector was segmented into 5 sections and the second forward

[1]Center for Nuclear Study , University of Tokyo (CNS)
[2]Research Center for Nuclear Physics, Osaka University (RCNP)
[3]Chiba Institute of Technology, Faculty of Information and Computer Science
[4]Japan Atomic Energy Agency (JAEA)

detectors were segmented into 2 sections. Total 20 channels were used to select the multi-charged evaporation channels.

Gamma-ray spectra were obtained by correcting the Doppler effect and gamma-gamma-coincidence analysis has been performed (See Fig. 1). By gating the lowest transition related to ^{35}S of 1991 keV [11], the transitions reported in the previous study [7,8] were observed in the case of ^{18}O beam energy at 70 and 80 MeV. The transitions related to ^{35}S were not clearly observed in 95 and 110 MeV. It indicates the cross section of ^{35}S goes down rapidly from 80 to 110 MeV. The transition of 1302 keV from the level of 7.18 MeV was assigned as the highest transition in our previous study [7, 8]. Table. 1 shows the relative intensities of transition of 1302 keV for each transition. The relative intensities of the 1302 keV for 1824 keV transition were 1.10(28) and 1.30(52) in 70 and 80 MeV beam energy although the intensities at higher excited energy, 5.9 MeV, were 5.3(13) and 6.8(0.9). There was small difference in the relative intensity at 3.8 MeV. In contrast, the intensities at higher excited energy were larger at 80 MeV beam energy. This result implies the excited states above 7.18 MeV were more produced in the case of 80 MeV beam energy. For this reason, the ^{18}O beam energy at 80 MeV is selected to excite the high-spin states of ^{35}S in the ^{26}Mg(^{18}O, 2α1n)^{35}S reaction.

Table. 1 Relative intensities of 1302 keV for each transition. Excited levels are shown as E_{ex}.

Beam Energy (MeV)	Relative Intensity (1302/1824) E_{ex}=3.8 MeV	(1302/987) E_{ex}=5.0 MeV	(1302/466) E_{ex}=5.9 MeV
70	1.10(28)	2.15(35)	5.3(1.3)
80	1.30(52)	2.39(40)	6.8(0.9)

References

[1] P. J. Twin et al., Phys. Rev. Lett. 57 (1986) 7, pp.811-814.
[2] C. E. Swensson et al., Phys. Lett. 85 (2000) 13, pp.2693-2696.
[3] E. Ideguchi et al., Phys. Lett., B 686 (2010) pp.18-22.
[4] E. Ideguchi et al., Phys, Rev. Lett. 87 (2001) 22, 222501.
[5] I. Ragnarsson et al., Phys. Rep. 45 (1987) pp.1-87.
[6] T. Inakura et al., Nucl. Phys., A 728 (2003) pp.52-64.
[7] E. Ideguchi et al., CNS Ann. Rep. 2009 (2010) pp.23-24.
[8] E. Ideguchi et al., CNS Ann. Rep. 2010 (2011) pp.5-6.
[9] M. Oshima et al., J. Radioanal. Nucl. Chem. 278 (2008) pp.257-262.
[10] T. Kuroyanagi et al., Nucl. Instrum. Methods Phys. Res., A 316 (1992) pp.289-296.
[11] A. Guichard et al., Phys. Rev., C 12 (1975) pp.1109-1117.

CHAPTER 3

Nuclear Reaction

This is a blank page.

3.1 Measurement of fission fragment mass distributions of compound nuclei populated by multi-nucleon transfer reaction in $^{18}O + ^{238}U$

K. Nishio[1], K. Hirose[1], T. Nagayama[1,2], H. Makii[1], I. Nishinaka[1], S. Ota[1], T. Ishii[1], K. Tsukada[1], M. Asai[1], S. Chiba[3], T. Ohtsuki[4], S. Araki[5] and Y. Watanabe[5]

Mass distributions of fission fragments for neutron induced fissions of actinide nuclei are the important nuclear data for atomic energy applications. In nuclear reactors with highly burned nuclear fuels and next generation fast breeder reactors, it is necessary to consider fission of minor actinides with relatively short half-lives. Delayed neutron yields are also one of the important data, because it will influence the reactor response. The delayed neutron yield is sensitive to the fission fragment mass and charge distributions. In this experimental program, we are promoting the measurement of the fission fragment mass distributions for short-lived actinide nuclei, whose data for neutron-induced fissions are practically impossible to take. We use multi-nucleon transfer reactions to populate the excited compound nuclei using an ^{18}O beam and an available actinide target.

Fission properties of excited compound nuclei populated in the multi-nucleon transfer reaction $^{18}O + ^{238}U$ were measured. The experiment was carried out at the JAEA tandem accelerator. Energy of the ^{18}O beam was 157.5 MeV. Projectile-like nucleus produced in multi-nucleon transfer reaction was identified using silicon ΔE-E detectors, and its energy was measured to assign the excitation energy of the compound nucleus. Two fission fragments were detected by position-sensitive multiwire-proportional counters (MWPCs). Time difference between the two MWPCs was recorded. Fission fragment masses were determined with the kinematic consideration by refereeing the velocity and the direction of recoiled fissioning nuclei which were determined by detecting the projectile-like nucleus.

Figure 1 shows the fission events of $^{239}Np^*$ as a function of fragment mass and excitation energy of the compound nucleus. A transition from asymmetric to symmetric fission toward high excitation energy is seen. Similar data for $^{237,238,239,240}U^*$, $^{240,241,242}Np^*$, and $^{241,242,243,244}Pu^*$ were obtained in a single measurement.

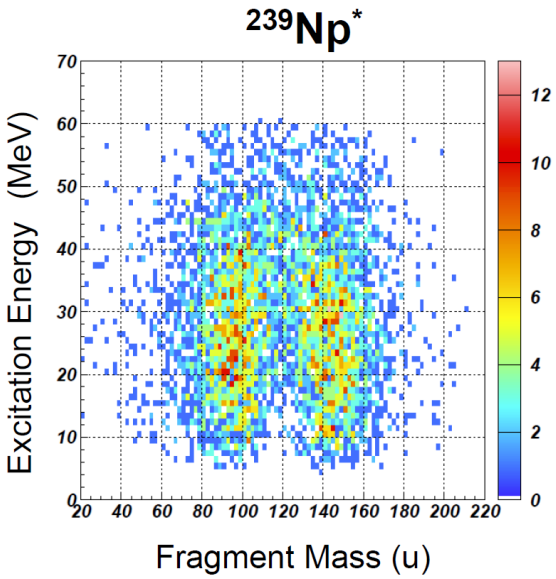

Fig. 1 Fission events of $^{239}Np^*$ as a function of the fragment mass and the excitation energy of the compound nucleus.

[1] Japan Atomic Energy Agency (JAEA)
[2] Ibaraki University
[3] Tokyo Institute of Technology
[4] Tohoku University
[5] Kyushu University

3.2 Energy and angular distributions of ^{16}O particles from ^{155}Gd(^{18}O, ^{16}O)^{157}Gd two-neutron transfer reaction

H. Makii[1], T. Ishii[1], S. Ota[1], K. Nishio[1], I. Nishinaka[1], S. Chiba[2], M. Asai[1], K. Furutaka[1] and S. Mitsuoka[1]

Neutron-capture [hereafter (n,γ)] cross sections of unstable nuclei play an important role in stellar nucleosynthesis. In the nucleosynthesis by slow neutron capture process (s-process) half lives of some unstable nuclei are long lived that the (n,γ) reactions can be competing with β-decay. Such long-lived nuclei act as branching points in the reaction path of the s-process. In order to understand the stellar conditions for the s-process nucleosynthesis, (n,γ) reaction cross sections of unstable nuclei over a wide stellar temperature range ($kT \approx 8 \sim 90$ keV) are required [1]. In addition (n,γ) cross sections of long-lived fission products (LLFPs) are the most important physical quantities for the study on transmutation of nuclear wastes. However, the measurement of the (n,γ) cross sections of unstable nuclei is very difficult. The main reasons for the difficulty are due to sample preparation and/or radioactivity of the sample. These difficulties can be overcome with the surrogate method, which aims at determining reaction cross sections for compound-nuclear reaction on the basis of the assumption that the formation and decay of a compound nucleus are independent of each other [2].

Recently, we have been developing an experimental apparatus for the surrogate method to determine (n,γ) cross sections by means of multinucleon transfer reactions with heavy-ion projectiles, such as (^{18}O, ^{16}O) two-neutron transfer reaction. The surrogate method using the multinucleon transfer reactions has an advantage to obtain experimental data corresponding to a wide variety of reactions in one experimental setup; e.g., when one bombard Gd targets with ^{18}O beams, one can observe various isotopes of O, F, N and C, which correspond to the populations of series of Gd, Eu, Tb, and Dy isotopes as compound nuclei [3]. In addition, it is well known that the angular distribution of the heavy-ion-induced transfer reactions at energies above the Coulomb barrier is expected to have a peak around the grazing angle θ_{gr}. This angular distribution gives a clear criterion for the scattering angle to be measured [4]. In the present study, we have measured the energy and angular distributions of outgoing ^{16}O particles from ^{155}Gd(^{18}O, ^{16}O) two-neutron transfer reaction. A ^{155}Gd target (92 % enrichment in ^{155}Gd) with a thickness of 0.9 mg/cm^2 and a diameter of 10 mm deposited on 1.1 μm aluminum foil was bombarded by a 153 MeV ^{18}O beam. Here, θ_{gr} is about 32^o with respect to the beam axis in laboratory system. Outgoing particles were detected by the Si Δ*E*-*E* detector. The Si Δ*E*-*E* detector consists of four surface-barrier type Si Δ*E* detectors with a thickness of 65 μm and a diameter of 20 mm, and an annular Si *E* detector with an inside diameter of 48 mm, an outside diameter of 96 mm, and a thickness of 300 μm. The Si *E* detector has sixteen annular active-areas covering angle ranges between 21.2^o and 37.8^o with respect to the incident beam axis. Hence we can obtain not only the energy distributions of the outgoing ^{16}O particles, but also the angular distributions of ^{16}O particles.

[1] Japan Atomic Energy Agency (JAEA)
[2] Tokyo Institute of Technology

Figure 1 shows E-ΔE plot for outgoing particles measured by the Si ΔE-E detector at θ (outgoing angle of ^{16}O) = 23.0^{o} (a), 27.6^{o} (b), 31.8^{o} (c), and 35.7^{o} (d) with respect to the beam axis, respectively. By assuming that the outgoing particle is not excited, excitation energy of compound nucleus can be deduced from the kinetic energy (E) of outgoing particle. The enclosed areas in Fig. 1 with dashed lines contains ^{157}Gd with excitation energy between 6.4 and 26.4 MeV. Since the neutron separation energy of ^{157}Gd is 6.4 MeV, these enclosed areas correspond to neutron energy up to 20 MeV in ^{157}Gd(n,γ) reaction. Figure 2 shows the energy and angular distributions of outgoing ^{16}O particles contained in the enclosed areas in Fig. 1. As shown in Fig. 2 the peak is located at $E \approx 134$ MeV and $\theta \approx 24^{o}$. The peak of the angular distribution is smaller than $\theta_{gr} \approx 32^{o}$. This suggests that slightly lower bombarding energy (~ 135 MeV) is more suitable for measurement of ^{155}Gd(^{18}O, ^{16}O) two-neutron transfer reaction.

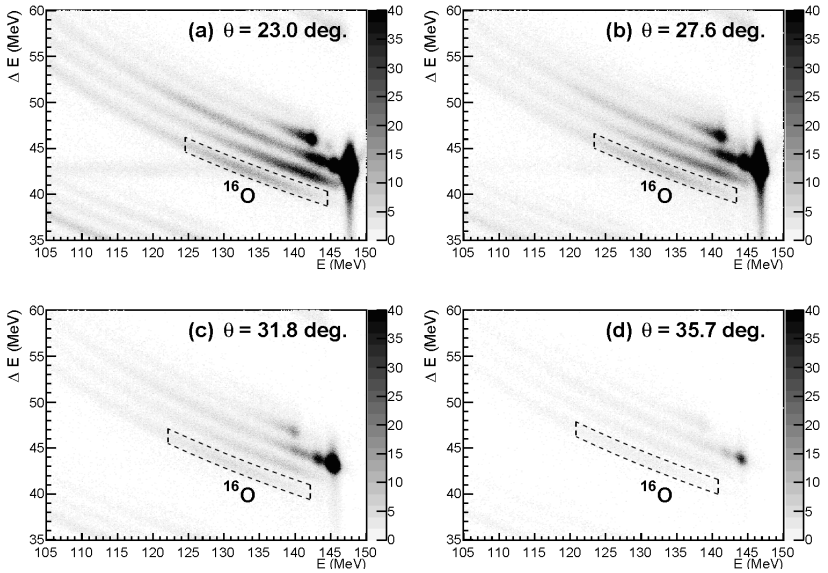

Fig.1 E-ΔE plot for outgoing particles measured by the Si ΔE-E detector at outgoing angles of θ = 23.0 ^{o} (a), 27.6 ^{o} (b), 31.8 ^{o} (c), and 35.7 ^{o} (d) with respect to the beam direction, respectively.

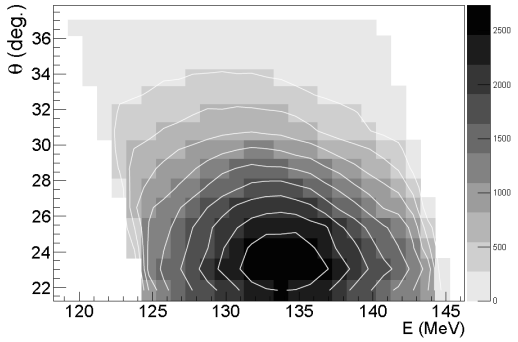

Fig. 2 Energy and angular distributions of outgoing ^{16}O particles from ^{155}Gd(^{18}O, ^{16}O) reaction.

References

[1] F. Käppeler and A. Mengoni, Nucl. Phys., A777 (2006) pp.291-310.

[2] J.E. Escher et al., Rev. Mod. Phys. 84 (2012) pp.353-397.

[3] H. Makii et al., JAEA-Tokai Tandem Annu. Rep. 2011, JAEA-Review 2013-002 (2013) pp.19-20.

[4] K. Ogata, S. Hashimoto and S. Chiba, J. Nucl. Sci. Technol. 48 (2011) pp.1337-1342.

3.3 Fission of iridium isotopes

K. Nishio[1], A. Andreyev[2], H. Kentaro[1], J. Cubiss[2], E. Maeda[1],
H. Makii[1], T. Nagayama[1,3], I. Nishinaka[1], S. Ohta[1] and T. Ohtsuki[4]

Finding of an asymmetric mass distribution in the low-energy fission of proton-rich nucleus ^{180}Hg [1] initiated several theoretical calculations on the fragment mass distributions for nuclei in wide area of chart of nuclei. It was demonstrated by P. Möller and J. Randrup that there was an island of mass-asymmetric fission in the proton-rich lead nuclei [2]. Also in the light nuclei between Z = 74 – 78 (tungsten to platinum), a fission mode with very large mass asymmetry was predicted, suggesting the possible formation of cluster structure at the last stage of the fission process due to the shells in the vicinity of doubly-magic nucleus ^{132}Sn. Motivated by the theoretical predictions, we started a campaign to measure the fission fragment mass distributions for nuclei in wide area on the chart of nuclei. First attempt was focused on the fission of compound nuclei ^{189}Ir and ^{193}Ir formed in the reactions of ^{7}Li + ^{182,186}W. The ^{189}Ir is the nucleus also studied in the reactions of p + ^{188}Os and α + ^{185}Re [3].

Exeriment was carried out using the ^{7}Li beams suppled by the tandem accelerator. Thin targets of about 100 μg/cm^2 were made by sputtering the enriched tungstem materials (isotopic abundance : 99.4 % for ^{182}W and 99.8% for ^{186}W) on a carbon foil of 50μg/cm^2. Both fission fragments were detected by two position-sensitive multi-wire proportional counters (MWPCs) with active area of 200mm × 200 mm. The MWPCs were mounted at ± 90^o relative to the beam direction at a distance 249 mm from the target. Incident beam energies were E_{beam} = 68.0, 41.1, and 31.5 MeV.

Figure 1 shows the mass distribution of the compound nucleus ^{189}Ir* at the ^{7}Li incident beam energy of 41.1 MeV (excitation energy E^* = 50.8 MeV). The distribution shows a symmetric shape with the standard deviation σ_m = 13.1 u. This value is about 18 % larger than σ_m = 10.7 u obtained in the reaction α + ^{185}Re leading to the same compound nucleus at the slightly lower excitation energy of E^* = 47.5 MeV studied in the α + ^{185}Re reaction [3]. In this spectrum, we did not observe clear signature of the fission mode with large mass asymmetry. The analysis for the other incident energies and the other compound nucleus ^{193}Ir is in progress.

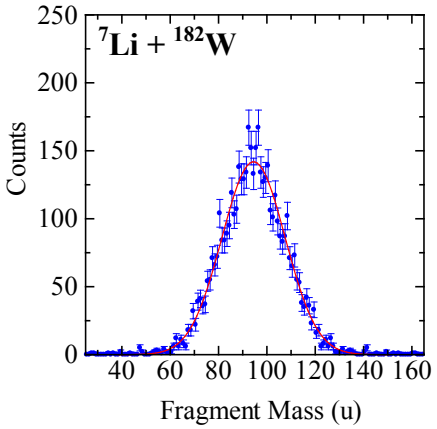

Fig. 1 Fragment mass distributions of the fission of ^{198}Ir*.

References

[1] A. Andreyev et al., Phys. Rev. Lett., 105 (2010) 252102.
[2] J. Randrup and P. Möller, private communication.
[3] M.G. Itkis et al., Sov. J. Nucl. Phys. 53 (1991) 757.

[1] Japan Atomic Energy Agency
[2] University of York
[3] Ibaraki University
[4] Tohoku University

3.4 Fission fragment anisotropy in heavy-ion-induced fission of actinide nuclei

I. Nishinaka[1], M. Tanikawa[2], K. Nishio[1], H. Makii[1], S. Mitsuoka[1], Y. Wakabayashi[1] and A. Yokoyama[3]

In general fission fragment angular distributions in light-ion-induced fission are successfully explained by the standard saddle point model [1]. However, in heavy-ion-induced fission of actinides at near-barrier energies, it has been found that fission fragment anisotropy becomes anomalously larger than that expected from the standard saddle point model [2, 3]. This anomaly of fission fragment anisotropy was thought to originate from non-equilibrium fission. The pre-equilibrium *K*-states model suggests that fission fragment anisotropy in heavy-ion-induced fission of actinides is governed by the entrance channel mass asymmetry $\alpha=(A_t-A_p)/(A_t+A_p)$ [4, 5], where A_t and A_p refer to mass numbers of target and projectile nuclei, respectively. A limited number of experiments have been carried out to study the effect of different entrance channels leading to the same compound nucleus, ^{248}Cf (^{16}O+^{232}Th and ^{12}C+^{236}U) [6] and ^{246}Bk (^{14}N+^{232}Th and ^{11}B+^{235}U) [7]. In order to study the effect of fission fragment anisotropy on entrance channels we measured fission fragment angular distributions in the reactions of ^{22}Ne+^{232}Th (α =0.827), ^{16}O+^{238}U (α =0.874) and ^{12}C+^{242}Pu (α =0.906)[8], leading to the same compound nucleus ^{254}Fm. As shown in Fig.1, the anisotropy for ^{22}Ne+^{232}Th with the smallest entrance channel mass asymmetry α=0.827 is larger than those for ^{16}O+^{238}U and ^{12}C+^{242}Pu. This results are hardly explained by the Businaro-Gallone critical point of mass asymmetry for ^{254}Fm (α_{BG} =0.903) [9]. The uncertainty of the anisotropy is rather large especially for ^{22}Ne+^{232}Th because of the low statistics. In order to make quantitative understanding, it is important to obtain data with small uncertainty. Therefore, we have carried out the measurement for the ^{22}Ne+^{232}Th reaction to obtain more statistics. Analysis of data is still in progress.

References

[1] R. Vandenbosch and J. R. Huizenga, Nuclear Fission (Academic, New York, 1973).

[2] S. Kailas, J. Phys., G 23 (1997) pp.1227-1233.

[3] J. P. Lestone et al., J. Phys., G 23 (1997) pp.1349-1357.

[4] V. S. Ramamurthy et al., Phys. Rev. Lett., 65 (1990) pp.25-28.

[5] Z. Liu et al., Phys. Lett., B 353 (1995) pp.173-178.

[6] R. Vandenbosh et al., Phys. Rev., C 54 (1996) pp.R977-R980.

[7] B. R. Behera et al., Phys. Rev., C 69 (2004) 064603.

[8] I. Nishinaka et al., JAEA-Review 2010-056 (2010) pp.46-47; I. Nishinaka et al., JAEA-Review 2011-040 (2011) pp.31-32.

[9] U. L. Businaro and S. Gallone, Nuovo Cimento 5(1957) p.315; K. T. R. Davies and A. J. Sierk, Phys. Rev. C31(1985) p.915; M. Abe, KEK preprint 86-26, KEK-TH-128 (1986).

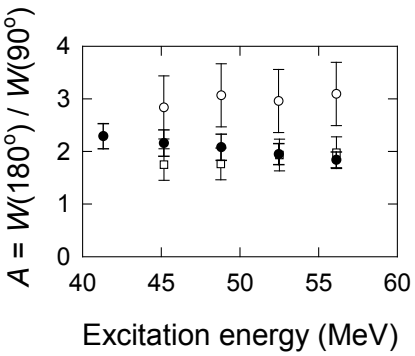

Fig. 1 Results of the fission fragment anisotropy for ^{16}O+^{238}U (solid circles), ^{12}C+^{242}Pu (open squares) and ^{22}Ne+^{232}Th (open circles) as a function of the excitation energy of the compound nucleus ^{254}Fm.

[1] Japan Atomic Energy Agency (JAEA)
[2] The University of Tokyo
[3] Kanazawa University

3.5 Measurement of branching ratio of ^{22}Ne (α, γ) ^{26}Mg / ^{22}Ne (α, n) ^{25}Mg reactions (2)

S. Ota[1], H. Makii[1], T. Ishii[1], I. Nishinaka[1], K. Nishio[1], S. Mitsuoka[1] and S. Chiba[2]

In He-burning phase of massive stars, the ^{22}Ne(α, n)^{25}Mg reaction is considered to be the main neutron source driving the synthesis of nuclides in the A = 60-90 mass range during the *s* process [1]. The reaction also acts as a secondary neutron source during the *s* process in low-mass asymptotic giant branch (AGB) stars during which roughly half the abundances of nuclides in the A = 90-209 range are thought to be synthesized [2]. A variety of attempts to experimentally determine the rate for this reaction at the Gamow window (E_α = 400-1000 keV) corresponding to *s* process temperatures (T_9 = 0.2-0.3 GK) has been made by such as direct ^{22}Ne(α, n)^{25}Mg measurements [e.g., 3], ^{26}Mg(γ, n)^{25}Mg [4], ^{25}Mg(n, γ)^{26}Mg [e.g., 5], ^{26}Mg(γ, γ')^{26}Mg [e.g., 6], ^{26}Mg(p, p'γ)^{26}Mg [7], and ^{22}Ne(^{6}Li, d)^{26}Mg α-transfer reactions [8, 9]. However, unambiguous determination of the resonance parameters such as E_r, J^π, Γ, Γ_γ, Γ_n and Γ_α in ^{26}Mg produced by α + ^{22}Ne has remained the longstanding problem. Of these ambiguous parameters, the ratio of Γ_n and Γ_γ to determine the branching ratio of γ and n emission channels play an important role to obtain the neutron yield for *s* process. The competing ^{22}Ne(α, γ)^{26}Mg reaction (Q = 10.615 MeV) with the ^{22}Ne(α, n)^{25}Mg reaction (open above excitation energy of ^{26}Mg, E_x = 11.093 MeV) may be of considerable strength and significantly suppress the neutron production during the He burning (E_x = 10.9-11.5 MeV). To solve this problem, we propose a ^{6}Li(^{22}Ne, ^{26}Mg)d α-transfer experiment. Because the ground states of α and ^{22}Ne are $J^\pi = 0^+$, the α-transfer reaction preferentially populates the natural parity states in ^{26}Mg. This makes possible to study astrophysically relevant natural parity states in ^{26}Mg. Different from the kinematics used in the ^{22}Ne(^{6}Li, d)^{26}Mg reaction, its inverse kinematics enables us to determine the Γ_n / Γ_γ from measurements of the ratio of ^{26}Mg and ^{25}Mg produced in the reaction.

We performed the ^{6}Li(^{22}Ne, ^{26}Mg)d experiment using a 110 MeV ^{22}Ne beam from JAEA -Tokai Tandem accelerator. ^{6}Li-enriched (95%) lithium carbonate (Li_2CO_3) target with the thickness of 20 μg/cm^2 was prepared on a graphite backing foil (20 μg/cm^2) so that the energy loss of the ^{22}Ne beam and deuterons in those materials will be negligibly small. The beam intensity was 10 pnA, and the experiment continued for 12 hours. Si ΔE-E detectors are used for particle identification in both of Mg and deuterons. For the detection of Mg, we used 20 μm thickness surface-barrier type detectors and 300 μm thickness PIN diode detectors. For the detection of deuterons, we used 75 μm thickness ion-implanted type detector and 300 μm thickness PIN diode detectors. Energy resolutions of ΔE and E detectors for the upstream detectors are 40 keV and 25 keV using ^{241}Am source, respectively. Thus totally < 50 keV is achieved, which is a better resolution than the former experiment with a ^{6}Li beam [9]. For each of the upstream (deuteron) and the downstream (Mg) detectors, 4 sets of Si ΔE-E detectors were used and placed at θ = 25° in Center-of-Mass (CM) system (θ_{CM}). The angle was chosen because the large cross section (about 10 μb/sr) was observed at the experiment by the normal kinematics [8]. To limit the scattered angle of deuterons, we have placed ϕ =

[1] Japan Atomic Energy Agency
[2] Tokyo Institute of Technology

1.0 mm collimators in the front of the downstream detectors. The energies of deuterons were measured to determine the excitation energy of ^{26}Mg. The background events are reduced by taking coincidence of Mg and deuteron. Details of the coincidence detection techniques are given in [10].

Figure 1 shows the deuteron spectrum obtained by the experiment. Those deuterons were all measured by the coincidence detection with the Mg. Unfortunately, no clear resonance structure could be identified from the figure, that is different from the spectrum obtained in [8] which was measured at almost the same CM angle. This is mainly due to the insufficient collimation of the particle detectors. In the present test, the size of slits were too large, the angular resolution of the deuterons were $\delta\theta_{LAB} < 2.5°$, i.e., the energy width of each resonance was about 250 keV.

In the next experiment, we will apply an improved detection system. Slits for both sides of upstream and downstream detectors will be introduced. This allows us to limit the $\delta\theta_{LAB}$ of deuteron small enough (< 0.2°). The construction of a new chamber for this geometry has been completed. Figure 2 shows the simulated spectrum of some known resonance states at 40° in CM for 3 days beam time by using the known cross section [8]. A clear resonance spectrum is expected in the next experiment and we will deduce the Γ_n / Γ_γ by the measurements of the yield ratio of ^{26}Mg and ^{25}Mg.

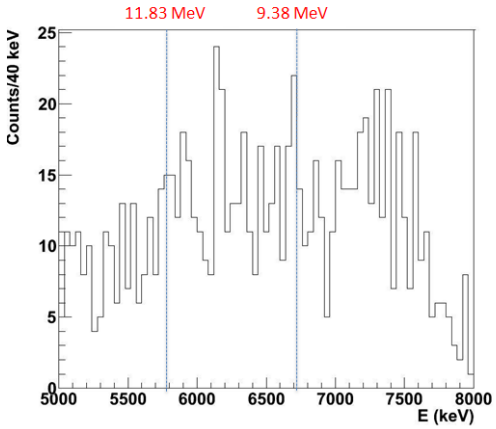

Fig. 1 Deuteron spectrum obtained by coincidence detection with Mg in the preliminary test ($\theta_{CM} = 25°$).

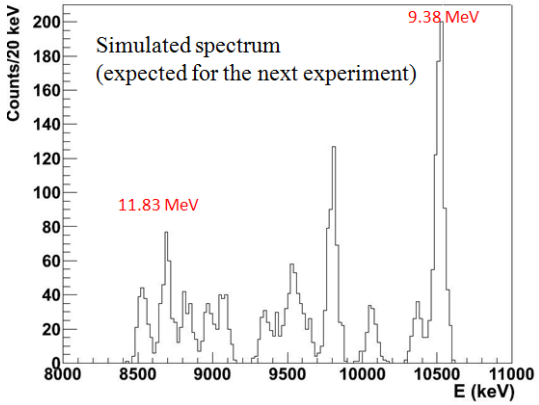

Fig. 2 An expected deuteron spectrum in the next experiment ($\theta_{CM} = 40°$).

References

[1] F. Kappeler, Prog. Part. Nucl. Phys., 43 (1999) p.419.

[2] O. Straniero et al., Astrophys. J. Lett., 440 (1995) p.L85.

[3] M. Jaeger et al., Phys. Rev. Lett., 87 (2001) 202501.

[4] B. L. Berman, R. J. Baglan, and C. D. Bowman, Phys. Rev. Lett., 24 (1970) p.319.

[5] C. Massimi et al., Phys. Rev., C 85 (2012) 044615.

[6] R. Longland et al., Phys. Rev., C 80 (2009) 055803.

[7] C. E. Moss, Nucl. Phys., A 269 (1976) p.429.

[8] U. Giesen et al., Nucl. Phys., A 561 (1993) p.95.

[9] C. Ugalde et al., Phys. Rev., C 76 (2007) 025802.

[10] S. Ota et al., 12th NIC Proceedings (2012) p.221.

This is a blank page.

CHAPTER 4

Nuclear Chemistry

This is a blank page.

4.1 Production of ^{95m}Tc for compton camera imaging

Y. Hatsukawa[1], K. Hashimoto[1], K. Tsukada[1], T. Sato[1], M. Asai[1], Y. Nagai[1],
A. Toyoshima[1], I. Tanimori[2], S. Sonoda[2], S. Kabuki[3], H. Saji[4] and Kimura[4]

Technetium-99m is the most common radioisotope used in medical diagnostic imaging. It is well suited to the role because it emits readily detectable 141 keV gamma rays, and its half-life is 6.01 hours. There are at least 31 commonly used radiopharmaceuticals based on technetium-99m for imaging and functional studies of the brain, myocardium, thyroid, lungs, liver, gallbladder, kidneys, skeleton, blood, and tumors. Recent years, with the development of the Compton camera which can realize high position resolution, technetium isotopes emitting high energy gamma-rays are required. In this study, technetium-95m which emits some gamma rays around 800 keV was produced in the ^{95}Mo(p,n)^{95m}Tc reaction.

$^{nat}MoO_3$ targets with 300-700 mg were irradiated with the 15 MeV proton beam for 7 hours at the JAEA Tandem accelerator. Averaged beam currents were 1.2 μA. After a few weeks cooling time, about 300-500 kBq of ^{95m}Tc were extracted from the irradiated MoO_3 target by a chemical separation described in [1].

Using purified ^{95m}Tc, a labeled compound, ^{95m}Tc-MDP (methylene diphosphate), was synthesized. In order to examine quality of the labeled compounds obtained in this study, a thin-layer chromatography (TLC) method was applied. A spot of solution of the labeled compound was placed at the edge of the TLC plate, and the plate stood up-right in a solvent. Two kind of solvents, Methyl ethyl ketone (MEK) and physiological saline were used. After about 10 -30 min dipping time, the TLC plates were dried and taken autoradiography images using imaging plates for 12 hours. Based on this result, it was found that the labeled compound, ^{95m}Tc-MDP was synthesized well.

Then, Compton camera imaging was taken by the Electron-tracking Compton gamma-ray camera (ETCC) which was developed by the Tanimori's group of Kyoto University for medical usage [2-4]. 170 kBq technetium-95m solution contained in ϕ10 mm plastic vial was used as a radiation source. The tentative result obtained from the experiment is shown in Fig.1. The white circle shows the size of ϕ10 mm plastic vial source. The obtained image taken by ETCC is distributed about ϕ30 mm. A higher position sensitivity image can be reconstructed by more careful data analysis.

[1] Japan Atomic Energy Agency
[2] Department of Physics, Kyoto University
[3] School of Medicine, Tokai University
[4] Faculty of Pharmaceutical Sciences, Kyoto University

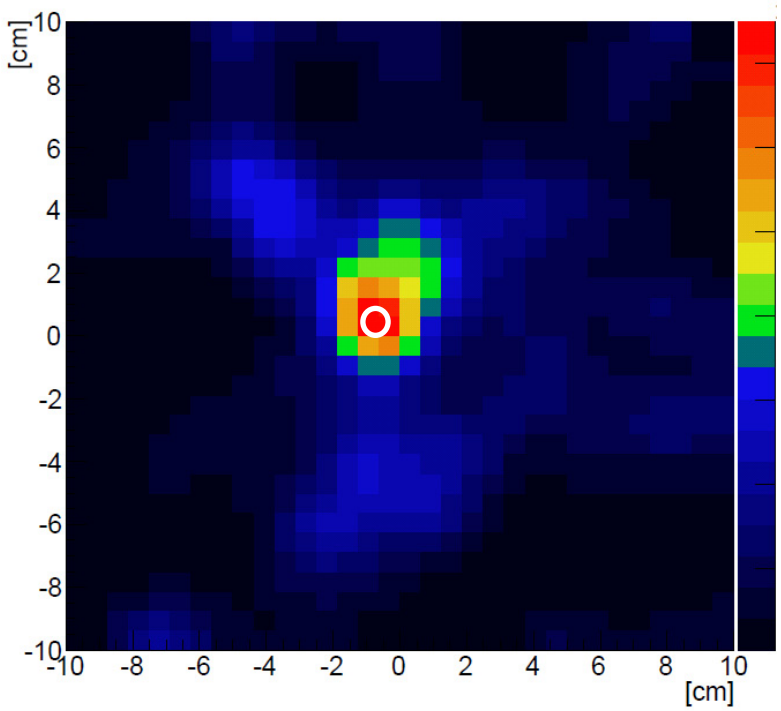

Fig.1 A preliminary result of imaging obtained from the ETCC. The white circle shows the size of original Tc-95m source. Most of events are reconstructed within about ϕ30 mm.

References

[1] Y. Hatsukawa et al, JAEA-Review 2011-040, pp.52-53.

[2] S.Kabuki et al., Nucl. Instrum. Methods Phys. Res., A623 (2010) p.606.

[3] S.Kabuki et al., Nucl. Instrum. Methods Phys. Res., A 580 (2007) p.1031.

[4] T. Tanimori et al., New Astron. Rev. 48 (2004) p.236.

4.2 Synthesis of astatinated phenylalanine derivatives via electrophilic destannylation for the preparation of astatinated peptide

Sh. Watanabe[1], I. Nishinaka[1], K. Hashimoto[1], I. Sasaki[1], Sa. Watanabe[1], Y. Sugo[1], H. Makii[1] and N. S. Ishioka[1]

Alpha emitting radionuclides have been of interest for several decades as candidates for radiotherapy due to their high cytotoxicity against living cells. ^{211}At (half-life: 7.21 h) is one of the most promising radionuclides because its half-life is long enough to accumulate in target tissues and its α-particle energy (5870 keV and 7450 keV from ^{211}Po) is appropriate for therapy [1]. Biologically active peptides characteristically display high specificity to receptor proteins expressed in cancer cells and rapidly localize in those cells within several hours. These properties make peptides attractive as carrier molecules or targeting vectors of therapeutic radionuclides for cancer therapy. Peptide Receptor Radionuclide Therapy (PRRT), or radiotherapy using radiolabeled peptides, has been demonstrated in the treatment of neuroendcrine tumors [3,4]. ^{211}At labeled peptides are also promising radiopharmaceuticals for the PRRT. The goal of this study is to prepare an astatinated biologically active peptide for PRRT. Electrophilic destannylation has been shown to rapidly substitute astatine for a stannyl group with high yield and under mild conditions [5]. Therefore, astatine labeled peptides will be easily prepared in the presence of peptides containing a stannylated amino acid residue. In this study, we demonstrated synthesis of an astatinated phenylalanine from the stannylated precursor via electrophilic destannylation as a feasible technique.

$^{208\text{-}211}$At were produced by irradiating a ^{nat}Pb target (1.2 mg/cm^2 thickness) with ^{7}Li beam (45 MeV, 138 nA current) via the ^{nat}Pb(^{7}Li,xn)$^{208\text{-}211}$At reaction. $^{208\text{-}211}$At isotopes were isolated from the irradiated target by dry distillation as previously described [6]. The synthetic route of derivatization of phenylalanine is outlined in Scheme 1. *N*-Boc-*p*-tributylstannylphenylalanine methyl ester **3** was then synthesized by procedures reported previously [7]. *N*-Boc-*p*-radiohalogenatedphenylalanine methyl esters **4, 5, 6** were obtained by procedures as follows; to a solution containing 10 μL of 10 mg/mL of the stannylated phenylalanine in ethanol was added 200 μL of ethanol containing $^{208\text{-}211}$At, ^{77}Br, or ^{131}I. Then, 20 μL of 10 mg/mL of *N*-chlorosuccinimide in ethanol was added. The mixture was stirred at room temperature for 15 min. The reaction was stopped by adding 10 μL of 10 mg/mL of sodium metabisulfite in H_2O. The desired compound was confirmed by thin layer chromatography (TLC). A 10 μL of a portion of the reactant was spotted 2 cm from the bottom of a silica gel thin layer chromatography (TLC) plate. The plates were developed by dichloromethane/methanol solution (20/1, v/v). After drying, the plates were exposed to the imaging plate for 24 hours, and whereby the distribution of radioactivity on the plates was visualized by the Bioimaging Analyzer System (BAS). The labeling yield was calculated from the measured radioactivity of each spot obtained by the BAS.

TLC images of the astatinated compound showed that a strong radioactive spot was observed at R_f = 0.8 (Fig. 1a) while free astatine at R_f = 0.0 (Fig. 1b). Astatine has no stable isotopes, which makes it quite difficult to characterize astatinated compounds by conventional devices such as NMR and mass spectroscopy. Phenylalanine derivatives labeled with ^{131}I, **5,** or ^{77}Br, **6**, were then prepared in order to characterize the astatinated product. A single radioactive spot was observed at R_f = 0.75 for **5** (Fig. 1c), and R_f = 0.73 for **6** (Fig. 1f), respectively, which were identical to those of

[1] Japan Atmic Energy Agency (JAEA)

non-radioactive compounds **1** (Fig. 1e) and **7** (Fig. 1h). These results clearly indicated that the astatinated phenylalanine derivative was successfully produced by electrophilic destannylation. The labeling yield of the astatination was estimated to be over 95%.

Future work will focus on the synthesis of an astatinated peptide which binds to the Her2/neu receptor protein. The protein has been shown to be overexpressed on the cell surface of both breast cancer and lung cancer [7]. Interest in this receptor is generated from literature which suggests that a peptide consisting of six amino acids (Met-Ala-Arg-Ser-Gly-Leu) strongly binds to the Her2/neu receptor[8]. Synthesis of the peptide containing astatinated phenylalanine (Phe(*p*-At)-Met-Ala-Arg-Ser-Gly-Leu is now being undertaken.

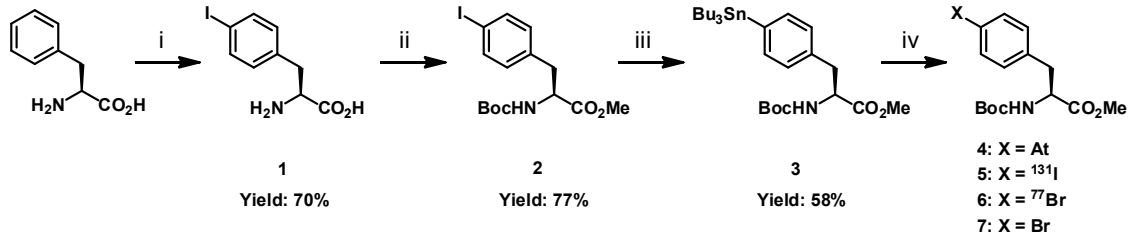

Scheme 1. Synthetic route of phenylalanine derivatives; i) I_2, $NaIO_3$, conc.H_2SO_4, AcOH, 70 ^oC; ii) Boc_2O, 1M NaOHaq., r.t.; iii) MeOH, EDC-HCl, DMAP, CH_2Cl_2, r.t.; iv) $(SnBu_3)_2$, $Pd(PPh_3)_4$, dioxane, N_2, reflux; v) At/$Na^{131}I$ /$Na^{77}Br$, *N*-chlorosuccinimide, 1%AcOH-EtOH, r.t.

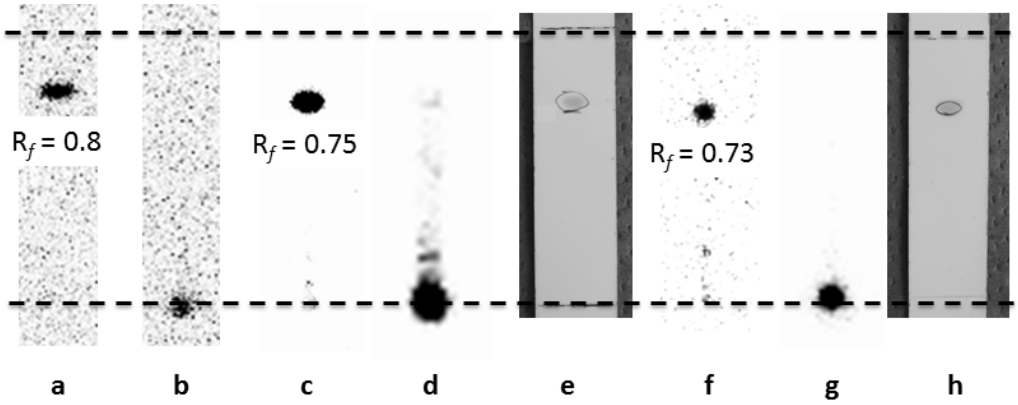

Fig. 1 Results of TLC experiments; a) **4**, b) free astatine, c) **5,** d) free iodine, e) **2**, f) **6**, g) free bromine, h) **7**. Images of a), b), c), d), f), and g) were visualized by BAS; e), and h) were visualized by UV.

References

[1] D. S. Wilbur, Curr. Radiopharm., 1, (2008) pp.144-176.

[2] V. Ambrosini et al., J. Nucl. Med., 52 (2011) pp.42S-55S.

[3] M. M. Graham and Y. Menda, J. Nucl. Med., 52, (2011) pp.56S-63S.

[4] M. J. Adam, and D. S. Wilbur, Chem. Soc. Rev. 34, (2005) pp.153-163.

[5] I. Nishinaka et al., JAEA-Review 2013-002 (2013) pp.33-34.

[6] I. Sasaki et al., Peptide Sci. 2012 (2013) pp.157-160.

[7] M. C. Hung, and Y. K. Lau., Semin Oncol. 26, (1999) pp.51-59.

[8] M. Houimei et al., Int. J. Cancer, 92 (2001) pp.748-755.

4.3 Extraction of astatine isotopes for development of radiopharmaceuticals

E. Maeda[1], A. Yokoyama[2], T. Taniguchi[1], K. Washiyama[3] and I. Nishinaka[4]

High energetic α-particles are expected to suppress tumor cell growth efficiently with a low level of damage to surrounding tissues because of their short path lengths in tissues (<100 μm) and high linear energies transferred (~100 keV/μm). Among a lot of α radionuclides, an ^{211}At isotope has gathered attention as a promising α-emitter for radionuclide therapy due to its proper half-life of 7.2 h. In order to obtain astatine isotopes, they are supposed to be produced via nuclear reactions, and separated from irradiated targets with high purity. But, the chemical properties of astatine are not well known for that purpose. In order to research on appropriate procedures in preparation of astatine for radiopharmaceuticals, we produced astatine isotopes by the reaction of ^{nat}Pb(^{7}Li, xn)$^{209\text{-}211}$At and performed a chemical separation of the isotopes from the target material. Solvent extraction has been considered one of the effective methods for that purpose [1]. We report dependence of the distribution ratio in solvent extraction of astatine on the concentration of HCl, and on the polarity of organic solvents to discuss the procedures.

A lead target (0.74 mg/cm^2) was irradiated with 50 MeV ^{7}Li beam with a current of 120-200 nA using the JAEA-Tokai tandem accelerator to produce astatine isotopes by the reaction of ^{nat}Pb(^{7}Li, xn)$^{209\text{-}211}$At. The irradiated target was put into a test tube and heated up to 650 ℃ and let stand for about 20 min in an electric furnace. Then carrier-free astatine was separated from the lead target by distillation. In the procedure, vaporized astatine isotopes were trapped in 4 M HCl solution which was then adjusted to several HCl concentrations between 1M and 8 M to be subjected to the extraction process of astatine isotopes with an equal volume of DIPE for 5 minutes. The γ-activity of each phase in extraction was measured with a HPGe detector to obtain the distribution ratio of astatine isotopes.
Subsequently, for the investigation on dependence of the distribution ratio of astatine on the polarity of the organic solvent, astatine isotopes were produced and distilled as in the experiment described above but trapped in 8 M HCl solution. Astatine was extracted from the 8 M HCl solution into equal volume of several different organic solvent in polarity by shaking for 5 min. The distribution rations were obtained in the same way as the experiment described above.

Dependence of the distribution ratio on the concentration of HCl was observed for DIPE as shown in Fig. 1. It demonstrates that the chemical species of astatine change depending on the HCl concentration. Astatine isotopes are extracted in the form of astatine chloride at higher concentration of HCl, but are extracted in the form of astatine hydroxide at lower concentration of HCl. On the other hand, the astatine isotopes were well extracted into DIPE and MIBK, but no significant extraction was observed in the other solvents as

[1] Grad. School Nat. Sci., Tech. Kanazawa Univ.
[2] Inst. Sci. Eng., Kanazawa Univ.
[3] Sch. of Health Sci., College of Med., Pharma. Health Sci., Kanazawa Univ.
[4] ASRC, Japan Atomic Energy Agency

shown in Fig. 2. It demonstrates that the affinity of astatine is related to polarity of the organic solvent for the 8M HCl solution. Our result is generally consistent with that of Ref. [2]. These results are still a part of chemical properties of the element in investigation but are useful for design of the chemical procedures in basic handling of astatine as well as development of the ^{211}Rn-^{211}At generator as the ultimate goal of the project.

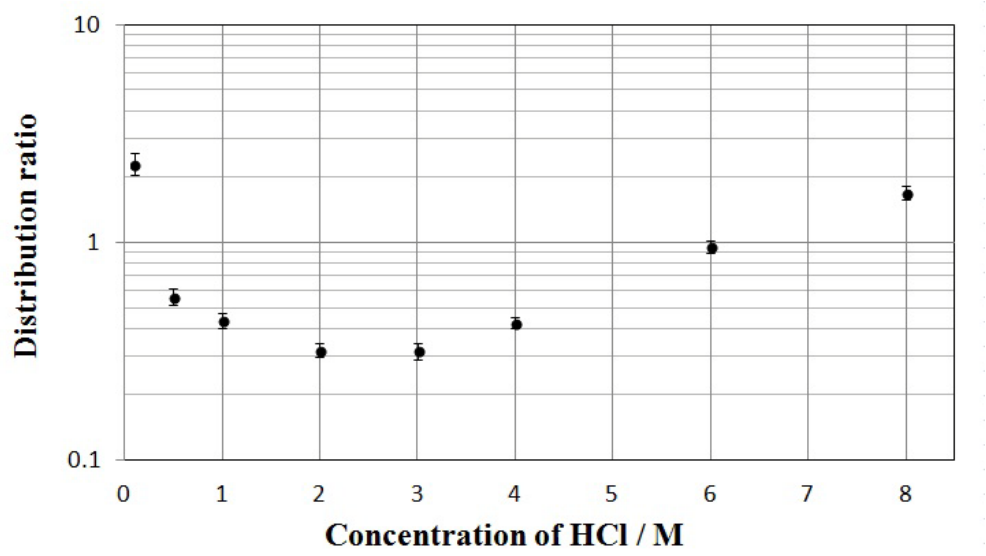

Fig. 1 Distribution ratios of astatine for several concentrations of HCl with DIPE.

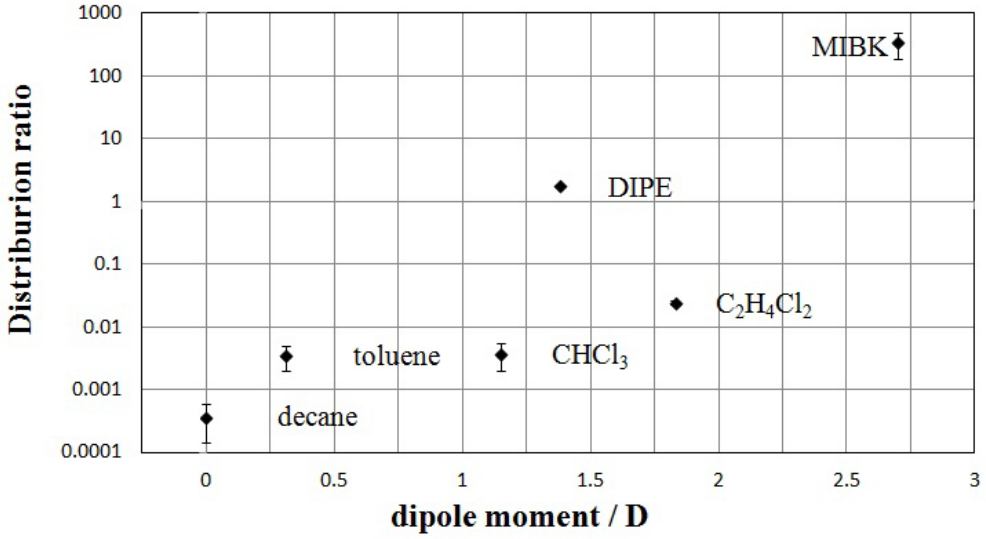

Fig. 2 Distribution ratios of astatine for different polarities of organic solvents with 8 M HCl.

References

[1] H. M. Neumann. Inorg. Nucl. Chem., 4 (1957) pp.349-353.

[2] C. Alliot et al., Radiochim. Acta., 97 (2009) pp.161-165.

4.4 Preparatory on-line extraction experiment of group-6 elements Mo and W for a reduction study of Sg

A. Toyoshima[1], S. Miyashita[1,2], K. Ooe[1,3], H. V. Lerum[4], Y. Kitayama[5], A. Wada[6], M. Asai[1], T.K. Sato[1], Y. Kaneya[1], Y. Komori[7], T. Yokokita[7], Y. Kasamatsu[7], K. Tsukada[1], Y. Kitatsuji[1], Y. Nagame[1], M. Schädel[1], J.P. Omtvedt[4], A. Yokoyama[5], H. Haba[8], A. Shinohara[7] and J.V. Kratz[9]

Seaborgium (Sg), placed on the group 6 of the Periodic Table, is expected to be redox-active similar to its lighter homologs, Mo and W. Theoretical calculation shows that Sg can be reduced from the most stable hexavalent state Sg(VI) to, e.g., the tetravalent one [1]. It also predict that the Sg(VI)/Sg(IV) couple will have a more negative redox potential than those of the corresponding W ions in acidic solution [1]. In such reduction reactions, electrons occupy the vacant valence 6d orbital of the Sg(VI) ion. The redox potential of the Sg(IV)/Sg(VI) couple, therefore, provides information on the stability of the 6d orbital which is influenced by increasingly strong relativistic effects.

Because of low production rates of ^{265a,b}Sg (a and b show two different states) in the ^{248}Cm(^{22}Ne, 5n) reaction and their short half-lives ($T_{1/2}$) of 8.5 s and 14.4 s [2], only single atoms of Sg are present. Thus, standard electrochemical techniques are not applicable to its reduction study. We are, therefore, developing a chemistry assembly available for the reduction of single Sg ions which will be coupled to a recoil separator like GARIS [2]. This assembly consists of a newly developed membrane degasser (MDG), a flow electrolytic column (FEC) and the continuous liquid-liquid extraction apparatus (SISAK) with a liquid scintillation counting system [3] to continuously perform dissolution, reduction, separation, and detection of Sg, respectively. In addition to that, we have found that Mo and W can be extracted from 0.1 M HCl/0.9 M LiCl to organic hinokitiol (HT) solution dissolved in toluene in separate batch experiments. In the present study, therefore, we carried out on-line extraction experiments of Mo and W isotopes using the MDG and SISAK at the JAEA tandem accelerator to test the extraction system of the assembly.

The radioisotopes ^{91m}Mo ($T_{1/2}$ = 65 s), ^{93m}Mo ($T_{1/2}$ = 6.9 h) and ^{176}W ($T_{1/2}$ = 2.5 h) were produced in the ^{89}Y(^{7}Li, 5n)^{91m}Mo, ^{89}Y(^{7}Li, 3n)^{93m}Mo, and ^{175}Lu(^{7}Li, 6n)^{176}W reactions, respectively. Nuclear reaction products were transported to the chemistry laboratory at a He gas flow rate of 1.5 L/min. The transported products were continuously introduced into a Y-shaped mixer of the MDG where the carrier gas containing the products was mixed with an aqueous solution of 0.1 M HCl/0.9 M LiCl. The flow rate of the aqueous

[1] Japan Atomic Energy Agency (JAEA)
[2] Hiroshima University
[3] Niigata University
[4] University of Oslo
[5] Kanazawa University
[6] Tokyo Metropolitan University
[7] Osaka University
[8] RIKEN
[9] University of Mainz

solution was 0.2 mL/s. The mixture passed through a shallow channel along a hydrophobic membrane filter (Fluoropore Membrane Filters, FGLP04700, Merck Millipore Ltd.) where only the carrier gas was sucked through the filter. The gas-free aqueous effluent from the MDG was then pumped through a thin Teflon tube into a Y-shaped mixer of SISAK. The aqueous solution was mixed with an organic solution of 10^{-5} - 10^{-2} M HT in toluene. The mixture was then separated in a centrifuging cell of SISAK. The separated effluent phases of aqueous and organic solution were collected in two plastic bottles. These samples were subjected to γ-ray measurement with Ge detectors. To quantify the separation, distribution ratio (D) was determined. D is defined by the equation $D = (A_{org} / V_{org}) / (A_{aq} / V_{aq})$, where A_{org} and A_{aq} are the amounts/activities of metal ions in organic and aqueous phases, respectively, and V_{org} and V_{aq} are the volumes of organic and aqueous phases, respectively.

The dissolved amounts of Mo and W were found to be as high as 70-90%, indicating successful dissolution with the newly developed MDG. In Fig. 1, variations of the D values of ^{91m}Mo, ^{93m}Mo, and ^{176}W are shown as a function of the concentration of HT ([HT]). The D values of Mo and W increase with increasing [HT]. This trend is consistent with that in the batch experiments, showing that SISAK is applicable to the extraction of Mo and W, although the D values obtained with this on-line experiment are smaller than those measured in the batch experiments. In the near future, after further optimization of the extraction system on-line reduction experiments of Mo and W will be carried out using MDG, FEC, and SISAK.

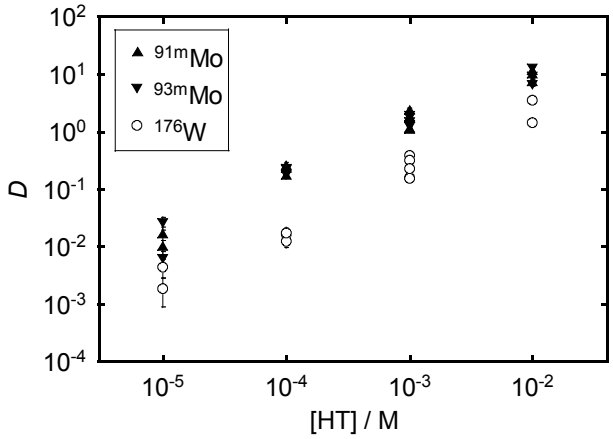

Fig. 1 Variations of distribution ratios (D) of ^{91m}Mo, ^{93m}Mo and ^{176}W as a function of the concentration of hinokitiol ([HT]).

References

[1] V. Pershina et al., J. Phys. Chem. A 103 (1999) pp.8463-8470.

[2] H. Haba et al., Phy. Rev., C 85 (2012) 024611.

[3] J. P. Omtvedt et al., Eur. Phys. J. D 45 (2007) pp.91-97.

4.5 Studies on transport mechanism of volatile Hf chloride compounds in quartz column with isothermal chromatography

S. Goto[1], Y. Oshimi[1], T. Tomitsuka[1], T. Asai[1], M. Murakami[1], K. Ooe[1], H. Kudo[1], K. Tsukada[2], M. Asai[2], T.K. Sato[2], A. Toyoshima[2], Y. Kanaya[2] and Y. Nagame[2]

A technique of a gas phase chemical separation has been applied to the chemistry experiments to clarify chemical properties of superheavy elements because it allows separating species of interest continuously and rapidly. In the gas-phase chemistry, sublimation enthalpies of volatile compounds can be deduced from their adsorption-desorption processes on a surface of gas chromatograph column. We have investigated gas chromatographic behavior of volatile chloride compounds of Hf isotopes with various half-lives for the study of Rf to confirm a model of an isothermal chromatography under our experimental condition. In the previous experiments[1], the temperature which the volatile compounds of Hf passed through the column was considerably higher rather than that of other reports[2, 3], and retention time was quite short. Since the oxychloride of Hf might be involving in these results, in order to obtain a pure chloride, the gases (He and HCl) to be used were refined further, and the experiments were performed again.

Hafnium isotopes, ^{165}Hf ($T_{1/2}$ = 76 s), ^{166}Hf ($T_{1/2}$ = 6.8 min), and ^{167}Hf ($T_{1/2}$ = 2.05 min), were produced in the ^{152}Gd(^{18}O, *x*n) reaction at the JAEA tandem accelerator facility. To compare with previous results, ^{85}Zr ($T_{1/2}$ = 7.9 min) were also produced in the ^{nat}Ge(^{18}O, *x*n) reaction. The Gd was electrodeposited with the thickness of 300 μg·cm^{-2} on 2.07 mg·cm^{-2} Be foil, and the Ge target was prepared with 212 μg·cm^{-2} using vapor deposition on the Gd target. The ^{18}O^{6+} beam energy was 108 MeV, and the intensity was about 1.3 μA. Nuclear reaction products were transported to the gas chromatographic apparatus with attaching on a carbon cluster in a He carrier gas flow. The schematic view of the apparatus is shown in Fig. 1. The carbon

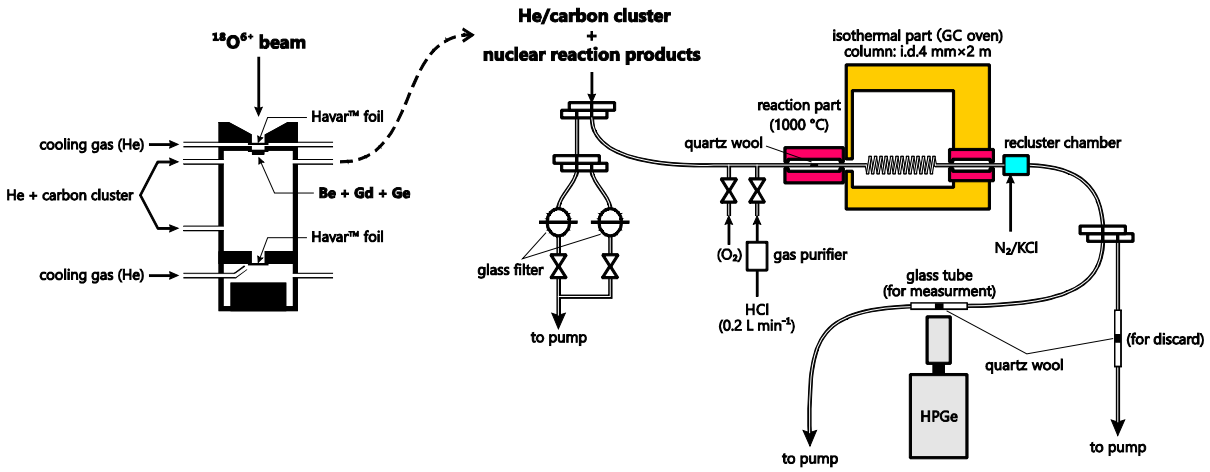

Fig. 1 Schematic view of the experimental setup.

[1] Niigata University
[2] Japan Atomic Energy Agency (JAEA)

cluster was produced by the DC pulse discharge between carbon electrodes. The carbon is expected to remove oxygen existing in the system which forms nonvolatile oxychlorides of Zr and Hf. The transported products were collected on quartz wool plugged in a quartz tube where a reactive HCl gas was added to form volatile chloride compounds. The formed volatile compounds were then fed into an isothermal chromatographic quartz column (i.d. 4 mm, 2 m length) directly connected to the tube. The flow rate of He carrier gas was 0.6 L min^{-1}, the reaction temperature was 1000 ºC, and the pressure at the reaction part was about 160 kPa. The compounds of Zr and Hf through the column were re-transported attaching on a KCl cluster in a N_2 carrier gas flow, and collected on glass wool plugged in a glass tube for γ-rays measurement to examine the yields of these elements which passed through the column. The passed-through yields for Zr and Hf were obtained as a function of the temperature of the isothermal column. As an additional treatment, the helium for carrier gas was refined with an oxygen and moisture trap and moisture was also removed from the chlorination reagent gas (HCl).

The chromatograms obtained in this study are shown in Fig. 2 together with the previous results. The temperature to which a volatile compound passes the column became low clearly. Since the condition changed experimentally was only having refined gas, oxygen or moisture had influenced the previous behavior of volatile compounds. However, the temperatures to pass through the column were still higher than estimation and other report [3] also at this result. Furthermore, the passage temperature hardly changed corresponding to the half-life of each isotope. Therefore, it seems that the influence of oxygen or moisture was not removed completely.

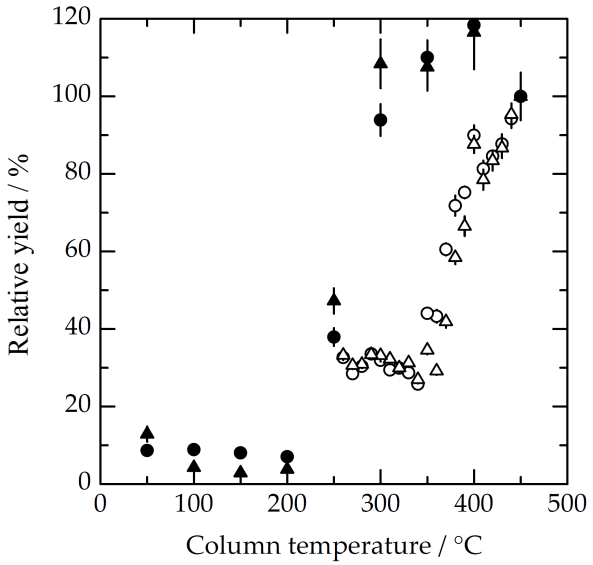

Fig. 2 Isothermal chromatograms of the compound of hafnium. Circle symbols are ^{165}Hf ($T_{1/2}$ = 76 s) and triangle symbols are ^{166}Hf ($T_{1/2}$ = 6.8 min). Closed symboles are the present results and open symbol are the previous results.

References

[1] S. Goto et al., JAEA-Review 2011-040 (2011) p.45.

[2] T.K. Sato et al., J. Nucl. and Radiochem. Sci., 6 (2005) pp.N1-N3.

[3] A. Türler et al., J. Alloys Compd., 271-273 (1998) pp.287-291.

CHAPTER 5

Nuclear Theory

This is a blank page.

5.1 Evolution of the energy levels and shell structure in antimony isotopes

Y. Utsuno[1], N. Shimizu[2], M. Honma[3], T. Mizusaki[4] and T. Otsuka[2]

Evolution of the shell structure (often called shell evolution) attracts much theoretical and experimental interest in the structure of unstable nuclei. In addition to well-known loosely bound effects, the nuclear force causes the shell evolution. For instance, the tensor force is demonstrated to give a considerable effect on the shell evolution [1]. Among various cases, it was considered that the evolution of low-lying levels in antimony isotopes (Z=51) offered an excellent example of the shell evolution due to the tensor force. This is because (i) the $7/2^+_1$ and $11/2^-_1$ states in odd-A antimony isotopes were regarded as rather good proton $g_{7/2}$ and $h_{11/2}$ single-particle states, respectively, according to the measurement of Schiffer et al. [2], and (ii) the evolution of the energy gap between those single-particle states extracted from experimental levels can be reproduced only with a mean-field calculation including the tensor force [3]. On the contrary, Sorlin and Porquet have recently pointed out that the $7/2^+_1$ and $11/2^-_1$ states in odd-A antimony isotopes are not good single-particle states based on (^{3}He, d) reaction data and that they are strongly affected by core-coupled states such as the $\pi(d_{5/2})\otimes 3^-_1$ state for the $11/2^-_1$ states [4]. Thus, it is desired to perform a large-scale nuclear-structure calculation which includes the core-coupled states within its model space to probe the shell evolution in this region.

In the present study, we have carried out shell-model calculations in the full $50\leq N\leq 82$ and $50\leq Z\leq 82$ valence space for the study of antimony isotopes. Namely, the $1d_{5/2}$, $0g_{7/2}$, $0h_{11/2}$, $1d_{3/2}$ and $2s_{1/2}$ orbits are adopted as the valence orbits. In this model space, collective states including the 3^-_1 states in tin isotopes are well described by using the semi-empirical neutron-neutron effective interaction named SNBG3 [5]. Hence, core-coupled states are treated appropriately. As for the proton-neutron interaction, which is the essential part in the proton shell evolution in an isotope chain, we take the same $V_{\rm MU}$ interaction as the one used for the study of neutron-rich silicon and sulfur isotopes [6]. The $V_{\rm MU}$ interaction [7] is aimed at universal description of the shell evolution, comprising the π+ρ meson exchange tensor force and a phenomenological Gaussian central force. Its monopole interaction, which characterizes the shell evolution, is close to that of realistic interactions for the *sd*- and *pf*-shell regions.

The $5/2^+_1$, $7/2^+_1$ and $11/2^-_1$ levels in antimony isotopes are compared between experiment and theory in Fig. 1. The present calculation successfully reproduces the experimental energy levels, and in particular the non-monotonic evolution of the $5/2^+_1$ and $11/2^-_1$ levels relative to the $7/2^+_1$ states. In order to clarify the relation between the energy levels and the shell structure, the energy levels are also estimated from the effective-single-particle energy (ESPE). The ESPE1 in Fig. 1 is defined most simply: the proton single-particle energies on top of ^{114}Sn (N=64) is obtained by assuming the neutron filling configuration in

[1] Japan Atomic Energy Agency (JAEA)
[2] University of Tokyo
[3] University of Aizu
[4] Senshu University

$1d_{5/2}$ and $0g_{7/2}$ based on the semi-magic number at N=64. For other neutron numbers, the energies are interpolated from those of N=50 or N=82. No correlation energy is taken into account for the ESPE1. On the other hand, the ESPE2 in Fig. 1 includes neutron-neutron correlation energy: the energies are calculated with the $\pi(j)\otimes 0^+_1$ states, where $\pi(j)$ and 0^+_1 are the proton single-particle state and the ground state of the tin isotopes of the same N. Proton-neutron correlation is not included in the ESPE2. It turned out that the trend of the evolution is rather close to the ESPE1 that is basically the same as the one in Ref. [1]. This indicates that cancellation between neutron-neutron correlation energy and proton-neutron correlation energy places the $11/2^-_1$ levels at correct positions. As a result, although the single-particle strengths in antimony isotopes are considerably reduced from unity due to the correlation energy as pointed out by Sorlin and Porquet [4], the evolution of the energy levels are still dominated by the evolution of the single-particle levels which is predominantly controlled by the tensor force.

References

[1] T. Otsuka et al., Phys. Rev. Lett., 95 (2005) 232502.

[2] J.P. Schiffer et al., Phys. Rev. Lett., 92 (2004) 162501.

[3] T. Otsuka et al., Phys. Rev. Lett., 97 (2006) 162501.

[4] O. Sorlin and M.-G. Porquet, Prog. Part. Nucl. Phys., 61 (2008) pp.602-673.

[5] M. Honma et al., RIKEN Accelerator Progress Report, 45 (2012) pp.35-35.

[6] Y. Utsuno et al., Phys. Rev. C, 86 (2012) 051301(R).

[7] T. Otsuka et al., Phys. Rev. Lett., 104 (2010) 012501.

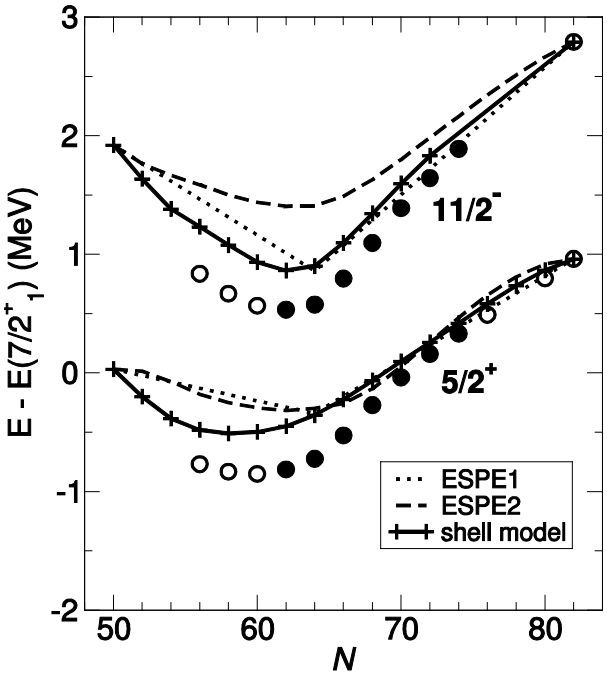

Fig. 1 Evolution of the $5/2^+_1$ and $11/2^-_1$ levels in antimony isotopes relative to $7/2^+_1$ compared between experiment (circles) and theory (lines). The filled circles denote the states whose single-particle strengths are measured to be large (≥0.5). The solid lines stand for the full shell-model calculation and the dotted and dashed lines correspond to the levels estimated from the effective single-particle energy. See the text for more details.

5.2 Single-particle levels of spherical nuclei in the superheavy and extremely superheavy mass region

H. Koura[1] and S. Chiba[2,1]

What are the nuclear structures far from the stability island of the superheavy mass region and is it possible to theoretically determine the limit of existence of the nuclear mass region? Doubly magic nuclei are mainly stabilized through neutron and proton shell closures, particularly spherical single-particle shell closure. By analyzing the single-particle levels of spherical nuclei, we expect to estimate the next island of stability in the extremely superheavy mass region. In this paper, we give a result of the extrapolation of single-particle levels to the extremely super heavy nuclear mass region obtained from a conventional phenomenological single-particle model constructed elaborately for spherical nuclei [1].

Figure 1 shows the whole nuclear chart, and the macroscopic proton and neutron drip lines and the fissility line, which roughly gives information on a region of possible existence of nuclei, are presented. Nuclei enclosed in boxes indicate predicted double magic nuclei (See also Figs. 2 and 3). Figures 2 and 3 show single-neutron and proton levels of unknown superheavy and extremely superheavy nuclei obtained from a modified Woods–Saxon potential, which are smooth functions of the number of nucleons [2]. This extrapolation gives that neutron shell closure remains for $N = 308$, and a proton shell has a gap at $Z = 164$, which is weaker than that of a neutron shell. Totally seven unknown doubly magic spherical nuclei beyond ^{208}Pb are found: $^{256}U_{164}$, $^{298}Fl_{184}$ (Z=114), $^{310}[126]_{184}$, $^{342}Fl_{228}$, $^{366}[138]_{228}$, $^{462}[154]_{308}$, and $^{472}[164]_{308}$. Of these, the $^{298}Fl_{184}$ and $^{472}[164]_{308}$ are beta-stable nuclei. The nucleus $^{472}[164]_{308}$ seems to be the heaviest nuclei in the possibly 'rather' long-lived nuclei obtained from the analysis of location of neutron and proton drip lines and the fissility line.

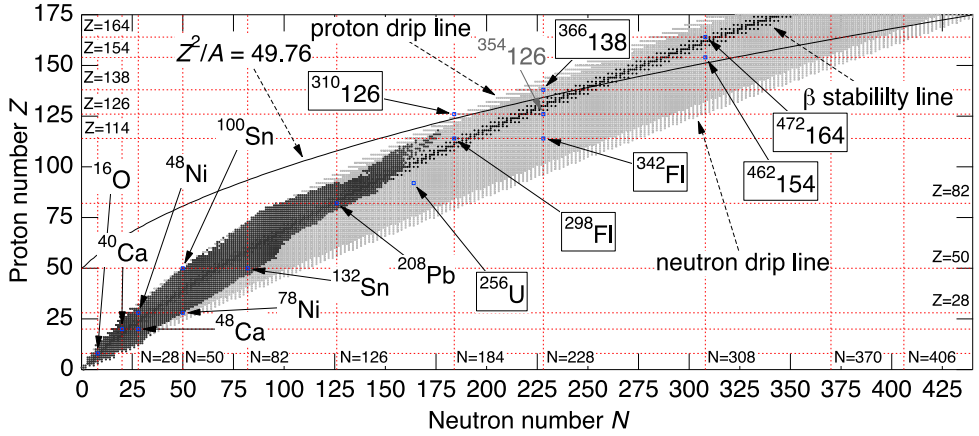

Fig. 1 Nuclear chart for calculated nuclei. Drip lines, the beta-stability line, and fissility line (Z^2/A=49.76) are obtained from the Weizsäcker–Bethe mass formula [1]. Identified nuclides are also plotted.

[1] Japan Atomic Energy Agency (JAEA)
[2] Tokyo Institute of Technology

References

[1] H. Koura and S. Chiba, J. Phys. Soc. Jpn. 82 (2013) 014201.

[2] H. Koura and M. Yamada, Nucl. Phys., A 671 (2000) pp.96-118.

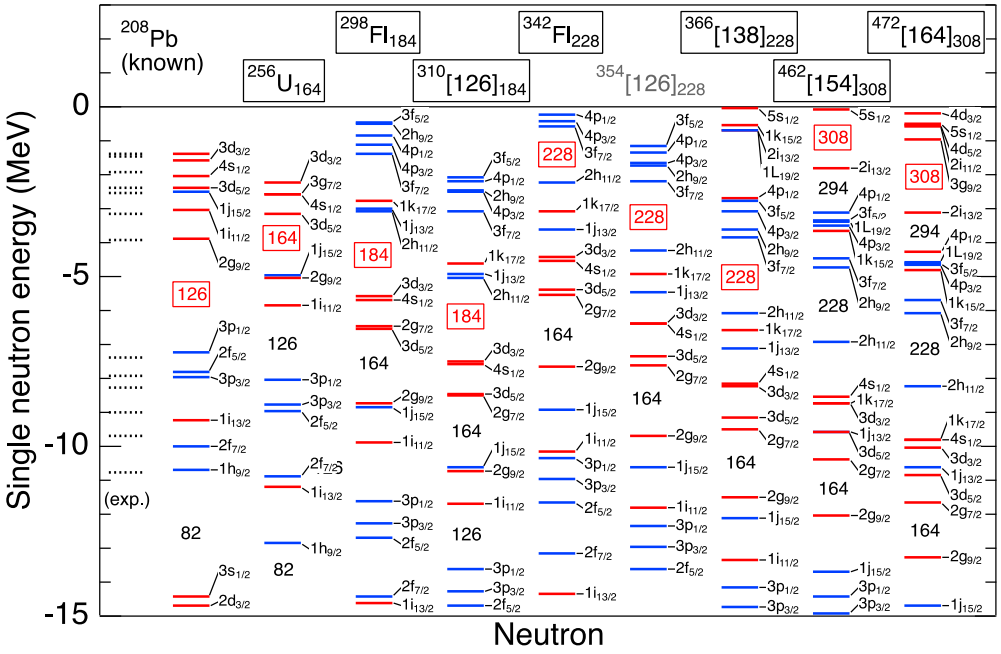

Fig. 2 Calculated neutron single-particle levels for doubly magic nuclei. Experimental levels for ^{208}Pb are also plotted. Numbers enclosed in boxes indicate closed shells at the Fermi surface. The nucleus $^{354}[126]_{228}$ is not a doubly magic nucleus but a single magic nucleus.

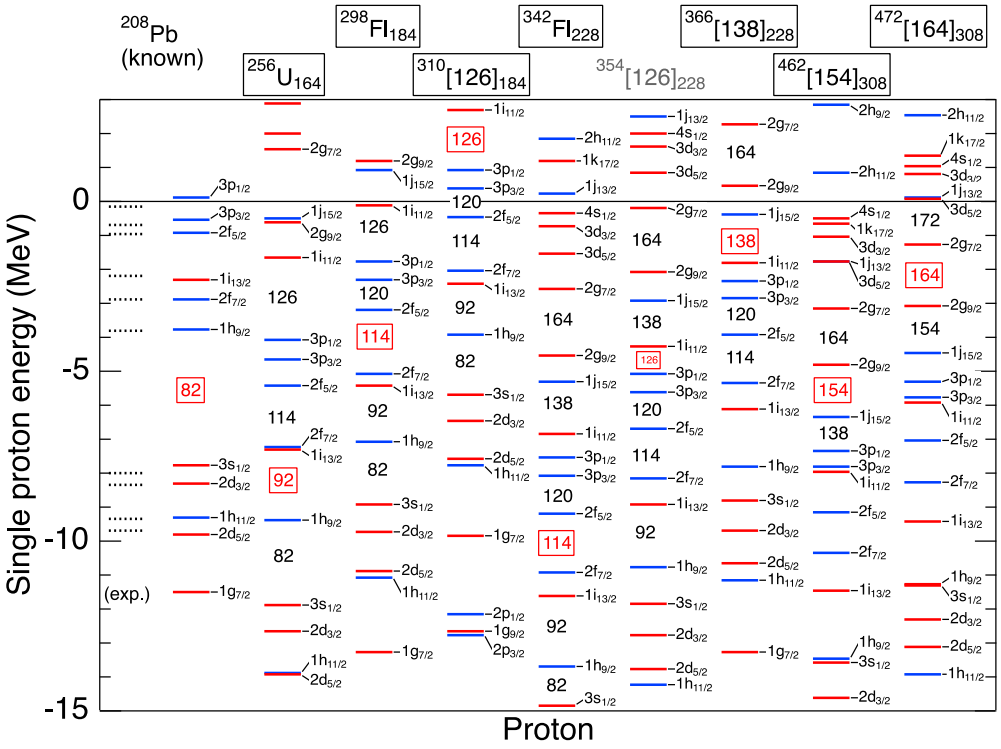

Fig. 3 Calculated proton single-particle levels for doubly magic nuclei.

CHAPTER 6

Atomic Physics and Solid State Physics

This is a blank page.

6.1 Charge state distribution of tungsten ions after penetration of C-foil targets

M. Imai[1], M. Sataka[2], K. Kawatsura[3], K. Takahiro[4],
K. Komaki[5], K. Nishio[2], H. Shibata[1] and S. Okayasu[2]

When (even single) fast heavy-ion in MeV/u energy range irradiates a solid target, a unique characteristic-effect, which cannot be brought about by any other means like photon or electron impacts, takes place by accumulation of several consecutive elastic and inelastic collision processes between projectile ion and target atoms. It is known for fast heavy-ion irradiation that the electronic stopping power, caused by the inelastic processes, is larger than the atomic (elastic) stopping power by more than three orders of magnitude. As a total range for fast heavy ions is longer than 10 μm, such electronic excitation effects span from the solid surface into inside the material and those features play effective roles in material modification. Furthermore, each inelastic collision process is strongly affected by energy, charge state, electronic state and so on of the projectile ions, and our previous measurements [1] using sulfur and carbon projectile ions have made it clear that collision frequency, *i.e.*, collision cross sections exert an effect on charge and electronic state evolution. Fast tungsten ions are often used for material modification. As they still wear quite number of electrons during solid penetration, charge and electronic state evolution of the projectile and secondary ion production and its transport are important aspects to understand the basics of the material modification. The present measurement is a part of our joint research project of "Basic processes of fast heavy-ion irradiation into solid and material property modification" and is devoted to the study of the equilibrium charge state distribution of 1.0 MeV W^{30+} projectile ions after C-foil penetration.

As has been presented in the previous annual reports [2, 3], we have measured the exit charge state distributions for penetrations of S^{6+} – S^{16+} ions through C-foil targets of 0.9 – 200 μg/cm^2 in thickness and performed calculations by an ETACHA code [4] to succeed in reproducing the experimental results, although ETACHA has been designed for higher energy region (>10 MeV/u) [1]. In this report, results of our brand new measurements for tungsten projectiles are presented.

The experiments were performed at the LIR1–3 beam line of the 20UR Tandem Accelerator Facility. A beam of 1.0 MeV/u (184 MeV) $^{184}W^{13+}$ ion was provided from the Tandem Accelerator within an energy accuracy of 0.1%, which was sufficient to separate the W isotopes, and post-stripper C-foil of ~20 μg/cm^2 was used to produce higher charge states of 30+. The W^{30+} ion beam was directed into a self-support carbon foil targets of 9.9 μg/cm^2 in thickness, which was sufficient for establishing charge state equilibrium. The charge states after foil penetration were measured using the heavy ion magnetic spectrometer ENMA and a position-sensitive gas chamber detector. The vacuum condition inside the collision chamber and the spectrometer were maintained below 10^{-4} and 10^{-6} Pa, respectively, to practically eliminate background

[1] Kyoto University
[2] Japan Atomic Energy Agency (JAEA)
[3] Kansai Gaidai University
[4] Kyoto Institute of Technology
[5] RIKEN

charge-exchange collisions with residual gas, which was confirmed by measurements with no foil targets. Measured equilibrium charge state distribution for 1.0 MeV/u W^{30+} ion incidence after penetration through C-foil target is plotted in Fig. 1. The measured most-probable charge state and the distribution center were 31+ and 31.3, respectively, whereas the only available data from literature [5] predict smaller values.

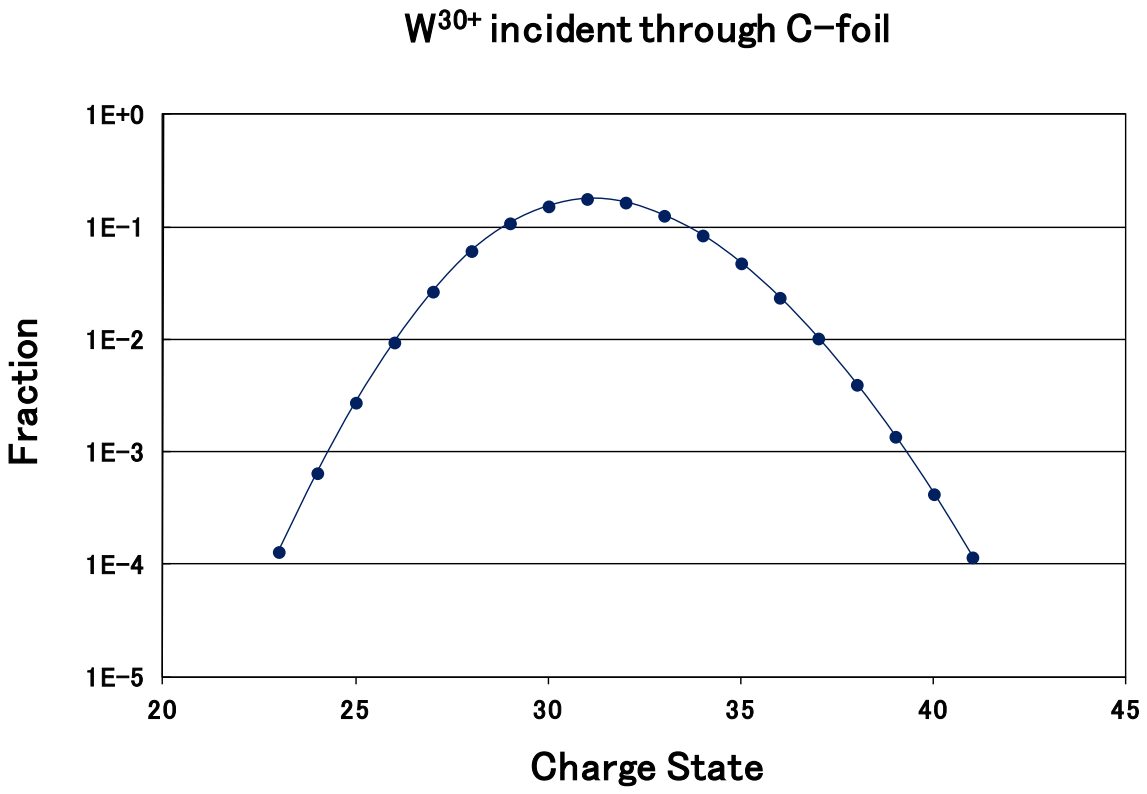

Fig. 1 Equilibrium charge state distribution for 1.0 MeV/u W^{30+} ion incidence after penetration through 9.9 μg/cm^2 C-foil targets.

References

[1] M. Imai et al., Nucl. Instrum. Methods Phys. Res., B230 (2005) pp.63-67; *ibid*. B256 (2007) pp.11-15; *ibid*. B267 (2009) pp.2675-2679.

[2] M. Imai et al., JAEA-Review 2007-046 (2008) pp.87-88; 2008-054 (2008) pp.89-90; 2009-036 (2009) pp.91-92; 2010-056 (2010) pp.89-90; 2011-040 (2011) pp.67-68; 2013-002 (2013) pp.49-50.

[3] M. Imai, JAEA-Review 2009-006 (2009) pp.168-180.

[4] J. P. Rozet et al., J. Phys., B22 (1989) pp.33-48; Nucl. Instrum. Methods Phys. Res., B107 (1996) pp.67-70.

[5] K. Shima et al., At. Data Nucl. Data Tables 51 (1992) pp.173-241.

6.2 Zero degree electron spectroscopy of 16 MeV C_2^+ ions

S. Tomita[1], S. Funada[1], Y. Shiina[1], K. Sasa[1], M. Sataka[2], M. Matsuda[2], M. Imai[3] and K. Kawatsura[4]

The yields of secondary electron Y_e induced by swift ions are well known to be almost proportional to the electronic stopping power S_e of incident charged particles, $Y_e = \Lambda S_e$, where Λ is called material parameter. The relation holds in a wide range of materials over four order of incident energy, not only for protons but also for heavy atomic ions[1], except for some special cases. Strong suppression of secondary electron yield for molecular ion beam is one of the examples of the special case. The suppression effect of secondary electron per number of incident atom for 0.5 MeV/atom C_4^+ is almost 50% of that of atomic ion with same velocity[2]. Since the electronic stopping power of C_4^+ is almost same as that of four atomic ions[3], the secondary electron suppression mechanism should be attributed either to the transport of scattered electrons inside material or to the transmission of scattered electrons through the material surface.

Recently, we have reported that the convoy electron yield per incident atom is almost linear to the number of constituent atoms of molecular ion. These electrons can be considered to be mainly generated by the capture of scattered electron to the continuum state of the projectile on the emergence from target surface. Therefore, the result implies that the amount of scattered electrons inside the target material with same velocity as projectile atom should be almost linear to number of constituent atoms of molecular ion. To shed a light on these phenomena related to the transport of scattered electron inside target material, we have performed zero degree electron spectroscopy with swift molecular ions.

The experiments were performed with ion beams provided by the tandem accelerator of the Japan Atomic Energy Agency, Tokai. C_2^+ ions were produced by ECR ion source from benzene gas. The ion source was located on the high voltage terminal of the tandem accelerator. The ions were extracted by potential difference of 10 kV and injected to the normal acceleration beam line by a 90° magnet. The mass selected ions using a 180° magnet on the high voltage terminal, the ions were injected to the acceleration tubes. The accelerated ions were mass selected again by 90° bending magnet and transported to the experimental chamber.

The experimental apparatus used for the present experiment is described elsewhere in detail[4]. The ions were injected on the target of thin carbon foil purchased from Arizona Carbon Foil Co. Inc. The nominal thickness was 3μg/cm^2. On the downstream of the target, 45° tandem parallel-plate spectrometer was placed at zero degrees with respect to the direction of projectile ion beam. The energy resolution of the spectrometer is 3.2% without the deceleration of the electrons before entrance of second analyzer.

The obtained energy spectrum for 16 MeV $C_2^+$is shown in Fig.1. The prominent peak at 366 eV corresponds to the convoy electrons which have same velocity as projectile ions. The other peak at 1.2 keV is the KLL Auger electrons from projectile ions. The energy corresponds to that of C^{3+} ion which was reported to be 230 eV in projectile frame[5]. In addition to the two peaks, there are also two peaks of Coster-Kronig transition,

[1]University of Tsukuba
[2] Japan Atomic Energy Agency (JAEA)
[3] Kyoto University
[4] Kansai Gaidai University

which can be found as a shoulder on the both energy sides of the convoy peak. It is not possible to determine the exact transition channel of the peak, due to poor energy resolution. But the position of peaks agrees roughly with the value reported by Yamazaki et al.[6] for C^{3+}+He collisions.

The electron yields of convoy electron, Coster-Kronig transition, and binary electron for C_2^+ are compared with that for C^+ ion with same velocity and tabulated in Table1. Here we use the yield of KLL Auger electrons for the normalization, because the strong cluster effect is not expected for the inner shell electron excitation process. The cluster effect for the convoy electron yield is 4.3 which does not agree with the linearity reported for 0.5 MeV/atom C_n^+ ions. We think that this value stems from both cluster effect and electron loss from projectile ion, because of rather thin carbon foil thickness. The yield of Coster-Kronig transition also shows cluster effect, which could stem also from thin target thickness. Because the equilibrium charge state of 8 MeV carbon atom is 4.6[7], which is too high to observe Coster-Kronig transition.

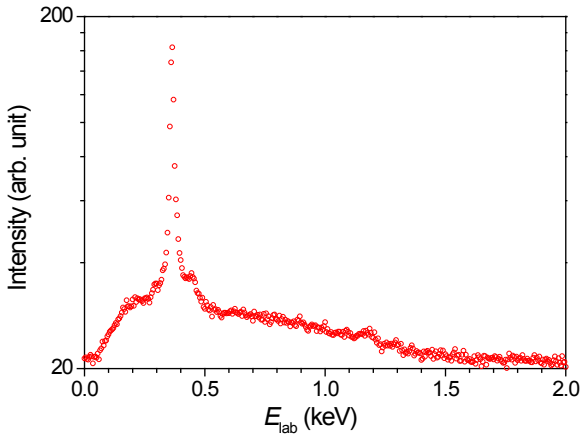

Fig. 1 Energy spectrum of zero degree electrons induced by the irradiation of 16 MeV C_2^+ ions through 3 μg/cm^2 carbon foil.

Table 1. Relative electron yield from 3μg/cm^2 carbon foil. The yields are normalized with that of projectile KLL Auger electrons.

	Convoy electron	Coster-Kronig	Binary electron
$Y\left(C_2^+\right)/Y\left(C^+\right)$	4.3	2.3	0.8

References

[1] H. Rothard et. al., Phys. Rev., A 41 (1990) p.2521.
[2] S. Tomita et. al., Phys. Rev., A 82 (2010) 044901.
[3] S. Tomita et. al., Phys. Rev., A 73 (2006) 060901.
[4] K. Kawatsura et. al., Nucl. Instrum. Methods Phys. Res., B 53 (1991) p.421.
[5] R. Bruch et. al., Phys. Rev., A 31 (1985) p.310.
[6] Y. Yamazaki et. al., Phys. Rev. Lett. 57 (1986) p.992.
[7] K. Shima et. al., Nucl. Instrum. Methods Phys. Res. 200 (1982) p.605.

6.3 Development for measurement of diffusion coefficients in Li ion battery material using ^{8}Li radioactive tracer

H. Ishiyama[1], S. C. Jeong[1], Y. X. Watanabe[1], Y. Hirayama[1], N. Imai[1], H. Miyatake[1], A. Osa[2], Y. Otokawa[2], M. Sataka[2], M. Matsuda[2], H. Makii[2], T. K. Sato[2] and A. Nakao[3]

The diffusion of lithium in materials used in secondary Li-ion batteries, which are under development for the realization of improvement in their battery lifetimes and charge capacities, is a key factor that determines the rate at which a battery can be charged and discharged. We have developed an in-situ lithium diffusion tracing method using a short-lived radioactive ion beam of ^{8}Li and successfully applied it to measure diffusion coefficients in Li ionic conductor (e.g. [1]). This method is sensitive to the diffusion over the micrometer scale and the lower limit of the diffusion coefficients (D) obtained by this method is on the order of 10^{-10} cm^2/s [2]. On the other hand, the diffusion coefficient of Li in $LiCoO_2$, which is used as positive electrode material in most Li secondary batteries, has thus far been measured using several electrochemical approaches indirectly. However, the diffusion coefficients obtained by these approaches are scatter over values from (5 -7) $\times 10^{-8}$ to 5×10^{-14} cm^2/s [3, 4]. It is desirable to directly measure the diffusion coefficients using the improved method which has the nanoscale sensitivity for the lithium diffusion. We have proposed a new method by detecting α particles emitted from decayed ^{8}Li at a small angle relative to a sample surface that is irradiated with a low-energy (the order of keV) ^{8}Li beam, by which the detection limit can be improved to a low value of 1×10^{-12} cm^2/s.

The detailed concept of our proposed method for nanoscale diffusion measurements is given in ref [5]. Here, we introduce the concept of the method briefly. Figure 1 shows the schematic layout of our proposed method. The ^{8}Li decays through β^- emission to ^{8}Be with a half-life of 0.84 s, which immediately decays into two α particles. The implantation energy of ^{8}Li is set to several keV, and consequently, the implantation depth can be set to several tens of nm from a sample surface. The implantation depth profile after several seconds will show a significant amount of broadening as compared with the as-implanted depth profile even for nanoscale levels of diffusion. Further, a solid state Si detector (SSD) for the detection of α particles emitted from decayed ^{8}Li is set at a small angle (θ in Fig. 1) relative to a sample surface. The path length of the detected α particles in the sample increases by a factor of d/sin θ with respect to the depth (d) from the sample surface, thereby leading to a larger change in the measured

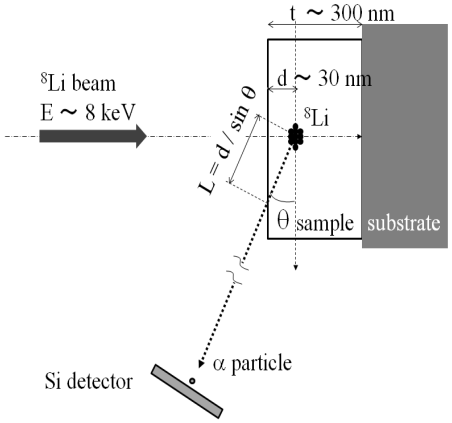

Fig. 1 Schematic layout for the nanoscale diffusion measurement.

[1] High Energy Accelerator Research Organization (KEK)
[2] Japan Atomic Energy Agency (JAEA)
[3] RIKEN

energy spectrum for the α particles than that measured along the implantation direction. The low-side edge of energy spectrum for the α particles emitted at the small angle to the sample surface shows a gradual shift to lower energies with an increase in time due to the ^{8}Li diffusion into the bulk side of the sample. Here, we introduce an energy gate in the lower-energy region of the spectrum. The integrated yields of α particles over a certain gate will increase with time, and this increase corresponds to the effect of Li diffusion.

In order to validate our new method, we have started an experimental program at the tandem facility of JAEA. A low-energy ^{8}Li beam has been provided by an isotope separator on-line (ISOL) at the tandem facility. As the sample, we selected a 400-nm-thick Li_2O-V_2O_5-SiO_2 (LVSO) foil. The diffusion coefficient of an LVSO bulk sample could not be measured below 300℃ by the previous method [2]. Therefore, we selected this sample to verify whether or not to obtain the improved detection limit for diffusion coefficients by this proposed method at the sample temperatures below 300℃. An SSD was set at θ = 10° to the sample surface with the solid angle of 2×10^{-4}. Figure 2 shows time-dependent yields of energy-gated α particles at the temperatures of the LVSO sample ranging from room temperature to 240℃. In order to remove the trivial time dependence of the half-life time of ^{8}Li, the yields, represented by 'Ratio' as a function of time, were normalized by those obtained measured by another SSD at θ = 40° without the energy gate, at which the energy-spectrum for the α particles should be little sensitive to the Li diffusion. As can be seen in Fig. 2, the normalized yields of α particles were observed to show significant changes at the sample temperatures above 60℃. However, after those measurements, the generation of an acicular crystal on the sample surface was observed. It was not clear when it generated. Since the surface roughness of the sample could not be evaluated due to the acicular crystal, it is difficult to determine the precise diffusion coefficients for the sample. In order to verify whether or not to obtain the improved detection limit of the diffusion coefficients by this method, further investigations are required. We will continue experimentally validating our new method.

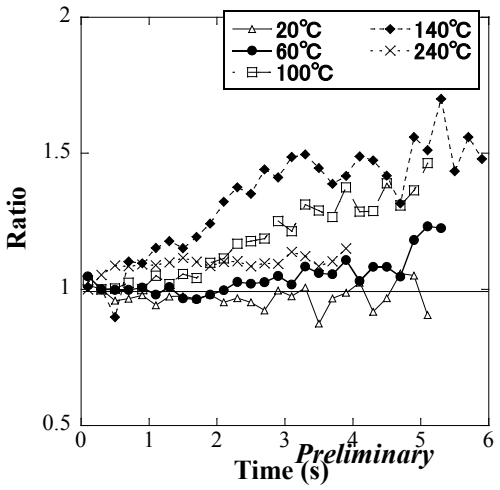

Fig. 2 Time-dependent yields of energy-gated α particles at the temperatures of the LVSO sample ranging from room temperature to 240℃.

References

[1] S. C. Jeong, et al., Solid State Ionics 180 (2009) pp.626-630.
[2] S.C. Jeong, et al., AIP Conf. Proc. 1120 (2009) pp.197-200.
[3] H. Sato, et al., J. Power Sources 68 (1997) p.540.
[4] H. Xia, et al., J. Power Sources 159 (2006) p.1422.
[5] H. Ishiyama, at al., Jpn. J. Appl. Phys. 52 (2013) 010205.

CHAPTER 7

Radiation Effects in Materials

This is a blank page.

7.1 Electronic stopping power dependence of ion-track size in UO_2 irradiated with ions

N. Ishikawa[1], T. Sonoda[2], T. Sawabe[2] and M. Sataka[1]

Uranium dioxide (UO_2) fuels in light water reactors are subjected to various high-energy particles. Not only neutrons but also high-energy fission fragments play an important role in radiation damage process. Since fission fragments have high kinetic energy of about 70~100-MeV, they create radiation damages in UO_2 oxide fuels. Since the radiation damage due to such high-energy heavy particles is dominantly created via high-density electronic energy deposition, the damage creation process is complicated. In order to understand the process, it is useful to utilize high-energy ion accelerator by which the energy deposition density and ion-fluence can be varied in precisely controlled manner.

One of the intriguing characteristics of the radiation damages due to high-energy ion irradiation in UO_2 is the formation of continuous ion tracks along the ion-paths. If the electronic stopping power (S_e) is sufficiently high, the ion-track in nanometer size is created [1-2]. It should be noted here that the ion-tracks created for ion-irradiated UO_2 are not amorphized [1], and it is expected that the S_e-dependence of the ion-track size for amorphized ion-tracks as in ion-irradiated $Y_3Fe_5O_{12}$ [3] and that for non-amorphized ones as in ion-irradiated UO_2 may be different. Therefore, ion-tracks created in UO_2 as one of non-amorphizable materials should be examined in detail.

The disc of UO_2 (diameter: 3 mm, thickness: 0.2–0.4 mm) were prepared from UO_2 powder which was first pressed with 2 t/cm^2 pressure to form pellet shape, and were subsequently sintered at 1740° C for 3 hours in the mixed gas of 40% H_2+N_2. The disc was prepared by Nippon Nuclear Fuel Development Co. Ltd. After sintering of the disc sample, the surfaces of samples were polished to mirror finish. The density of the samples was confirmed to be around 97% of the theoretical density. TEM samples of this sintered UO_2 for ion irradiations were picked up and thinned by focused ion beam (FIB) method using Hitachi FB-2000A at CRIEPI.

The thin specimens were then irradiated with 100 MeV Xe^{25+}, 150 MeV Xe^{27+}, 210 MeV Xe^{29+}, 150 MeV Au^{27+}, and. 310 MeV Au^{27+}. The data for 100 MeV Zr^{10+} and 210 MeV Xe^{14+} obtained by our group [2] are added in the course of the present analysis. The ions were accelerated by the tandem accelerator at JAEA-Tokai. The observation of ion-tracks were performed by 300 kV field emission transmission electron microscope (FE-TEM); Hitachi HF-3000 at CRIEPI.

The electronic stopping power and the projected range were estimated using SRIM-2008. The values of S_e for ion irradiations appeared in previous literatures were recalculated using SRIM-2008 for consistency of the analysis. The estimated S_e values for ions used in the present study are plotted as a function of the specific energy in Fig.1. The ions can be classified into three groups as indicated by three arrows in the figure; (1) E=0.7~0.8 MeV/u (2) E=1.1 MeV/u (3)E=1.5~1.6 MeV/u.

1 Japan Atomic Energy Agency (JAEA)
2 Central Research Institute of Electric Power Industry (CRIEPI)

The S_e-dependence of ion-track size is plotted in Fig.2. The present data (including the data obtained by our previous study[2]) are consistent with the data for 173 MeV Xe irradiation reported in Ref.[1]. This indicates the data for 173 MeV irradiation is reliable, although the specimen in Ref.[1] was annealed at 900ºC after the irradiation. It is clear from the figure that the ion-track size increases monotonically as a function of S_e. In order to take the effect of ion-velocity (the velocity effect)[3] into consideration, it is better to compare ion-track data for different S_e while fixing the ion-velocity (or the specific energy). The ions are categorized into three groups so that each group includes ions with same velocity. Whichever the velocity is chosen, we again find the ion-track size monotonically increases as increasing S_e. It seems that specific energy (or ion-velocity) hardly influences the ion-track size for ion-irradiated UO_2, or the influence is very small, if any, in this energy range (E=0.7-1.6 MeV/u.).

Part of the present work was supported by KAKENHI (21360474).

References

[1] Hj. Matzke, P.G. Lucuta and T. Wiss, Nucl. Instrum. Methods Phys. Res., B166-167 (2000) p.920.
[2] T. Sonoda et al., Nucl. Instrum. Methods Phys. Res., B 268, (2010) p.3277.
[3] A. Meftah et al., Phys. Rev. B 48 (1993) p.920.

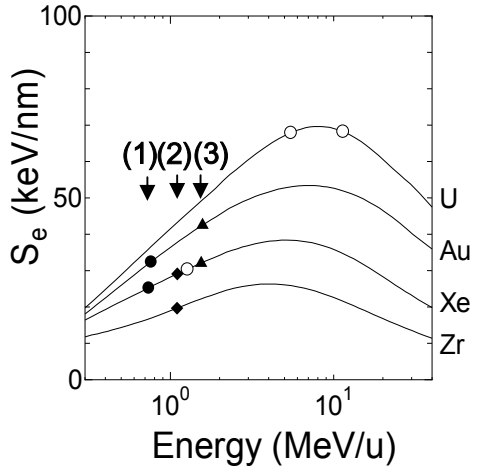

Fig. 1 Electronic stopping power, S_e, as a function of the specific energy in ion-irradiated UO_2. Closed symbols represent S_e for the ions used in the present study and our previous study[2]. Open circles represent S_e for the ions used in the study of Ref.[1]. Three groups of the specific energies are indicated. (See text.)

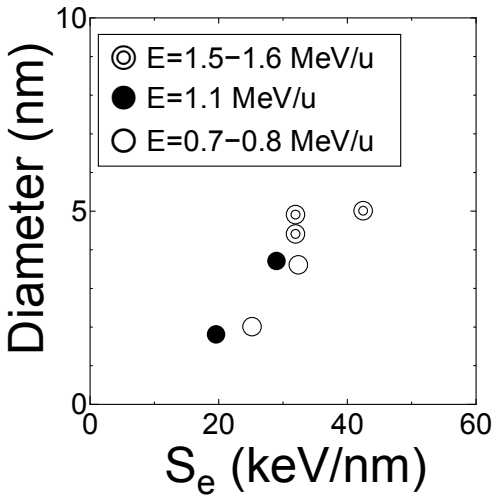

Fig.2 S_e-dependence of the diameter of ion-tracks in ion-irradiated UO_2. The values of specific energy of the ions are indicated in the figure. Part of the data (100 MeV Zr^{10+} and 210 MeV Xe^{14+}) for UO_2 are quoted from our previous paper [2].

7.2 Atomic structure of ion tracks in CeO_2 irradiated with 200 MeV Xe ions

S. Takaki[1], T. Yamamoto[1], M. Kutsuwada[1], K. Yasuda[1], S. Matsumura[1], N. Ishikawa[2], M. Matsuda[2] and M. Sataka[2]

Radiation damage induced by fission products (FPs) is one of the crucial issues for nuclear fuel and transmutation target materials. High-density electronic excitation induced by FPs is known to form continuous ion tracks. This report aims to clarify the structure of ion tracks in CeO_2 irradiated with 200 MeV Xe ions in an atomic scale. Transmission electron microscopy (TEM) and scanning transmission electron microscopy (STEM) techniques, including high-angle annular dark-field (HAADF) and annular bright-field (ABF) imaging are applied to CeO_2 specimens irradiated with 200 MeV Xe ions.

Sintered CeO_2 polycrystalline specimens were irradiated with 200 MeV Xe ions at an ambient temperature. The electronic (S_e) and nuclear (S_n) stopping power of 200 MeV Xe ions was calculated by SRIM code to be 27 keV/nm and 1.1 keV/nm, respectively, at surface region. The irradiated specimens were prepared to be thin-foils by using Ar-ion milling for plan-view observations. Microstructure observations were performed with bright-field (BF) and weak-beam dark-field (WBDF) TEM imaging at 200 kV. A part of specimens was subjected to observations with STEM to obtain Z-contrast images with an atomic resolution by using a TEM equipped with a spherical aberration corrector. HAADF- and ABF-STEM images were utilized for the atomic resolution observations.

Figure 1 (a) shows a high resolution HAADF-STEM image of CeO_2 taken from a [001] direction, which includes an ion track induced by irradiation with 200 MeV Xe ions at the central region of the micrograph with an end-on condition. It is clearly seen that the lattice image of Ce-column with a distance of 0.27 nm, which corresponds to the distance of Ce-ion column to <001> directions as shown in the insertion of Fig. 1 (a), is retained at the core damage region of the ion track. O-ion column surrounded by four Ce ions are not visible because of the large difference in the values of Z between Ce and O ions. The contrast of Ce-ion column is, however, decreased significantly at the core damage region. This is clearly shown in the signal intensity profiles across the ion track to <020> and <200> directions as shown in Figure 1 (b) and (c), respectively, in which the signal intensity at the core damage region of the ion track is depressed for both directions. It is also noted that the background signal intensity increases at the core damage region of ion track, especially for the peripheral region of the ion track. The size of the distorted region, which is defined as the distance between the peaks of back ground intensity, is about 4 nm. A distance where the signal intensity of ion track decreases is evaluated to be 2-3 nm, which fairly agrees with the size of structure-factor contrast observed in WBDF-TEM image and Fresnel contrast in BF image [1,2].

A high resolution ABF-STEM of CeO_2 has detected directly the atomic column of O ions. Figure 2(a) shows an ABF-STEM image of the identical region of Fig. 1(a), which includes an ion track at an end-on

[1] Kyushu University
[2] Japan Atomic Energy Agency (JAEA)

condition. The lattice image at the peripheral region of the ion track is magnified in Fig. 2(b) with a superimposed lattice model of CeO_2 from a [001] direction, in which O-ion columns are apparently evident as black dot-contrast at the tetrahedral site of fcc sublattice of Ce ions. On the other hand, it is seen in Fig. 2(c) that the lattice image of O-ion columns at the core region of the ion track is blurred and/or disappeared. It has been reported that the image of O-ion column strongly depends on specimen thickness. However O-ion columns are visible at the peripheral regions of the ion track for both <200> and <020> directions, although the specimen used in the present study is a wedge shaped one. The blurry and disappearance of O-ion column at the core damage region of the ion track is, therefore, caused by high-density electronic excitation damage with 200 MeV Xe ions. These results clearly show that the oxygen sublattice at the core damage region of ion tracks is significantly disordered, and consistent with results obtained by synchrotron radiation study [3].

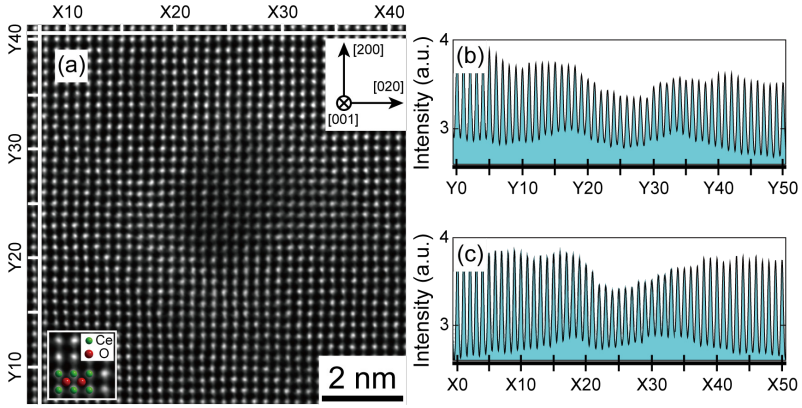

Fig. 1 High resolution HAADF-STEM image of CeO_2 taken from a [001] direction, including an ion track (located at the center of the micrograph) formed under 200 MeV Xe ions irradiation (a). Signal intensity profiles including an ion track are shown in (b) and (c), respectively, for band regions from X20 to X30 (b), and from Y20 to Y30 (c) in Fig. 1 (a).

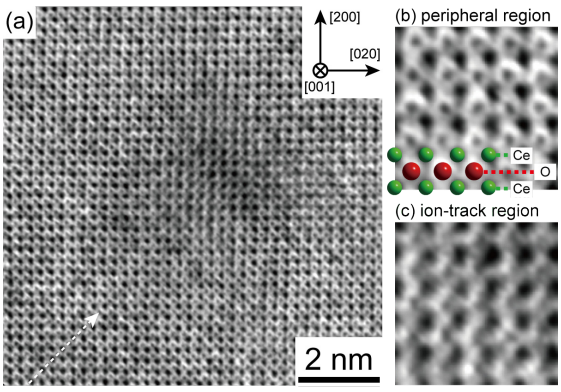

Fig. 2 High resolution ABF-STEM image in CeO_2 for an identical region to Figure 1 (a), taken from a [001] direction (a). Magnified images of the peripheral region (b) and the core damage region of the ion track (c) are also presented. The corresponding atomic configuration is superimposed in magnified image of (b).

References

[1] K.Yasuda et al., Nucl. Instrum. Methods Phys. Res., B314 (2013) p.185.

[2] S.Takaki et al., submitted to Nucl. Instrum. Methods Phys. Res., B (2014), DOI information: 10.1016/j.nimb.2013.10.077.

[3] H. Ohno et al., Nucl. Instrum. Methods Phys. Res., B266 (2008) p.3013.

7.3 Study on effects of high-energy heavy ion irradiation on crystal structure in CeO_2 thin films

T. Kishino[1], K. Shimizu[1], Y. Saitoh[2], N. Ishikawa[2], F. Hori[1] and A. Iwase[1]

In our previous study, pure CeO_2 bulk pellets were irradiated with 200MeV Xe ions and the effects of the irradiation on the lattice structure were measured. The lattice parameter increased with increasing the ion fluence. It is quite interesting if the high density electronic excitation contributes to the production of oxygen vacancies. However, as the projected range of the incident ions is much smaller than the thickness of CeO_2 bulk pellets, effects of ion irradiation are not constant in the specimen, but strongly depend on the depth from the surface. It is, therefore, very difficult to discuss irradiation effects quantitatively. In this study, we prepared CeO_2 thin films. They are much thinner than the projected range of incident ions, and we can obtain nearly uniform irradiation effects in the specimens. In this report, the effect of high energy ion irradiation on the lattice parameter is discussed in terms of the energies deposited through the electronic excitation and the elastic collisions.

Specimens were deposited on Al_2O_3 substrate by the RF magnetron sputtering method for 1.5h. The thickness of the film was 23nm. The lattice structure of the as-deposited CeO_2 thin films specimens was estimated by means of X-ray diffraction. Their lattice parameter before the irradiation was 5.402A, which was slightly smaller than for the bulk pellet (5.411A). Then the CeO_2 thin films were irradiated at room temperature with 10MeV I ions and 200MeV Xe ions. The change in lattice structure of CeO_2 thin film by irradiations was characterized by using a conventional Cu-Kα X-ray diffractometer. The electronic stopping power, nuclear stopping power, and the projected range were estimated by using SRIM-2003. The projected ranges for the two ions are much larger than the film thickness. Therefore, defects are uniformly introduced along the specimen thickness and the possibility of ion implantation effects can be excluded.

Figure 1 shows the fluence dependence of the lattice parameter of the CeO_2 films for 10MeV I and 200MeV Xe irradiations. With increasing the ion fluence, a monotonic decrease in lattice parameter is observed, and the effect of 200MeV Xe ions is larger than that of 10MeV I ions when compared at the same ion fluences. In our previous study, however, the average lattice parameter of CeO_2 bulk was increased by 200MeV Xe irradiation[1][2]. In CeO_2 bulk, the lattice expansion has been explained as originating from the irradiation-induced oxygen deficiencies. When oxygen vacancies were introduced by the irradiation, Ce atoms would be repulsed each other, leading to the lattice expansion.

Finally, the dependence of the lattice parameter of CeO_2 thin films on the deposited energy through electronic excitation is quantitatively discussed. In this discussion, we use the Poisson's law. The Poisson's law is given as;

1 Department of Materials Science, Osaka Prefecture University
2 Japan Atomic Energy Agency

$$L(\varphi) = (L_1 - L_0)\{1 - exp(-aSe\varphi)\} + L_0 \ , \qquad (1)$$

where L_0 is the lattice parameter of CeO_2 before the irradiation, L_1 the saturated lattice parameter, Se the value of electronic stopping power for irradiating ions, and φ is the ion fluence. In eq.(1), aSe is the cross section of the ion track and a is the proportionality coefficient. The fitting result is shown in Fig.2. From the values of a and Se, the diameter of region can be calculated as 2nm for 10-MeV I ion irradiation and 6nm for 200-MeV Xe ion irradiation. In this report, we show that the lattice parameter of CeO_2 thin films decreases by the energetic ion irradiation. This lattice shrinkage has not been observed in bulk CeO_2 specimens. The reason for the irradiation induced lattice shrinkage still remains uncertain. To clarify this phenomenon, we need to study the specimen thickness dependence of the irradiation effect in more detail.

Fig.1

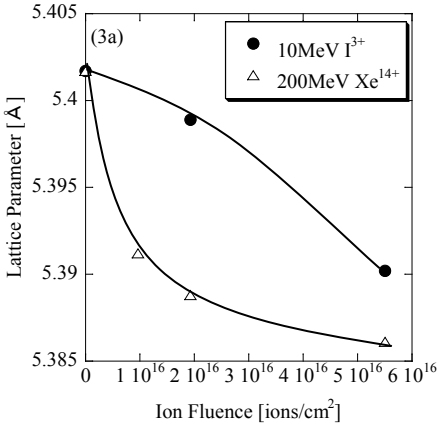

Fig.1 Changes in lattice parameter of CeO_2 thin films by the irradiation with 10-MeV I^{3+} and 200-MeV Xe^{14+}.

Fig.2

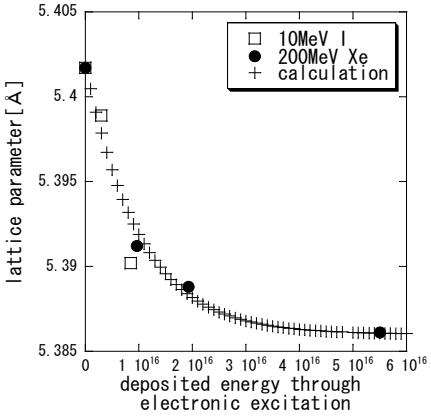

Fig.2 Dependence of lattice parameter on deposited energy density through electronic excitation. Symbols(+) indicate the result calculated by the Poisson's law.

References

[1] K.Shimizu et al., Nucl. Instrum. Methods Phys. Res., B286 (2012) pp.291-294.

[2] Y.Tahara et al., Nucl. Instrum. Methods Phys. Res., B269 (2011) p.886.

7.4 Direct observation of ion tracks in amorphous silicon nitride films by TEM

Y. Morita[1], K. Nakajima[1], M. Tsujimoto[1], S. Isoda[1], M. Mastuda[2],
M. Sataka[2], K. Narumi[2], Y. Saitoh[2] and K. Kimura[1]

When an energetic ion passes through a material, an ion track may be produced along the ion path if the electronic stopping power S_e is larger than a material dependent threshold value. In case of crystalline materials, the ion tracks can be easily observed by transmission electron microscopy (TEM). The track interior is amorphized or comprised of defect clusters depending on the material. In case of amorphous materials, direct TEM observation of ion tracks is generally difficult due to a lack of sufficient contrast. There were a small number of TEM studies on the ion tracks produced in amorphous materials of special kind, namely metallic glasses. Recently, we have demonstrated that ion tracks in amorphous silicon nitride (a-SiN) thin films produced by sub-MeV C_{60} ion impact can be clearly observed using TEM and high-angle annular dark field scanning transmission electron microscopy (HAADF-STEM) [1]. The diameter of the observed tracks is ~ 4 nm, which is larger than the diameter expected from the electronic stopping power. Because the nuclear stopping power is comparable to or even larger than the electronic stopping power for sub MeV C_{60} ions, the result suggests that the nuclear stopping power also plays an important role in the track formation. In this study, the ion tracks produced by 200 MeV Au^{32+} and Kr^{14+} ions were observed to see the effect of the nuclear stopping power on the track formation.

Self-supporting a-SiN films of 30 nm thickness were irradiated with 200 MeV Au^{32+} and Kr^{14+} ions to fluences ~ 1×10^{11} ions/cm^2. After the ion irradiation, TEM and HAADF-STEM observations were performed using a JEOL JEM-2200FS equipped with a field emission gun operating at 200 kV. The samples were held at the specimen tilting holder with the tilt angle from -30 to 30 degrees. The images were taken by GATAN Ultrascan 1000 CCD camera with a 2k × 2k pixel. In HAADF-STEM mode, a narrow electron beam converged to 0.5 nm diameter and an annular dark detector covering over 120 mrad were used.

Figure 1 shows an example of the observed HAADF-STEM image of the a-SiN film iraadiated with 200 MeV Au^{32+} ions. There are circular dark structures of almost uniform diameter of ~ 3 nm. The number of the structures agrees with the fluence of 200 MeV Au^{32+} ions, indicating that single 200 MeV Au^{32+} impacts produce the individual circular structures. The dark contrast of the observed ion tracks indicates that the density of the track interior is reduced compared to the virgin area. The a-SiN films irradiated with 200 MeV Kr^{14+} ions were also observed by TEM and HAADF-STEM. However, no image like Fig. 1 was observed by both TEM and HAADF-STEM. The intensity profiles of the observed HAADF-STEM images of the ion tracks were derived as shown in the inset of Fig. 1. More than 100 profiles were measured and

[1] Kyoto University
[2] Japan Atomic Energy Agency (JAEA)

the averaged radial density profile is shown by a solid line in Fig. 2. The density reduced by 20% at the track center and the density reduced region extends to ~ 1.5 nm from the center. This density reduced region is surrounded by a slightly density enhanced shell region, of which the width is ~ 2 nm. Such a core-shell structure was also observed for the ion tracks in amorphous SiO_2 irradiated with swift heavy ions using small angle X-ray scattering [2]. For comparison the radial density profile of the ion tracks in a-SiN film (20 nm) irradiated with 540 keV C_{60}^{2+} ions is shown by a dashed line in Fig. 2. The density profile of the ion tracks produced by 540 keV C_{60}^{2+} ions is similar to that produced by 200 MeV Au^{32+} ions, but the radius is about 1.5 times larger. The observed track radii and the stopping powers estimated by SRIM code are summarized in Table 1. Although the electronic stopping power of 540 keV C_{60}^{2+} is smallest among these three ions, the track radius is largest, indicating that the track formation is not soley responsible for the electronic stopping power. The total stopping power of 200 MeV Au^{32+} is larger than that of 540 keV C_{60}^{2+} while the track radius is smaller. These facts indicate that the nuclear stopping power is more efficient for the track formation in comparison with the electronic stopping power.

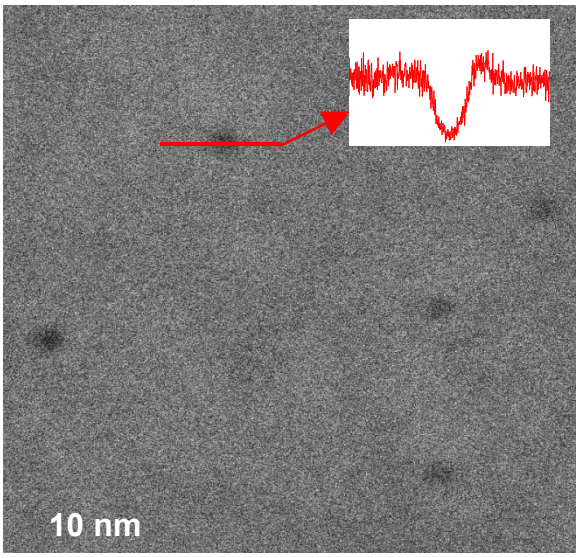

Fig. 1 HAADF-STEM image of a-SiN film irradiated with 200 MeV Au^{32+} ions.

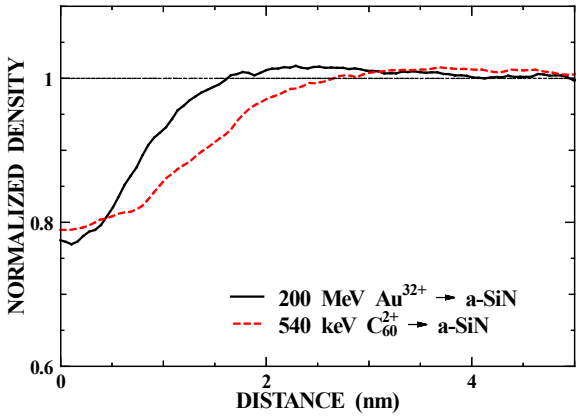

Fig. 2 Radial density profiles of the ion tracks produced by 200 MeV Au^{32+} ions and 540 keV C_{60}^{2+} ions in a-SiN films.

Table 1. Track radii and stopping powers.

.

ion	Radius of ion track (nm)	$(dE/dx)_e$ (keV/nm)	$(dE/dx)_n$ (keV/nm)	$(dE/dx)_{total}$ (keV/nm)
200 MeV Au^{32+}	1.5	24.1	0.2	24.3
200 MeV Kr^{14+}	--	13.1	0.02	13.1
540 keV C_{60}^{2+}	2.3	7.3	9.9	17.2

References

[1] K. Nakajima et al., Nucl. Instrum. Methods Phys. Res., B291 (2012) pp.12-16.

[2] P. Kluth et al., Phys. Rev. Lett. 101 (2008) 175503.

7.5 Threshold fluence of surface amorphization in single crystalline Al_2O_3 induced by swift heavy ions

N. Okubo[1] and N. Ishikawa[1]

Microstructure in single crystalline Al_2O_3 developed during irradiation by swift heavy ions has been investigated. A high energy (swift) heavy ion loses its energy in a medium through two processes, electronic loss and nuclear collisions. The latter process is known to be the dominant mode of energy loss at low ion energies around1 keV/u, and is responsible for direct displacing atoms of the medium from their lattice positions. The electronic energy loss is appreciable at higher energy around 1 MeV/u. In this process, the target atoms are not directly displaced but only excited or ionized. However, it can lead to displacement of lattice atoms in a cylindrical core (ion track) along the ion path in insulating materials. Recently, amorphization in ceramics such as the aluminum oxide, which affects the physical and mechanical properties, is attracted as a phenomenon induced by swift heavy ion irradiations with high-density electronic energy depositions (S_e) [1]. Detailed mechanism of the amorphization induced by swift heavy ion irradiation has not been clearly understood. In this paper, the microstructures of single crystalline Al_2O_3 specimen irradiated by swift heavy ions are investigated by transmission electron microscope (TEM).

Single crystalline Al_2O_3 specimens were irradiated with several energies of Xe ions at ambient temperature, by using the Tandem Accelerator of JAEA, Tokai. The irradiation energy range was from 80 to 160 MeV. The fluences were in the range from 1.0×10^{13} to 1.0×10^{15} ions/cm^2. The specimens used were 10×10 mm^2 plates with 0.5 mm thicknesses. Both surface and backside of specimen were optical grade. After irradiations, XRD measurements and cross sectional TEM observations were conducted. The specimens irradiated by 80 and 160 MeV-Xe were observed by TEM in order to confirm the cross sectional structure in this report.

The TEM observations demonstrated that amorphization was induced in surface region in single crystalline Al_2O_3 irradiated by swift heavy ions. An obvious boundary was observed in the cross sectional TEM image as shown in Fig. 1. The crystal structure of surface region above the boundary was identified as an amorphous phase and the deeper region as a single crystal by electron diffraction patterns. The amorphization was observed around 800 nm depth through from ion-beam incident surface of the specimen irradiated at 3.5×10^{14} ions/cm^2. The projected range (R_p) of the 160 MeV Xe ions in the Al_2O_3 was about 10 μm. The microstructure of the 10 μm depth, where the effect of S_n was maximum, was confirmed as a single crystal. No visible interstitial loops and damage structures were observed around the 10 μm depth. Distinct ion tracks, induced by passing of high energy particles, were vertically observed in depth of single crystalline region as shown in Fig. 1. The diameters of these tracks are sized to be 2–4 nm. The TEM contrast of ion tracks were decayed and disappeared as increasing the specimen depth. These TEM observation results indicate that amorphization could be caused by accumulating and overlapping of ion tracks. In the case of single crystal Al_2O_3, the amorphization depth was shallower than that of the case of

[1] Japan Atomic Energy Agency(JAEA)

polycrystalline Al_2O_3, which was studied in previous work [2], comparing in almost same S_e and fluence. From TEM observations, amorphization depth was determined and the data of single crystal (black circle and square) are shown in Fig. 2 with the data of polycrystalline (open triangle) from Ref. [2]. Amorphization occurs over the fluence of 1.0×10^{14} ions/cm^2. Also the amorphization is supposed to be enhanced by the increasing of fluence in both case of single and poly crystalline Al_2O_3. Comparing almost same fluence, however, the amorphization depth of poly crystal are about twice wider than single crystal as shown in Fig. 2 by dotted lines. These results imply that degree of amorphization induced by high energy ion irradiation depends on not only irradiation conditions but also crystal structure. This may be interpreted by the difference of restriction for phase transfer followed by lattice distortion by electronic excitation in the specimen. In thermal spike model, threshold electronic stopping power S_{et} of amorphization was estimated to be around 10 keV/nm in Al_2O_3 [1]. The 10 keV/nm corresponds to about 7500 nm depth in the 160 MeV Xe irradiation case by SRIM calculation. In the case of single crystal, the thickness of amorphous layer (800 nm) was about 1/10 of the 7500 nm. This implies that amorphization depth should be saturated around depth of S_{et} at following high enough fluence and the amorphization rate could be variable with the balance between track formations and the relaxation rate of lattice distortion and/or re-crystallization rate of amorphous track depending on the crystal structures. It is noted that the amorphous structure is unstable under TEM observation.

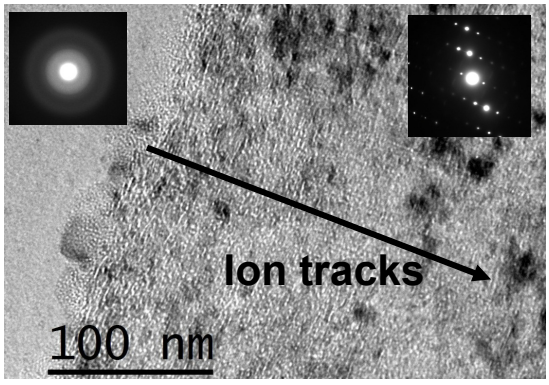

Fig. 1 Boundary between amorphous and crystal structures Al_2O_3
Ion tracks were observed in single crystal region shown as an arrow.

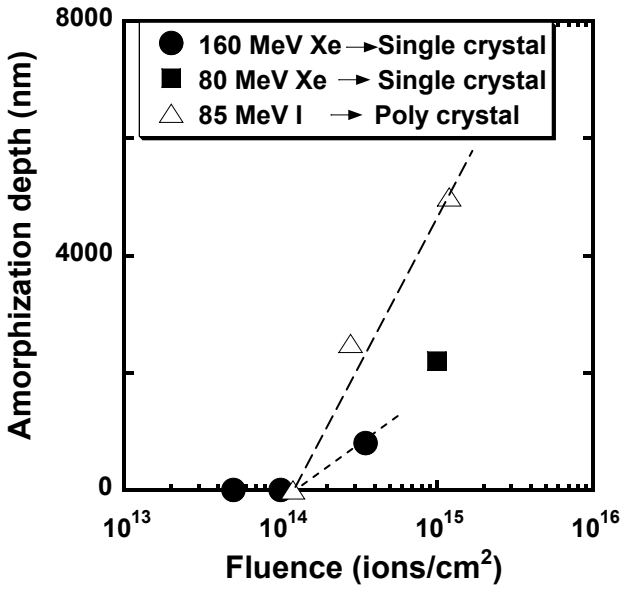

Fig. 2 Fluence dependence of single and poly crystalline Al_2O_3 specimens on amorphization depth
Data of poly crystalline are re-plotted from ref [2].

References

[1] G. Szenes, J. Nucl. Mater., 336 (2005) pp.81-89.
[2] T. Aruga et al., Nucl. Instrum. Methods Phys. Res., B166-167 (2000) pp.913-919.

7.6 Cluster formation in Zeolite using high energy heavy ion irradiation

S. Okayasu[1] and Y. Sasaki[2]

High energy heavy ion bombardment on zeolite films containing exchanged silver ions (Ag-zeolites) causes the structural changes of the films. The crystal structure becomes amorphous along the ion tracks due to high energy transfer from the bombarding ions to the sample. We reported that silver compound clusters are formed 10 - 20 nm in diameter and aligned in the amorphous regions after the bombardments. In this report, we present precise analyses of the phenomena using high resolution Transfer Electron Microscopy (TEM). We deduce the silver compounds and propose a possible formation mechanism of the products.

Figure 1 shows a cross sectional and a plain view of TEM images for an Ag-zeolite sample after heavy ion irradiation (200MeV-Au ions, fluence 1×10^{12} ions/cm^2).

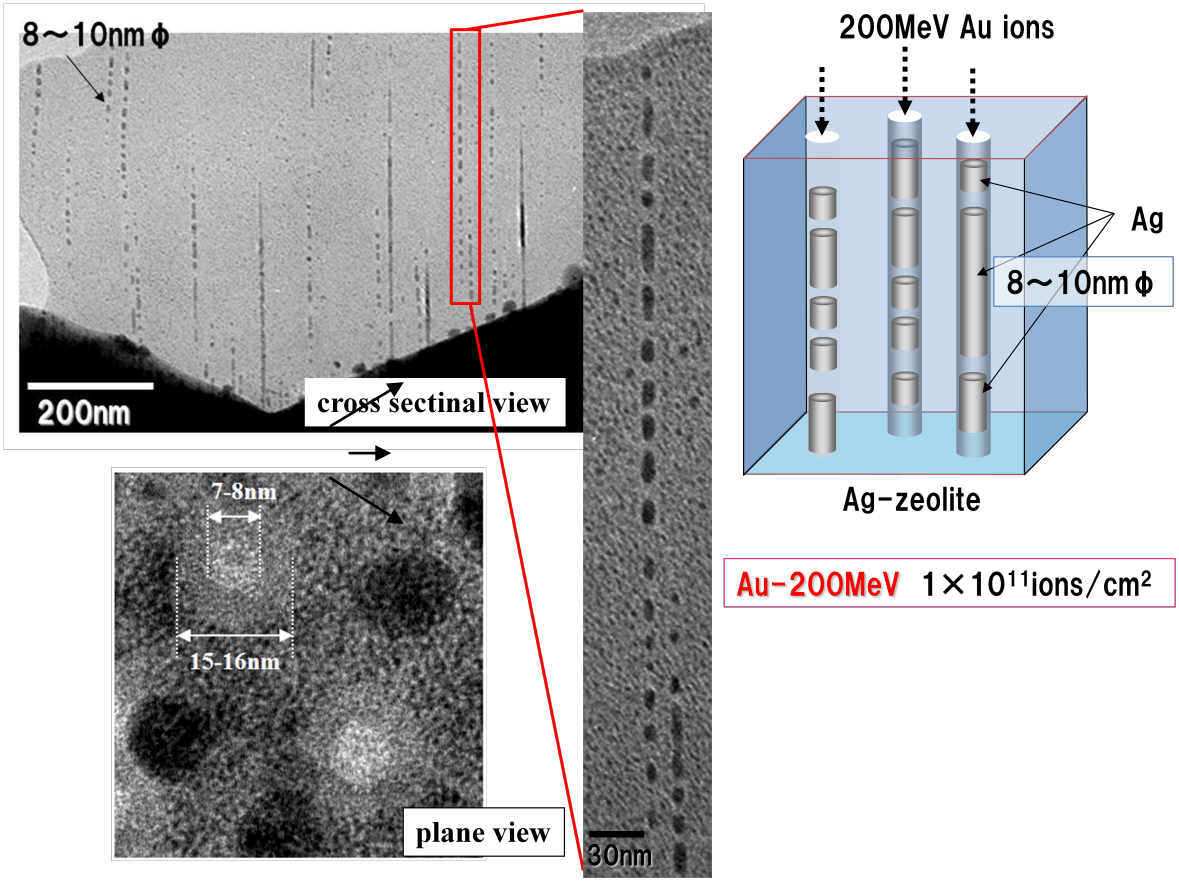

Fig.1 Aligned silver clusters formed along 200MeV-Au ion irradiation tracks.

[1] Japan Atomic Energy Agency (JAEA)
[2] Japan Fine Ceramics Center (JFCC)

Left upper panel is a cross sectional view of a TEM image of Ag-zeolite. Left lower panel is that of a plane view. Right panel illustrates a schematic diagram for the formation of aligned silver clusters by heavy ion irradiations.

Dark shade regions are silver compounds. From the plain view image, amorphous areas due to the heavy ion bombardment grow to about 20 nm in diameter, twice for those of silver compounds. The observed silver compounds can be considered as silver oxides Ag_2O if silver ions within the amorphous areas are condensed to the silver compound clusters. Assuming the compounds as metals, the zeolite films can be expected to be conductive. However, the film remains in an insulator, and this fact is consistent with the assumption that the compound is Ag_2O. There is no direct evidence to identify the compounds at this time, we can propose a possible formation mechanism of the compounds as shown in Fig. 2, if it can be assumed that the products are Ag_2O.

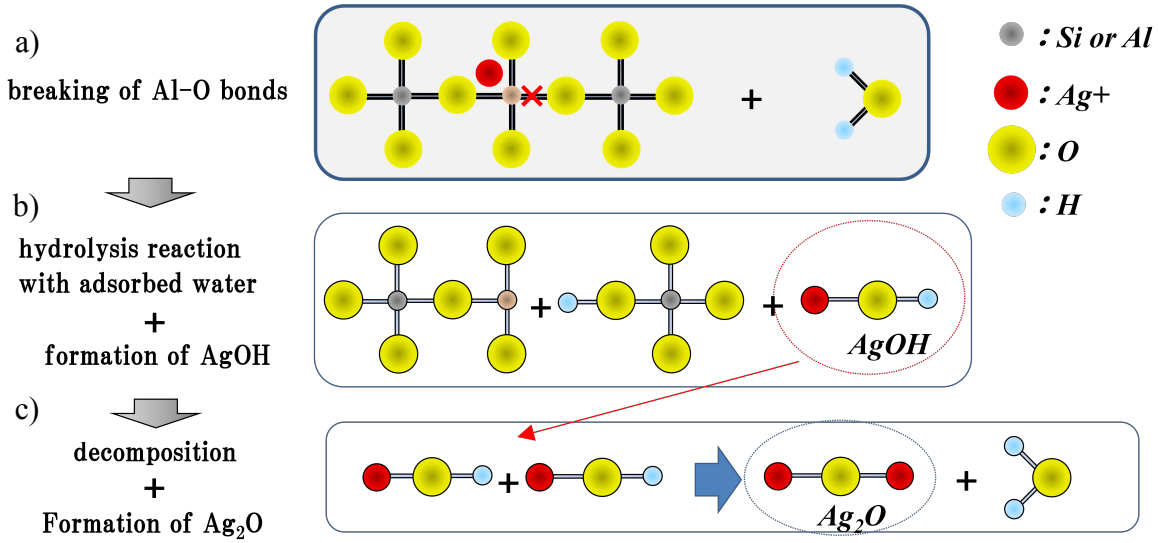

Fig.2 Ag_2O formation mechanism by ion-irradiation.

a) A breakdown of an Al-O bond occurs within an amorphous track due to the irradiation.
b) A hydrolysis reaction between an adsorbed water molecule and an adsorbed Ag^+ ion occurs, and a AgOH molecule is formed.
c) Decompotision of two AgOH molecules occurs, and an Ag_2O molecule is formed. The formed Ag_2O molecules are aligned along the track.

7.7 Ion irradiation effects on Mn-doped ZnO films

N. Matsunami[1], M. Itoh[1], S. Okayasu[2], M. Sataka[2] and H. Kakiuchida[3]

The authors have investigated electronic excitation effects on the electrical resistivity, optical absorption and atomic structure of In-doped ZnO (IZO) [1] and Al-doped ZnO (AZO) [2]. In this report, studies of property modifications by high-energy ions have been extended to Mn-doped ZnO.

Mn(6%)-doped ZnO films have been prepared by using a RF-magnetron sputter deposition method [1] on C-plane-cut-Al_2O_3-substretes (CALO) at 250 ºC for magnetic property studies (CALO was used to reduce the influence of the substrate) and on SiO_2-substrates at 500 ºC (MZO/SiO_2) for atomic and electronic structure studies. Rutherford backscattering spectroscopy (RBS) of 1.8 MeV He^+ ions with the stopping power [3] and the density of $4.2x10^{22}$ cm^{-3} shows that the composition of MZO films is close to stoichiometric and Mn/Zn 6±1 %, and thickness of MZO/CALO and MZO/SiO_2 is ~1 and 0.13 μm. It appears that the composition remains unchanged under 100 MeV Xe ion impact. X-ray diffraction (XRD) shows that MZO films are polycrystalline with c-axis orientation.

Temperature (T) dependence of magnetic susceptibility (χ) of MZO is shown in Fig. 1 and it is found to follow the Curie law (i.e., paramagnetic): $\chi = \chi_o + C/T$, C being the Curie constant. Total angular momentum J in units of ħ is reduced using the relation [4]: $C = NJ(J+1)g^2\mu_B^2/3k_B$. Here, g=2.0, μ_B the Bohr magneton, k_B the Boltzman constant, N the Mn concentration and Mn only is assumed to contribute to paramagnetism. J vs ion fluence is shown in Fig. 2. It is found that the fluence dependence of J is similar for both 100 MeV Xe and 90 MeV Ni ions, in contrast to the XRD results described below. J decreases from 2 to 3/2 under the ion impact and this corresponds to valence modification of Mn^{3+} into Mn^{4+}. Measurement of Mn valence modification using other method, e.g., XPS is under way.

For 100 MeV Xe ion impact on MZO/SiO_2, it appears that the XRD intensity decreases to a half of that unirradiated at $25x10^{12}$ cm^{-2} and 1/50 at $5x10^{14}$ cm^{-2} and lattice constant of c-axis decreases by 0.6 % for the fluence > $1x10^{13}$ cm^{-2}. These indicate lattice disordering and amorphization by the ion impact. For 90 MeV Ni ion impact on MZO/SiO_2 up to $20x10^{12}$ cm^{-2}, effects are smaller than those by 100 MeV Xe ion impact. It can be understood that these effects are caused by the electronic energy deposition and the electronic stopping power of 90 MeV Ni is smaller by a factor of 1.5 than that of 100 MeV Xe (see Table 1). For 100 MeV Xe ion impact on MZO/C-Al_2O_3, the fluence dependence of the XRD intensity, and lattice compaction is similar to those of MZO/SiO_2, indicating that ion impact modifications of atomic structure are independent of substrate.

It is found that the bandgap modification of MZO/SiO_2 by 100 MeV Xe for the fluence up to $2x10^{14}$ cm^{-2} and 90 MeV Ni ions up to $2x10^{13}$ cm^{-2} is very small (<0.02 eV) in contrast with the case of In-doped ZnO (bandgap increases by 0.25 eV at 100 MeV Xe ions at 10^{14} cm^{-2} [1]). Hence, disordering of MZO lattice does not affect the bandgap modification by the ion impact.

1 Division of Energy Science, EcoTopia Science Institute, Nagoya University
2 Japan Atomic Energy Agency (JAEA)
3 National Institute of Advanced Industrial Science and Technology (AIST)

The electrical resistivity of unirradiated MZO films is ~ 1 MΩcm and much larger (~ 6 order of magnitude) than that of IZO (0.03 to 10 Ωcm) [1] and AZO (0.1 to 0.5 Ωcm) [2]. It appears for 100 MeV Xe impact that the resistivity reaches minimum of 40 Ωcm at $3x10^{12}$ cm^{-2}. The lowest resistivity is much larger than that of IZO ($2x10^{-3}$ Ωcm) at 1-$4x10^{14}$ cm^{-2} and that of AZO (0.1 Ωcm) at $2x10^{13}$ cm^{-2}, and achieved at smaller fluence. The reduction of the resistivity by the ion impact (4 order of magnitude) is similar for these three films (MZO, IZO and AZO) and hence, it is reasonably concluded that the resistivity reduction of MZO by the ion impact is due to ion-induced dopant replacement as in the case of IZO and AZO. The resistivity before ion impact is too high to measure the Hall effect and temperature dependence. In view of ionic radius, dopant-replacement looks easy, though the ion-induced mechanism has not been established yet. Here, ionic radius in 4 coordinates of Zn^{2+}, Mn^{3+}, Mn^{4+}, In^{3+} and Al^{3+} is 0.074, 0.066, 0.06, 0.076 and 0.053 nm [5]. When Zn^{2+} is replaced by Mn^{4+}, it is anticipated more O vacancy generation leading to donor levels. Fraction of replacement of Zn cite by Mn and effect of Mn^{4+} on donor generation are to be investigated.

Table 1 Projected range (R_p), electronic (S_e) and nuclear (S_n) stopping powers near surface of ZnO for 100 MeV ^{136}Xe and 90 MeV ^{58}Ni ions in ZnO calculated using TRIM1997 [3].

Ions	R_p(μm)	S_e(keV/nm)	S_n(keV/nm)
100 MeV Xe	9.4	21.1	0.195
90 MeV Ni	9.2	14.6	0.031

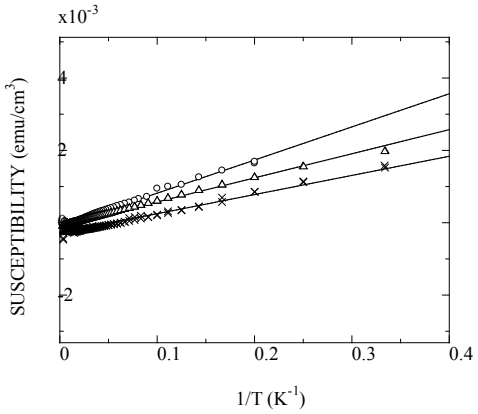

Fig. 1 Magnetic susceptibility of Mn-doped ZnO on C-Al_2O_3 vs 1/T, T being temperature (K), for unirradiated (○), 100 MeV Xe at $2x10^{12}$ cm^{-2} (Δ), $1x10^{13}$ cm^{-2} (x).

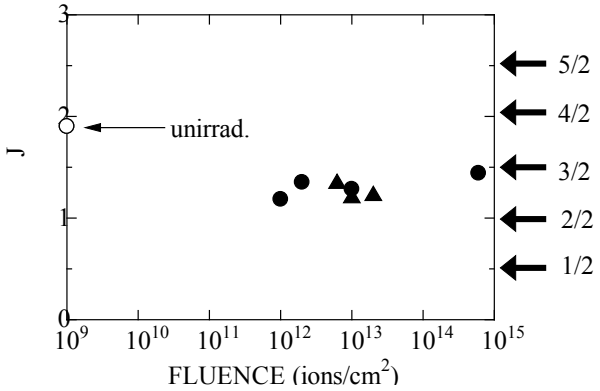

Fig. 2 Total angular momentum J in unit of ħ (Planck constant divided by 2π) vs fluence of 100 MeV Xe (●) and 90 MeV Ni (▲). J=2 and 2/3 correspond to Mn^{3+} and Mn^{4+}.

References

[1] N. Matsunami et al., Nucl. Instrum. Methods Phys. Res., B268 (2010) p.3071.
[2] O. Fukuoka et al., Nucl. Instrum. Methods Phys. Res., B250 (2006) p.295.
[3] J. F. Ziegler et al., The Stopping and Range of Ions in Solids, Pergamon Press, 1985.
[4] C. Kittel, Introduction to Solid State Physics, John Wiley & Sons, 5th ed. 1976.
[5] E. Barsoum, Fundamentals of Ceramics, McGraw-Hill, 1997.

7.8 Shape and property control of nanoparticles by swift heavy ion irradiation

H. Amekura[1], N. Okubo[2] and N. Ishikawa[2]

While various metal species of spherical nanoparticles (NPs) in amorphous silica show shape elongation under swift heavy ion irradiation [1], it was reported for Ag NPs that the elongated shapes recovered to the spherical ones under thermal annealing [2]. Since a spherical shape has the minimum surface area under a constant volume, primary this behavior could be ascribed to a minimization of the interface energy between the particle and the matrix. However, if the matrix was very stiff even at the elevated temperatures, the elongated NPs could not return to the spherical shapes even in a molten form.

The thermal shape recovery from the elongated shapes to spherical ones were studied in NPs with a low melting point (Zn, m.p. ~420°C) and those with a high m.p. (V, m.p. ~1890°C) [3]. Spherical Zn and V NPs were fabricated in different pieces of silica glass by implantation of Zn and V ions of the same energy of 60 keV. Both the NPs were irradiated with 200 MeV Xe^{14+} ions up to a fluence of 5.0×10^{13} ions/cm^2 with an incident angle of 45 deg from the sample surface. Isochronal annealing was carried out in a vacuum ($< 3 \times 10^{-3}$ Pa) between 200 and 1000°C in steps of 100°C for 10 min each. The degree of the elongation was evaluated by linearly polarized optical absorption spectroscopy [4] at room temperature (RT).

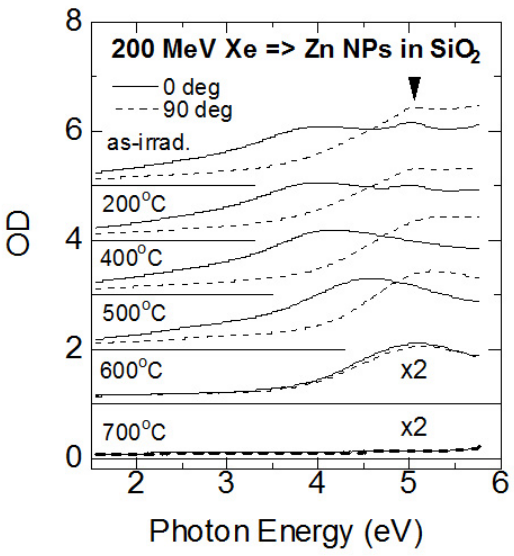

Fig. 1. Optical density (OD) spectra of Zn NPs in silica irradiated with Xe ions of 200 MeV to a fluence of 5.0×10^{13} ions/cm^2 and annealed in a vacuum isochronally for 10 min at each temperature. The triangle indicates an absorption band due to radiation-induced defects in the silica. The solid (broken) lines indicate the spectra measured with linearly polarized light at a polarization angle of 0 (90) deg. The spectra are vertically shifted from each other for clarity; the horizontal lines indicate the baselines.

Figure 1 shows changes in optical density (OD) spectra of the elongated Zn NPs in silica with the isochronal annealing. The spectra were measured at RT after each annealing, using linearly polarized light at the two different polarizations of 0 and 90 deg from the elongation plane. In the as-irradiated state, the

[1] National Institute for Materials Science (NIMS)
[2] Japan Atomic Energy Agency (JAEA)

spectra obtained at 0 and 90 deg were very different from each other, indicating the elongated shapes of the NPs. The spectrum at 0 deg showed a pronounced low energy shift compared with that at 90 deg. With increasing the annealing temperature, the 0 deg spectrum gradually shifted toward the 90 deg spectrum, indicating a decrease in the aspect ratios of the elongated NPs. After the annealing at 600°C, both the spectra became almost identical, indicating the recovery to the spherical shapes of the NPs. An important observation was that the Zn NPs were still in elongated shapes even after the annealing at 500°C, while the m.p. of bulk Zn is 420°C. In fact, we have once experimentally evaluated the m.p. of unirradiated spherical Zn NPs by rapid X-ray diffraction at high temperatures using synchrotron radiation [5]. The observed m.p. of the NPs was the same as the bulk one within experimental error [5]. Since m.p. of NPs are usually comparable to or lower than the bulk value, we concluded that the Zn NPs at 500°C are in a molten form with keeping the elongated shapes, probably due to the mold effect of the silica matrix.

In the case of vanadium NPs, the elongation signal was stable up to 800°C, but steeply decreased at 900°C and mostly disappeared at 1000°C. Since the m.p. of bulk vanadium is 1890°C, the recovery from the elongated shapes to spherical ones was induced in a solid phase in the case of vanadium NPs. It is reported that the diffusion of various metal atoms, such as Cu [6], Zn [7], Er [8], Eu [9] and Tb [10], in silica is enhanced around 800-1000°C, probably due to the softening of the silica matrix, which possibly assists the recovery of the elongated V NPs to spherical shapes.

References

[1] M. C. Ridgway et al., Phys. Rev. Lett., 106 (2011) 095505.
[2] V. Rodriguez-Iglesias et al., Opt. Lett., 35 (2010) pp.703-705.
[3] H. Amekura et al., Nanotechnology 23 (2012) 095704.
[4] H. Amekura et al., Phys. Rev., B 83 (2011) 205401.
[5] H. Amekura et al., J. Appl. Phys. 108 (2010) 104302.
[6] H. Amekura, and N. Kishimoto, J. Appl. Phys. 94 (2003) pp.2585-2589.
[7] H. Amekura et al., Nanotechnology 18 (2007) 395707.
[8] A. Polman et al., J. Appl. Phys. 70 (1991) pp.3778-3784.
[9] N. Can et al., J. Appl. Phys. 78 (1995) pp.6737-6744.
[10] H. Amekura et al., J. Appl. Phys. 84 (1998) pp.3867-3871.

7.9 Enhancement of critical current density by hybrid effect of flux pinning in heavy-ion irradiated high-T_c superconducting thin films

T. Sueyoshi[1], T. Kotaki[1], T. Fujiyoshi[1], F. Mitsugi[1], T. Ikegami[1] and N. Ishikawa[2]

For development of second generation "coated conductors" using $REBa_2Cu_3O_y$ (REBCO, RE: Rare Earth element) films, further improvement of critical current density J_c in magnetic field is indispensable. One-dimensional (1D) pinning centers (PCs), such as columnar defects (CDs), are most effective to immobilize the flux lines in REBCO. The flux pinning of the 1D-PCs, however, is weakened substantially when a magnetic field is inclined off the direction of 1D-PCs. In addition, the flux pinning of the 1D-PCs is accompanied by the formation of double kinks between adjacent CDs, which induces the movement of flux lines to the next CDs with no energy barrier [1]. In contrast, three-dimensional (3D) PCs such as nano-particles have the morphology with no preferential direction for flux pinning. In addition, it is expected that the 3D-PCs coexisting with 1D-PCs improve the anisotropy of J_c and suppress the motion of the double kinks, known as "hybrid flux pinning". For the hybrid flux pinning, 3D-PCs residing between 1D-PCs efficiently act as assistant PCs, whereas 3D-PCs are distributed from place to place in various sizes. In order to customise the spatial and the size distributions of 3D-PCs in REBCO films, we have fabricated quasi-multilayered films of $BaZrO_3/YBa_2Cu_3O_y$ (BZO/YBCO) using a multilayering process in a pulsed laser deposition (PLD) method [2]. In the multilayered films, the BZO precipitates can be formed into the nano-particle shape, the density and the spatial distribution of the nano-particles can be tunned by the growth temperature [2]. In this work, CDs are introduced by using 200 MeV Xe ion irradiations along the *c*-axis direction into the BZO/YBCO quasi-multilayered films grown at different temperatures, in order to elucidate the influence of 3D-PC configurations on the hybrid flux pinning system.

The quasi-multilayered YBCO films with BZO were fabricated on (100) $SrTiO_3$ substrates by a PLD technique alternating a YBCO target and a BZO target [2]. During the deposition, the growth temperature T_s was 780 °C or 810 °C. In this work, the laser pulse on the BZO target is 1 pulse and the multilayered films consists of 60 bilayers of BZO/YBCO, where the film thickness is about 260 nm. The multilayered films were irradiated with 200 MeV Xe ions at the tandem accelerator of JAEA in Tokai, Japan. The incident ion beam was directed parallel to the *c*-axis of the films, introducing the CDs as the *c*-axis correlated PCs. The electronic stopping power S_e is about 2.8 keV/Å, which produces the CDs of about 8 nm in diameter within YBCO [3]. The total densities of CDs correspond to the dose equivalent matching field B_ϕ = 3 T. The transport properties were measured using a four-probe method in evaluating the J_c properties. The transport current was always applied in the direction perpendicular to the magnetic field.

Figure. 1 shows the angular dependences of J_c at 65 K for 1 T and 3 T in the multilayered films for pre- and

[1] Kumamoto University
[2] Japan Atomic Energy Agency (JAEA)

post-irradiation, where θ is defined as the angle between the magnetic field and the *c*-axis of the films. For the pre-irradiation, there is no peak at any angles except for $\theta = 90°$ in the 780°C film, while a broad peak of J_c centered at $\theta = 0°$ occurs in the 810°C film (Figure. 1(a)). The former is typical of random pinning, that is, the BZO in the 780°C film is randomly distributed as 3D-PCs with no preferential direction for the flux pinning. The latter case, on the other hand, seems to be nature of the *c*-axis correlated flux pinning, though the nano-particles of BZO are disconnected by a YBCO layer along the thickness direction. After the irradiation, a pronounced peak of J_c around $\theta = 0°$ emerges for both 1 T and 3 T, regardless of the growth temperature, as shown in Figures 1(c) and (d). This originates from the *c*-axis correlated pinning by the introduced CDs. There is little difference in the height or the width of the peaks between the 780°C film and the 810°C one for $B = 1$ T, although the behaviours of J_c around $\theta = 0°$ are substantially different from each other before the irradiation. Increasing the magnetic field, on the other hand, the difference of the J_c between both samples stands out around $B \parallel c$-axis. The difference of the J_c between the 780°C film and the 810°C one would result from the size of the BZO nano-particles for the most part. At lower T_s, the density of surface steps or kinks is higher, which suppresses the migration of adatoms to the preferred adsorption sites and promotes the fragmentation of the nucleus [4]. Then, the BZO crystals in the 780°C multilayered film would be relatively small particles, which are hard to work as the effective 3D-PCs for the pinning of the kinks of flux lines, compared to the 810°C one. Therefore, the J_c of the 810°C film is larger than that of the 780°C one in a wide rage of magnetic field orientation. For lower magnetic field below the matching field B_ϕ, on the other hand, the flux lines are mostly captured by CDs, so that the flux pinning of BZO nano-particles would not stand out. Then, there is not much difference in the J_c between the 780°C film and the 810°C one.

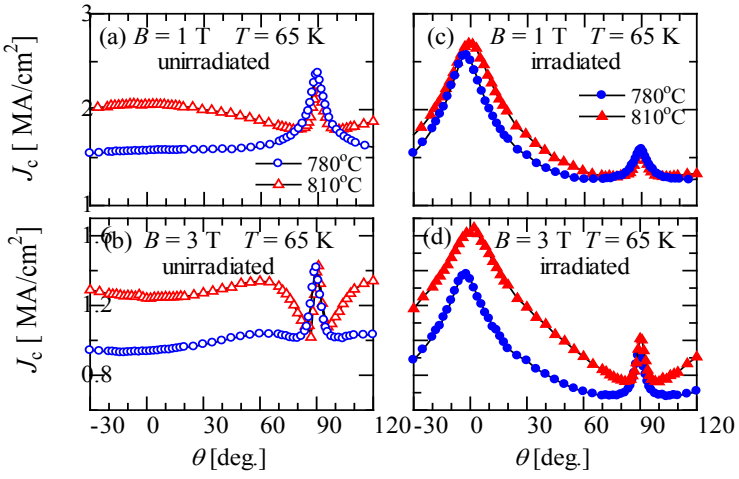

Fig. 1 Angular dependences of J_c in multilayered films with 60 bilayers before and after irradiation.

References

[1] D. R. Nelson and V. M. Vinokur, Phys. Rev., B 48 (1993) pp.13060-13097.

[2] T. Sueyoshi et al., Physica C 484 (2013) p.134.

[3] K. Nakashima et al., Physica C 463-465 (2007) p.665.

[4] H. Kai et al., Supercond. Sci. Technol. 23 (2010) 025017.

7.10 Application of high-aspect-ratio nanoholes formed by etching of latent tracks for sensors

M. Fujimaki[1], M. Sataka[2] and M. Matsuda[2]

An evanescent-field-coupled waveguide-mode (EFC-WM) sensor is one of the highly-sensitive molecular detection sensors [1]. Figure 1 shows a schematic showing the setup of the sensor. The EFC-WM sensor is capable of detecting modifications in the dielectric environment near the waveguide surface. A monolithic sensing plate for the EFC-WM sensor consisting of a SiO_2 glass substrate, a thin single crystalline Si layer, and a SiO_2 glass waveguide shows a superior sensitivity and stability [2]. The sensitivity of the EFC-WM sensor can be enhanced by perforating the waveguide layer [2]. One of the promising perforation methods is a method that utilizes selective etching of latent tracks formed by swift heavy ion irradiation. However, uniform swift heavy ion irradiation in large area, such as a 10 cm square or larger, has not been accomplished. In the present research, to realize the mass-production perforating process, we tried to establish an ion irradiation process that can irradiate swift heavy ions in large area uniformly.

The beam line that we used was the line L2 of the 20 MV tandem accelerator at JAEA-Tokai. The ions used were 200 MeV Xe ions. The ion beam was made to be wide in the X direction by scanning it using an electromagnet (IDX Corporation). Samples to be irradiated were the monolithic sensing plate with a layered structure of 84-nm Si and 480-nm SiO_2 on a 1.2-mm-thick SiO_2 substrate (See Fig. 2). The sensing plate was cut into a plate of 14×18 mm. Nine plates were placed on a sample holder in line as shown in Fig. 3. Figures 4(a) and 4(b) show a schematic and a photograph of the sample holder, respectively. Uniform large-area irradiation was attempted by moving the sample holder 150 mm up and down during the irradiation as shown in Fig. 4(a). The moving speed was about 1mm/s. The ion fluence was monitored by integrated ion-beam current measured on the sample holder. The irradiated plates were then perforated by soaking them in a 4.8% aqueous solution of hydrofluoric acid (HF) for 2 min. The resulting nano holes were observed by scanning electron microscopy (SEM; Hitachi High-Technologies, S4800).

Figure 5 shows the intensity of the ion beam current along the X direction on the sample holder. As can be seen, the beam profile was quite uniform with its scanned width of 40 mm. Figure 6 is an example of the SEM image of the perforated waveguide, where the average diameter of the nanoholes was 70 nm. The density of nanoholes aimed in the irradiation experiment was 100 μm^{-2}, whereas the average density of nanoholes observed by the SEM was 46 μm^{-2}, which might be due to overestimation of ion fluence because of the effect of secondary electrons. The deviation of the density of nanoholes from the average density was within ±10%. The deviation is ideally 0%. In the previous experiment [3], however, the deviation was more than ±50%, indicating that the deviation was improved in the present experiment very much. This is owing to the uniformity of the incident ion beam. However, unsymmetrical distribution of nanoholes along the X

[1] National Institute of Advanced Industrial Science and Technology (AIST)
[2] Japan Atomic Energy Agency (JAEA)

direction was observed, which might be due to that the ion beam did not pass the center of the scanning magnet. In order to obtain expected sensitivity, the deviation must be within 5%. Further improvement of the optics of the ion beam and the method to estimate the fluence is required.

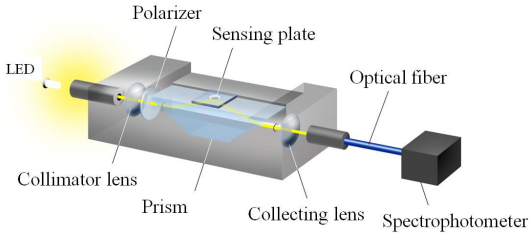

Fig. 1 Schematic showing the setup of the sensor.

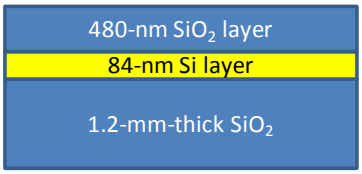

Fig. 2 Schematic of the layered structure of the sensing plate.

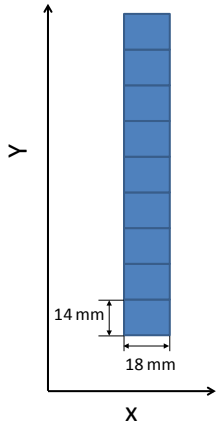

Fig. 3 Alignment of the sample plates on the sample holder.

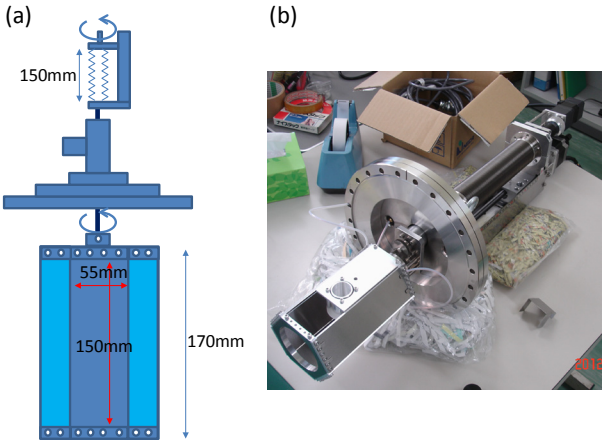

Fig. 4 Schematic (a) and photograph (b) of the sample holder.

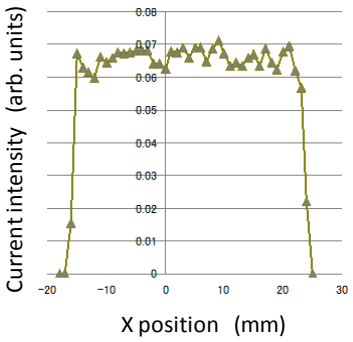

Fig. 5 Intensity of the ion beam current along the X direction on the sample holder.

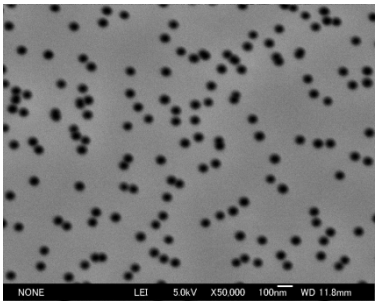

Fig. 6 SEM image of the perforated waveguide.

The authors would like to thank the Advanced Functional Materials Research Center of Shin-Etsu Chemical Co., Ltd. for supplying the sensing plate.

References

[1] M. Fujimaki et al., Microelectron. Eng. 84 (2007) p.1685.

[2] M. Fujimaki et al., Opt. Express 16 (2008) p.6408.

[3] M. Fujimaki et al., JAEA-Tokai Tandem Annu. Rep. 2011, JAEA-Review 2013-002 (2013) p.64.

7.11 Evaluation of radiation tolerance of microprocessor by heavy ion irradiation

Y. Chiba[1], E. Asai[1], H. Tomioka[1], T. Kameda[1], M. Sataka[2] and M. Matsuda[2]

Nowadays, many microprocessors are used in various fields such as amateur hobbies, consumer electronics, industrial automation *etc*. For examples, AVR microprocessors manufactured by Atmel Corporation are well-known for their availability, low price, and free development environment. From the other point of view, Ferroelectric Random Access Memory (FRAM) attracts notice as a superior radiation tolerant device in aerospace field. In micro-satellite field, although the various challenging missions are performed by universities, companies *etc.,* even now new type microprocessors are not utilized due to limited radiation tolerance data and no previous actual operation achievements in space environment. For those reasons, PIC microprocessors with some success in space are still mainly used conservatively in university satellite projects such as CubeSat without further investigation. The authors investigate radiation tolerance of ATmega128A (AVR) to evaluate whether the AVR can be used in the micro satellites. Moreover, the authors also show the radiation tolerance of PIC16F877A (PIC) and MSP430FR5739 (MSP) for comparison.

Table 1 shows device properties of processors under the irradiation experiments. As a reference, we also include the properties of PIC and MSP subjected to the experiments in Takasaki Advanced Radiation Research Institute, JAEA. In the AVR experiment, heavy ions were irradiated by using the Tokai Tandem Accelerator. The heavy ions irradiated to the AVR were 70MeV-$^{37}Cl^{8+}$ and 150MeV-$^{81}Br^{12+}$. To evaluate radiation tolerance, single event upset (SEU) were counted, and the cross section of each device was calculated. The cross section $\sigma_{\mathrm{hi}}(L)$ (cm^2/bit) is obtained by the equation:

$$\sigma_{hi}(L) = \sigma_s \left[1 - \exp\left\{ -\left(\frac{L - L_{th}}{W} \right)^s \right\} \right], \quad (1)$$

where σ_s and L_{th} are a saturated cross section and a threshold Linear Energy Transfer (LET), respectively. W and s are the constants determining the shape of Weibull function. The LETs of each heavy ion are obtained by SRIM software.

LET – Cross section relationship for AVR is shown in Fig. 1. As a reference, LET – Cross section relationships for PIC and MSP are also shown in Fig. 2 and Fig. 3, respectively. According to the result, both saturated cross section and threshold LET of AVR is almost the same as PIC. The frequencies of the SEU of the both devices on the planned orbit (400 km altitude, 65 degrees inclination) were evaluated by the online software, CRÈME 96 [1]. The frequency of the AVR was 2.97×10^{-7} SEUs/bit/day. On the other hand, the frequencies of the PIC and MSP were 2.33×10^{-7} SEUs/bit/day and 3.40×10^{-9} SEUs/bit/day,

[1] University of Tsukuba
[2] Japan Atomic Energy Agency (JAEA)

respectively. It was confirmed that the frequency of the SEU of the AVR is almost the same as PIC. According to SEU simulation on the planned orbit, the AVR has the same radiation tolerance compared with PIC microprocessor.

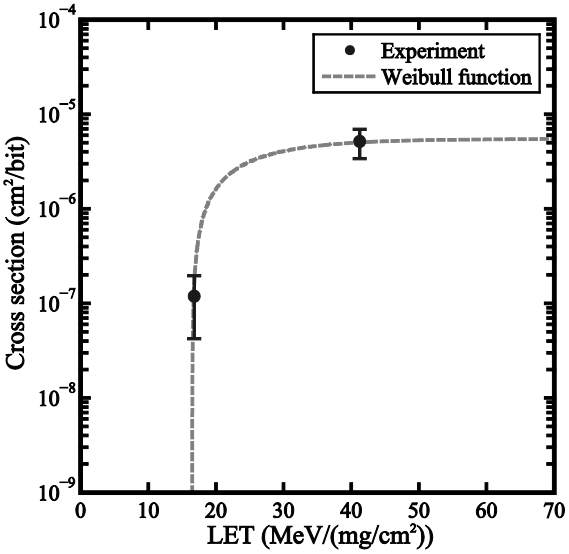

Fig. 1 Relationship between cross-section and LET for irradiation of $^{37}Cl^{8+}$ and $^{81}Br^{12+}$ ions toward AVR.

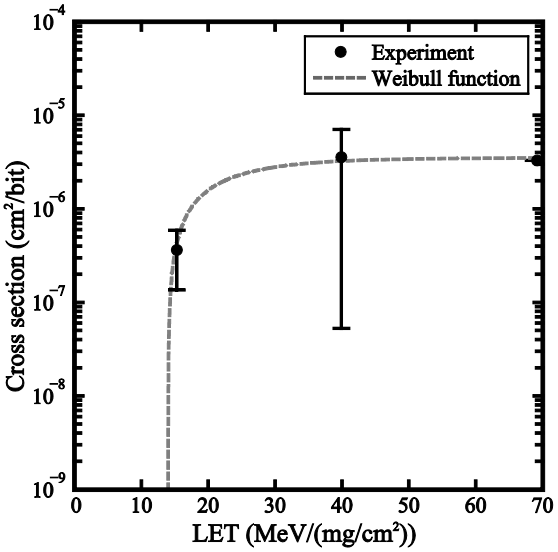

Fig. 2 Relationship between cross-section and LET for irradiation of $^{40}Ar^{8+}$, $^{84}Kr^{17+}$ and $^{129}Xe^{25+}$ ions toward PIC.

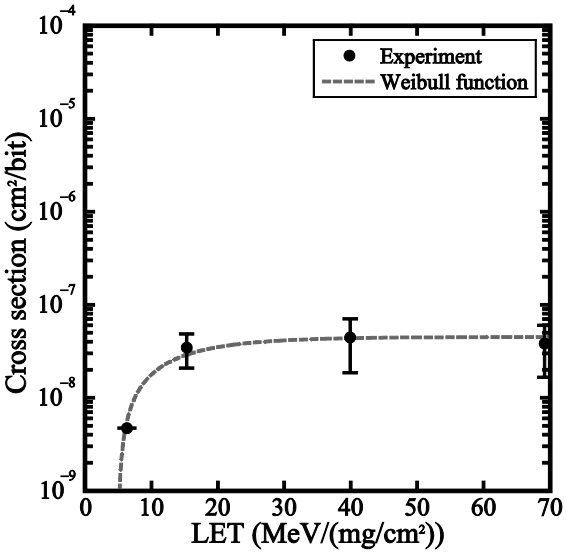

Fig. 3 Relationship between cross-section and LET by irradiating $^{20}Ne^{4+}$, $^{40}Ar^{8+}$, $^{84}Kr^{17+}$ and $^{129}Xe^{25+}$ ions toward MSP.

Table 1 Device properties.

Device	Voltage (V)	Data capacity (byte)
AVR	5	256 (SRAM and flash)
PIC	5	64 (SRAM and EEPROB)
MSP	3.3	256 (FRAM)

References

[1] A. J. Tylka et al., IEEE Trans. Nucl. Sci., 44 (1997) pp.2150-2156.

CHAPTER 8

Publication in Journal and Proceedings, and Contribution to Scientific Meetings

This is a blank page.

8.1 Accelerator Operation and Development

Journal/Proceedings

S. Abe, A. Osa, N. Ishizaki, H. Tayama, M. Matsuda, T. Nakanoya, H. Kabumoto, M. Nakamura, K. Kutsukake, Y. Otokawa, T. Asozu, Y. Tsukihashi, S. Hanashima and T. Ishii
Present status of JAEA-Tokai tandem accelerator facility
Proc. of the 25th Meeting for Tandem Accelerators and their Associated Technologies, Nagoya, Nagoya univ. (July. 20-21, 2012), 36-39.

M. Matsuda, T. Asozu, M. Sataka and A. Iwase
Development of one-accelerator-dual-beam system
Proc. of the 25th Meeting for Tandem Accelerators and their Associated Technologies, Nagoya, Nagoya univ. (July. 20-21, 2012), 94-97.

M. Matsuda, S. Abe, N. Ishizaki, H. Tayama, T. Nakanoya, H. Kabumoto, M. Nakamura, K. Kutsukake, Y. Otokawa, T. Asozu and A. Osa
Present status of JAEA-Tokai tandem accelerator and booster
Proc. of the 9th Annual Meeting of Particle Accelerator Society of Japan, Osaka (Aug. 8-11, 2012) 362-366.

Meetings

S. Abe, A. Osa, N. Ishizaki, H. Tayama, M. Matsuda, T. Nakanoya, H. Kabumoto, M. Nakamura, K. Kutsukake, Y. Otokawa, T. Asozu, Y. Tsukihashi, S. Hanashima and T. Ishii
Present status of JAEA-Tokai tandem accelerator facility
The 25th Meeting for Tandem Accelerators and their Associated Technologies, Nagoya, Nagoya univ. (July. 20-21, 2012).

M. Matsuda, T. Asozu, M. Sataka and A. Iwase
Development of one-accelerator-dual-beam system
The 25th Meeting for Tandem Accelerators and their Associated Technologies, Nagoya, Nagoya univ. (July. 20-21, 2012).

M. Matsuda, S. Abe, N. Ishizaki, H. Tayama, T. Nakanoya, H. Kabumoto, M. Nakamura, K. Kutsukake, Y. Otokawa, T. Asozu and A. Osa
Present status of JAEA-Tokai tandem accelerator and booster
The 9th Annual Meeting of Particle Accelerator Society of Japan, Osaka (Aug. 8-11, 2012).

M. Matsuda, T. Asozu, M. Sataka and A. Iwase

Development of dual-beam system using an electrostatic accelerator for in-situ observation of swift heavy ion irradiation effects on materials

8th International Symposium on Swift Heavy Ions in Matter (SHIM2012), Kyoto, Japan (Oct. 24-27, 2012).

8.2 Nuclear Structure

Journal/Proceedings

M. Asai, K. Tsukada, M. Sakama, H. Haba, T. Ichikawa, Y. Ishii, A. Toyoshima, T. Ishii, I. Nishinaka, Y. Nagame, Y. Kasamatsu, M. Shibata, Y. Kojima and H. Hayashi
Ground-state configuration of the N = 157 nucleus ^{259}No
Phys. Rev., C, 87 (2013) 014332.

Meetings

M. Asai, K. Tsukada, N. Sato, T. K. Sato, A. Toyoshima, S. Miyashita, K. Ooe, Y. Kaneya, T. Ishii and Y. Nagame
Proton configuration in ^{261}Db
2012 Autumn Meeting of the Physical Society of Japan, Kyoto, Japan (Sep. 11-14, 2012).

M. Asai, K. Tsukada, A. Toyoshima, T. K. Sato, Y. Nagame, N. Sato, T. Ishii and Y. Kasamatsu
Measurements of the first excited-state energies in even-even actinide nuclei
56th Symposium on Radiochemisty, Tokyo, Japan (Oct. 3-5, 2012).

M. Asai
Nuclear spectroscopy / nuclear structure in the transition region N = 152 to 162
9th International Workshop “Chemistry of the Superheavy Elements”, Wako, Japan (Mar. 8, 2013).

8.3 Nuclear Reaction

Journal/Proceedings

K. Nishio, S. Mitsuoka, I. Nishinaka, H. Makii, Y. Wakabayashi, H. Ikezoe, K. Hirose, T. Ohtsuki, Y. Aritomo and S. Hofmann
Fusion probabilities in the reactions $^{40,48}Ca + ^{238}U$ at energies around the Coulomb barrier
Phys. Rev. C. 86, 034608-1-6 (2012).

Y. Aritomo, K. Hagino, K. Nishio and S. Chiba
Dynamical approach to heavy-ion induced fission using actinide target nuclei around the Coulomb barrier
Phys. Rev. C. 85, 044614-1-15 (2012).

M. Veselsky, A.N. Andreyev, S. Antalic, M. Huise, P. Möller, K. Nishio, A.J. Sierk, P.Van Duppen, and M. Venhart
Fission-barrier heights of neutron-deficient mercury nuclei
Phys. Rev. C. 86, 024308-1-8 (2012).

J. Khuyagbaatar, K. Nishio, S. Hofmann, D. Ackermann, M. Block, S. Heinz, F. P. Heßberger, K. Hirose, H. Ikezoe, B. Kinlder, B. Lommel, H. Makii, S. Mitsuoka, I. Nishinaka, T. Ohtsuki, Y. Wakabayashi and S. Yan
Evidence for hindrance in fusion between sulfur and lead nuclei
Phys. Rev. C 86, 064602-1-6 (2012).

S. Hofmann, S. Heinz, R. Mann, J. Maurer, J. Khuyagbaatar, D. Ackermann, S. Antalic, W. Barth, M. Block, H.G. Burkhard, V.F. Comas, L. Dahl, K. Eberhardt, J. Gostic, R.A. Henderson, J.A. Heredia, F.P. Hesberger, J.M. Kenneally, B. Kindler, I. Kojouharov, J.V. Kratz, R. Lang, M. Leino, B. Lommel, K.J. Moody, G. Munzenberg, S.L. Nelson, K. Nishio, A.G. Popeko, J. Runke, S. Saro, D.A. Shaughnessy, M.A. Stoyer, P. Thorle-Pospiech, K. Tinschert, N. Trautmann, J. Uusitalo, P.A. Wilk and A.V. Yeremin
The reaction $^{48}Ca + ^{248}Cm \rightarrow ^{296}116^{*}$ studied at the GSI-SHIP
Eur. Phys. J. A, 48, 62-1-23 (2012).

F.P. Hesberger, S. Antalic, D. Ackermann, Z. Kalaninov´a, S. Heinz, S.Hofmann, B. Streicher, B. Kindler, I. Kojouharov, P. Kuusiniemi, M. Leino, B. Lommel, R. Mann, K. Nishio, S. Saro, B. Sulignano and M. Venhar
Alpha-gamma decay studies of ^{253}No and its daughter products ^{253}Md, ^{249}Fm
Eur. Phys. J. A, 48, 75-1-9 (2012).

A. N. Andreyev, S. Antalic, D. Ackermann, L. Bianco, S. Franchoo, S. Heinz, F. P. Heßberger, S. Hofmann, M. Huyse, Z. Kalaninova, I. Kojouharov, B. Kindler, B. Lommel, R. Mann, K. Nishio, R. D. Page, J. J. Ressler, B. Streicher, S. Saro, B. Sulignano and P. Van Duppen
β-delayed fission of ^{192,194}At
Phys. Rev. C 87, 014317-1-8 (2013).

J. F. W. Lane, A. N. Andreyev, S. Antalic, D. Ackermann, J. Gerl, F. P. Heßberger, S. Hofmann, M. Huyse, H. Kettunen, A. Kleinbohl, B. Kindler, I. Kojouharov, M. Leino, B. Lommel, G. Munzenberg, K. Nishio, R. D. Page, S. Saro, H. Schaffner, M. J. Taylor and P. Van Duppen
β-delayed fission of ^{186,188}Bi isotopes
Phys. Rev. C 87, 014318-1-7 (2013).

Y. Aritomo, D.J. Hinde, A. Wakhle, R. du Rietz, W. Dasgupta, K. Hagino, S. Chiba and K. Nishio
Dynamical approach to fusion-fission process in superheavy mass region
EPJ Web of Conferences 35, 05001-1-4 (2012).

Y. Aritomo, K. Hagino, S. Chiba and K. Nishio
Dynamical approach to heavy-ion induced fusion using actinide target
AIP Conf. Proc. 1491, 303 (2012).

S. Ota, H. Makii, T. Ishii, K. Nishio, S. Mitsuoka, I. Nishinaka and S. Chiba
Study on low energy resonances in ^{22}Ne (α, γ) ^{26}Mg using the ^{22}Ne + ^{6}Li α-transfer reaction
Proceedings of Science (12th International Symposium of Nuclei In Cosmos), 221, 2012.

H. Ishiyama, S.C. Jeong, Y. Watanabe, Y. Hirayama, N. Imai, H. Miyatake, M. Oyaizu, I. Katayama, M. Sataka, A. Osa, Y.i Otokawa, M. Matsuda and H. Makii
Toward online nanoscale diffusion measurements using radioactive ^{8}Li tracer
Jpn. J. Appl. Phys. 42, 010205 (2013) 1-3.

H. Makii, H. Miyatake, Y. Wakabayashi, H. Ishiyama, K. Niki, M. Okada, N. Imai, Y.X. Watanabe, Y. Hirayama, S.C. Jeong, T. Shima, I. Nishinaka, S. Mitsuoka, K. Nishio and S. Chiba
Measurement of the ^{12}C(α,γ)^{16}O reaction at TRIAC
AIP Conference Proceedings 1484 (2012) 269-274.

H. Makii, S. Namiki, O. Iwamoto, N. Iwamoto and H. Sawahata,
Radioactive tracer ^{132}Cs (TRACs) for fukushima nuclear plant accident
Journal of the Physical Society of Japan 81, 085003 (2012) 1-2.

Y. Hirayama, M. Mihara, Y.X. Watanabe, S.C. Jeong, H. Miyatake, S. Momota, T. Hashimoto, N. Imai, K. Matsuda, H. Ishiyama, S. Ichikawa, T. Ishii, T. Izumikawa, I. Katayama, H. Kawakami, H. Kawamura, I. Nishinaka, K. Nishio, H. Makii, S. Mitsuoka, A. Osa, Y. Otokawa and T.K. Sato
Tilted-foil technique for producing a spin-polarized radioactive isotope beam
The European Physical Journal A 48, 54 (2012) 1-10.

Meetings

K. Nishio
Fusion-fission study at JAEA for heavy element synthesis
VIII Tours Symposium on Nuclear Physics and Astrophysics, Lenzkirch-Saig, Germany, September 2-7, 2012.

K. Nishio
In-beam fission study at JAEA for heavy-element synthesis
International Conference on Recent Trends in Nuclear Physics 2012, Chandigarh, India, Nov. 19-21, 2012.

K. Nishio
Fusion-fission study at JAEA for heavy-element synthesis
Scientific workshop on Nuclear Fission Dynamics and the Emission of Prompt Neutrons and Gamma Rays (Theory-2), Biarritz, France, Nov. 28-30, 2012.

K. Nishio
Fusion and fission study at JAEA
Seminar at Department of Physics, University of York, York, United Kingdom, Dec. 11, 2012.

K. Nishio
Fission research program at JAEA
10th ASRC International Workshop "Nuclear Fission and Decay of Exotic Nuclei", Tokai, Japan (2013).

K. Nishio
Experimental study for heavy-ion induced fission process
The 5th RIBF Workshop “Fission of Heavy Nuclei” Niigata, Japan, Dec.27. 2012.

S. Ota, H. Makii, T. Ishii, K. Nishio, S. Mitsuoka, I. Nishinaka and S. Chiba
Study on low energy resonances in ^{22}Ne (α, γ) ^{26}Mg using the ^{22}Ne + ^{6}Li α-transfer reaction
12th International Symposium of Nuclei In the Cosmos, Cairns, Australia (Aug. 5-12, 2012).

H. Makii, S. Ota, T. Ishii, K. Nishio, I. Nishinaka, K. Furutaka, Y. Wakabayashi, S. Chiba and M. Igashira
Development of anti-Compton $LaBr_3$(Ce) spectrometer for measurement of surrogate reaction
International Conference on Nuclear Data for Science and Technology (ND 2013), New York, U.S.A. (March 4-8, 2013).

8.4 Nuclear Chemistry

Journal/Proceedings

M. Asai, Y. Kaneya, T. K. Sato, K. Tsukada, K. Ooe, N. Sato and A. Toyoshima
Efficiency calibration of Ge detector for ^{131}I and ^{134}Cs in soil samples and a simplified calculation of cascade summing corrections for volume source
J. Nucl. Radiochem. Sci., 12 (2012) 5.

T. K. Sato, N. Sato, M. Asai, K. Tsukada, A. Toyoshima, K. Ooe, S. Miyashita, M. Schädel, Y. Kaneya, Y. Nagame, A. Osa, S. Ichikawa, T. Stora and J. V. Kratz
First successful ionization of Lr (Z = 103) by a surface-ionization technique
Rev. Sci. Instrum., 84 (2013) 023304.

A. Toyoshima
Chemical studies of rutherfordium (Rf) and nobelium (No) on an atom-at-a-time scale
J. Nucl. Radiochem. Sci. 12 (2012) A1.

X. H. Liang, K. Tsukada, A. Toyoshima, Z. J. Li, M. Asai, T. K. Sato, N. Sato and Y. Nagame
Adsorption behavior of ^{181}W and ^{93m}Mo as lighter homologues of seaborgium (Sg) in HF/HNO_3 on anion-exchange resin
J. Radioanal. Nucl. Chem. 292 (2012) 917.

Meetings

T. Tomitsuka, T. Kojima, M. Murakami, S. Goto, T.K. Sato, K. Tsukada, M. Asai, A. Toyoshima, N. Sato, K. Ooe, Y. Nagame, Y. Kaneya and H. Kudo
Isothermal gas chromatographic behavior of hafnium isotopes
2012 Annual Meeting of the Japan Society of Nuclear and Radiochemical Sciences, Tokyo, Japan (Oct. 3–5).

T. K. Sato, N. Sato, Y. Kaneya, M. Asai, K. Tsukada, A. Toyoshima, K. Ooe, S. Miyashita, A. Osa, S. Ichikawa, M. Schädel, Y. Nagame, T. Stora and J. V. Kratz
Development of surface-ionization type ion-source at the JAEA-ISOL setup for measurement of the first ionization potential of Lr (Z = 103)
16th International Conference on Electromagnetic Isotope Separators and Techniques Related to their Applications (EMIS2012), Matsue, Japan (Dec. 2-7, 2012).

T. K. Sato, N. Sato, M. Asai, K. Tsukada, A. Toyoshima, K. Ooe, S. Miyashita, Y. Nagame, M. Schädel, A. Osa, Y. Kaneya, S. Ichikawa, T. Stora and J. V. Kratz
Ionization potential measurement of lawrencium (Lr, Z = 103) by the surface ionization method
56th Symposium on Radiochemisty, Tokyo, Japan (Oct. 3-5, 2012).

Y. Kaneya, T. K. Sato, N. Sato, M. Asai, K. Tsukada, A. Toyoshima, K. Ooe, S. Miyashita, Y. Nagame, M. Schädel, A. Osa, S. Ichikawa, T. Stora and J. V. Kratz
Development of a gas-jet coupled surface ion source of ISOL for measurement of the first ionization potential of Lr (II)
56th Symposium on Radiochemisty, Tokyo, Japan (Oct. 3-5, 2012).

T. K. Sato, Y. Kaneya, N. Sato, M. Asai, K. Tsukada, A. Toyoshima, K. Ooe, S. Miyashita, Y. Nagame, M. Schädel, S. Ichikawa, T. Stora and J. V. Kratz
Measurement of the first ionization potential of Lr by surface ionization method
2013 Annual Meeting of the Chemical Society of Japan, Kusatsu, Japan (Mar. 22-24, 2013).

Y. Kaneya, T. K. Sato, N. Sato, M. Asai, K. Tsukada, A. Toyoshima, K. Ooe, S. Miyashita, Y. Nagame, M. Schädel, A. Osa, S. Ichikawa, T. Stora and J. V. Kratz
Development of surface ionization method for determination of the first ionization potentials of heavy actinides
2013 Annual Meeting of the Chemical Society of Japan, Kusatsu, Japan (Mar. 22-24, 2013).

I. Nishinaka, A. Yokoyama, K. Washiyama, R. Amano, E. Maeda, N. Yamada, H. Makii, S. Watanabe, N. S. Ishioka and K. Hashimoto
Nuclear and radiochemical study of production and utilization of radioactive astatine isotopes in the $^{7}Li+^{nat}Pb$ reaction
EuCheMS International Conference on Nuclear and Radiochemistry, Como, Italy (Sep. 16-21, 2012).

I. Nishinaka, A. Yokoyama, K. Washiyama, R. Amano, E. Maeda, N. Yamada, T. Taniguchi, S. Watanabe, N. S. Ishioka, K. Hashimoto, H. Makii and A. Toyoshima
Nuclear and radiochemical study of production and utilization of radioactive astatine isotopes in the $^{7}Li+^{nat}Pb$ reaction –Aim at the new cancer medical treatment by α-emitting radioisotopes
Annual Meeting of the Japan Society of Nuclear and Radiochemical Sciences, Tokyo, Japan (Oct. 3-5, 2012).

E. Maeda, A. Yokoyama, N. Yamada, T. Taniguchi, K. Washiyama, R. Amano, I. Nishinaka, N. Takahashi and Y. Kasamatsu
Wet separation with solvent extraction of astatine isotopes in the synthesis process for nuclear medicine
Annual Meeting of the Japan Society of Nuclear and Radiochemical Sciences, Tokyo, Japan (Oct. 3-5, 2012).

K. Washiyama, K. Li, R. Amano, A. Yokoyama, N. Takahashi, K. Nakai, Y. Kasamatsu, A. Shinohara, I. Nishinaka, H. Makii, K. Hashimoto and Y. Kasamatsu
Biodistribution of ^{211}At astatide in mice
Annual Meeting of the Japan Society of Nuclear and Radiochemical Sciences, Tokyo, Japan (Oct. 3-5, 2012).

S. Watanabe, I. Nishinaka, I. Sasaki, K. Yamada, Sa. Watanabe, Y. Sugo, H. Hanaoka, K. Hashimoto and N. S. Ishioka
Synthesis of a biologically active peptide containing radiohalogenated phenylalanine by electrophilic destannylation reaction
7th International Symposium on Radiohalogens (7ISR), Whistler, Canada (Sep. 15-19, 2012).

S. Watanabe, I. Nishinaka, K. Yamada, K. Hashimoto, H. Makii, H. Hanaoka, and N. S. Ishioka
Synthesis of astatinated amino acid derivatives for the radionuclide therapies
56th Symposium on Radiochemistry, Tokyo, Japan (Oct. 3-5, 2012).

A. Toyoshima, S. Miyashita, K. Ooe, M. Asai, T.K. Sato, K. Tsukada, Y. Kitatsuji, Y. Nagame, M. Schädel, J.P. Omtvedt, J. V. Kratz, H. Haba, Y. Kasamatsu, A. Shinohara, A. Wada, K. Akiyama, Y. Oura, A. Yokoyama and K. Sueki
Electrolytic reduction of Mo and W as lighter homologues of seaborgium (Sg)
56th Symposium on Radiochemistry, Tokyo, Japan (Oct. 3 - 5, 2012).

S. Miyashita, A. Toyoshima, K. Ooe, M. Asai, T.K. Sato, K. Tsukada, Y. Kitatsuji, Y. Nagame, M. Schädel, J.P. Omtvedt, J. V. Kratz, H. Haba, Y. Kasamatsu, A. Shinohara, A. Wada, K. Akiyama, Y. Oura, A. Yokoyama and K. Sueki
Solvent extraction of Mo and W for redox studies of Sg
56th Symposium on Radiochemistry, Tokyo, Japan (Oct. 3 - 5, 2012).

K. Ooe, K. Tsukada, M. Asai, T.K. Sato, A. Toyoshima, S. Miyashita, Y. Nagame, M. Schädel, Y. Kaneya, H. Lerum, J.P. Omtvedt, J. V. Kratz, H. Haba, Y. Kasamatsu, A. Shinohara, K. Akiyama, Y. Oura, A. Yokoyama and K. Sueki
Improvement of rapid liquid-liquid extraction apparatus SISAK for redox studies of Sg
56th Symposium on Radiochemistry, Tokyo, Japan (Oct. 3 - 5, 2012).

K. Ooe, K. Tsukada, M. Asai, T.K. Sato, A. Toyoshima, S. Miyashita, Y. Nagame, M. Schädel, Y. Kaneya, H. Lerum, J.P. Omtvedt, J. V. Kratz, H. Haba, A. Wada and Y. Kitayama
Development of a new continuous dissolution apparatus using a hydrophobic membrane filter for superheavy element chemistry
93th Spring Meeting of the Chemical Society of Japan, Kusatsu, Japan (Mar. 27 - 30, 2013).

S. Miyashita, K. Ooe, A. Toyoshima, T.K. Sato, M. Asai, K. Tsukada, Y. Nagame, M. Schädel, Y. Kaneya, J.P. Omtvedt, J. V. Kratz, H. Haba, A. Wada and Y. Kitayama
Extraction behavior of hexavalent Mo and W for Sg experiment
93th Spring Meeting of the Chemical Society of Japan, Kusatsu, Japan (Mar. 27 - 30, 2013).

8.5 Nuclear Theory

Journal/Proceedings

E.S. Diffenderfer, L.T. Baby, D. Santiago-Gonzalez, N. Ahsan, A. Rojas, A. Volya, I. Wiedenhover, A.H. Wuosmaa, M.P. Carpenter, R.V.F. Janssens, C.J. Lister, M. Devlin, D.G. Sarantites, L.G. Sobotka, Y. Utsuno and M. Horoi
High-spin spectrum of ^{24}Mg studied through multiparticle angular correlations
Phys. Rev. C, 85 (2012) 034311-1-17.

N. Shimizu, Y. Utsuno, T. Mizusaki, M. Honma, Y. Tsunoda and T. Otsuka
Variational procedure for nuclear shell-model calculations and energy-variance extrapolation
Phys. Rev. C, 85 (2012) 054301-1-6.

L. Liu, T. Otsuka, N. Shimizu, Y. Utsuno and R. Roth
No-core Monte Carlo shell-model calculation for ^{10}Be and ^{12}Be low-lying spectra
Phys. Rev. C, 86 (2012) 014302-1-9.

T. Abe, P. Maris, T. Otsuka, N. Shimizu, Y. Utsuno and J.P. Vary
Benchmarks of the full configuration interaction, Monte Carlo shell model, and no-core full configuration methods
Phys. Rev. C, 86 (2012) 054301-1-18.

Y. Utsuno, T. Otsuka, B. A. Brown, M. Honma, T. Mizusaki and N. Shimizu
Shape transitions in exotic Si and S isotopes and tensor-force-driven Jahn-Teller effect
Phys. Rev. C, 86 (2012), 051301(R)-1-6.

K. Shimada, H. Ueno, G. Neyens, K. Asahi, D.L. Balabanski, J.M. Daugas, M. Depuydt, M.De Rydt, L. Gaudefroy, S. Grevy, Y. Hasama, Y. Ichikawa, D. Kameda, P. Morel, T. Nagatomo, L. Perrot, Ch. Stodel, J.-C. Thomas, Y. Utsuno, W. Vanderheijden, N. Vermeulen, P. Vingerhoets, E. Yagi, K. Yoshida and A. Yoshimi
Erosion of N=20 shell in ^{33}Al investigated through the ground-state electric quadrupole moment
Phys. Lett. B, 714 (2012) 246-250.

N. Shimizu, T. Abe, Y. Tsunoda, Y. Utsuno, T. Yoshida, T. Mizusaki, M. Honma and T. Otsuka
New-generation Monte Carlo shell model for the K supercomputer era
Prog. Theor. Exp. Phys., 2012 (2012) 01A205-1-27.

Y. Utsuno, T. Otsuka, B.A. Brown, M. Honma, T. Mizusaki and N. Shimizu
Shell evolution around and beyond N=28 studied with large-scale shell-model calculations
Prog. Theor. Phys. Suppl., 196 (2012) 304-309.

Y. Utsuno, N. Shimizu, T. Otsuka and T. Abe
Efficient computation of Hamiltonian matrix elements between non-orthogonal Slater determinants
Comput. Phys. Commun., 184 (2013) 102-108.

H. Koura and S. Chiba
Single-particle levels of spherical nuclei in the superheavy and extremely superheavy mass region
J. Phys. Soc. Jpn. 82, (2013) 014201-1-5.

H. Koura
Phenomenological formula for alpha-decay half-lives
J. Nucl. Sci. Technol. 49, (2012) 816-823.

K. Morita, K. Morimoto, D. Kaji, H. Haba, K. Ozeki, Y. Kudou, T. Sumita, Y. Wakabayashi, A. Yoneda, K. Tanaka, S. Yamaki, R. Sakai, T. Akiyama, S. Goto, H. Hasebe, M. Huang, T. Huang, E. Ideguchi, Y. Kasamatsu, K. Katori, Y. Kariya, H. Kunieda, H. Koura, H. Kudo, A. Mashiko, K. Mayama, S. Mitsuoka, T. Moriya, M. Murakami, H. Murayama, S. Nanami, A. Ozawa, N. Sato, K. Sueki, M. Takeyama, F. Tokanai, T. Yamaguchi and A. Yoneda
New result in the production and decay of an isotopes, ^{278}113, of the 113th element
J. Phys. Soc. Jpn. 81, (2012) 103201-1-4.

M. S. Smith, C.D. Nesaraja, E.J. Lingerfelt, H. Koura and F.G. Kondev
Comparison of Nuclear Mass Models at nuclearmasses.org
Origin of matter and evolution of galaxies 2011, eds. S. Kubono *et al*. (AIP Conf. Proc. 1484, 2012), pp.421-423.

Meetings

Y. Utsuno
Monte Carlo shell model and its applications to exotic nuclei
International Workshop “Nuclear Theory in the Supercomputing Era,” Khabarovsk, Russia (Jun. 18-22, 2012).

Y. Utsuno
Tensor-force driven shell evolution in correlated nuclei
International Symposium on Perspective in Isospin Physics—Role of non-central interactions in structure and dynamics of unstable nuclei—, Wako, Japan (Aug. 27-28, 2012).

Y. Utsuno
Recent shell model results for exotic nuclei
VIII Tours Symposium on Nuclear Physics and Astrophysics, Lenzkirch-Saig, Germany (Sep. 2-7, 2012).

Y. Utsuno, N. Shimizu, M. Honma, T. Mizusaki and T. Otsuka
Shell evolution in antimony isotopes
2012 Fall Meeting of the Physical Society of Japan, Kyoto, Japan (Sep. 11-14, 2012).

Y. Utsuno
Shell evolution probed by energy levels in unstable nuclei
The 3rd RIBF Discussion Meeting “γ-ray Spectroscopy of Medium-Heavy Unstable Nuclei,” Sendai, Japan (Sep. 24, 2012).

Y. Utsuno
Towards unified description of the shell evolution
International Symposium "Exotic Nuclear Structure From Nucleons," Tokyo, Japan (Oct. 10-12, 2012).

Y. Utsuno
Shell evolution in neutron-rich calcium isotopes
7th Italy-Japan Symposium on Nuclear Physics, Milan, Italy (Nov. 20-23, 2012).

Y. Utsuno
Manifestation of the shell evolution in energy levels of exotic nuclei
RCNP International Workshop on Physics Opportunities Using Compton Suppressed Ge Clover Array (Clover12), Osaka, Japan (Dec. 7-8, 2012).

Y. Utsuno
Shell evolution along the Sn isotopes
10th ASRC International Workshop "Nuclear Fission and Decay of Exotic Nuclei", Tokai, Japan (Mar. 21-22, 2013).

Y. Utsuno, T. Otsuka, N. Shimizu, T. Mizusaki and M. Honma
Energy levels and shell evolution in neutron-rich calcium isotopes
68th Annual Meeting of the Physical Society of Japan, Higashi-Hiroshima, Japan (Mar. 27-29, 2013).

H. Koura and S. Chiba
Theoretical study of decay heat and delayed neutron accompanied with beta-decay from fission fragments
Spring Meeting of the Atomic Energy Society of Japan, Osaka, Japan (Mar. 26-28, 2013).

H. Koura
Theoretical study of beta-delayed neutron and decay heat
10th ASRC International Workshop, “Nuclear Fission and Decay of Exotic Nuclei”, JAEA Tokai, Japan (Mar. 21-22, 2013).

H. Koura

Properties of nuclear masses for heavy and superheavy nuclei

Workshop on Low-Energy Radioactive Isotope Beam (RIB) Production by In-Gas Laser Ionization for Decay Spectroscopy at RIKEN, Wako, Japan (Dec. 10-11, 2012).

H. Koura

Effect of decay modes of superheavy nuclei to r-process nucleosynthesis

ENSAR-ECOS Workshop on Future Superheavy Element Strategy (FUSHE 2012), Erbismühle, Germany (May. 13-16, 2012).

8.6 Atomic Physics and Solid-state Physics

Journal/Proceedings

M. Imai
Semiempirical formulae for inelastic atomic and molecular collisions
Atomic Processes in Basic and Applied Physics, Springer Series on Atomic, Optical and Plasma Physics 68, eds. V. Shevelko and H. Tawara, Springer-Verlag Berlin Heidelberg (2012) 455–479.

H. Ishiyama, S.C. Jeong, Y.X. Watanabe, Y. Hirayama, N. Imai, H. Miyatake, M. Oyaizu, I. Katayama, M. Sataka,, A. Osa, Y. Otokawa, M. Matsuda and H. Makii
Toward online nanoscale diffusion measurements using radioactive ^{8}Li tracer
Jpn. J. Appl. Phys. 52 (2013) 010205.

Meetings

M. Imai, M. Sataka, K. Kawatsura, K. Takahiro, K. Komaki, H. Shibata and K. Nishio
Charge state evolution for 2 MeV/u carbon ions passing through carbon foils
23rd International Conference on Atomic Collisions in Solids (ICACS 25), Kyoto, Japan (Oct. 21-25, 2012).

Y. Ohta, T. Majima, M. Imai, H. Tsuchida, H. Shibata, A. Itoh and M. Sataka
Charge state distribution of 1 MeV/u tungsten ions after penetration of carbon foils
8th International Symposium on Swift Heavy Ions in Matter (SHIM2012), Kyoto, Japan (Oct. 24-27, 2012).

N. Matsunami, Y. Sakuma, M. Sataka, S. Okayasu and H. Kakiuchida
Electronic sputtering of CuO films by high-energy ions
8th International Symposium on Swift Heavy Ions in Matter (SHIM2012), Kyoto, Japan (Oct. 24-27, 2012).

H. Ishiyama, S.C. Jeong, Y.X. Watanabe, Y. Hirayama, N. Imai, H. Miyatake, M. Oyaizu, I. Katayama, M. Sataka,, A. Osa, Y. Otokawa, M. Matsuda and H. Makii
In-situ diffusion measurements in solids using short lived radioactive tracers of ^{8}Li and ^{20}Na
XVI International Conference on Electromagnetic Isotope Separators and Techniques Related to their Application (EMIS 2012), Matsue, Japan (Dec. 2-7, 2012).

S.C. Jeong, H. Ishiyama, N. Imai, Y. Hirayama, H. Miyatake, Y.X. Watanabe, I. Katayama, H. Kawakami, M. Sataka, S. Okayasu, S. Ichikawa, K. Nishio, S. Mitsuoka, T. Nakanoya, M. Yahagi and T. Hashimoto
Online diffusion experiments in solids by implanting radiotracer beam of ^{8}Li
8th International Symposium on Swift Heavy Ions in Matter (SHIM 2012), Kyoto, Japan (Oct. 24-27, 2012).

8.7 Radiation Effects in Materials

Journal/Proceedings

K. Shimizu, S. Kosugi, Y. Tahara, K. Yasunaga, Y. Kaneta, N. Ishikawa, F. Hori, T. Matsui and A. Iwase
Change in magnetic properties induced by swift heavy ion irradiation in CeO_2
Nucl. Instrum. Methods Phys. Res., B286 (2012) 291-294.

Y. Tahara, K. Shimizu, N. Ishikawa, Y. Okamoto, F. Hori, T. Matsui and A. Iwase
Study on effects of energetic ion irradiation in Gd_2O_3-doped CeO_2 by means of synchrotron radiation X-ray spectroscopy
Nucl. Instrum. Methods Phy. Res., B277 (2012) 53-57.

Y.Sasaki and T.Suzuki,
Formation of Ag clusters by electron beam irradiation on Ag-Zeolite
Materials Transactions, 50 (2009)1050.

Y.Sasaki and S.Okayasu
Zeolite and the manufacturing method
Patent application 2009-213741 (Sep. 2009).

T. Sueyoshi, Y. Furuki, E. Tanaka, T. Fujiyoshi, F. Mitsugi, T. Ikegami and N. Ishikawa
Angular dependence of critical current density in YBCO films with columnar defects crossing at widespread angles
IEEE Trans. Appl. Supercond. 23 (2013) 8002404.

T. Sueyoshi, T. Nishimura, T. Fujiyoshi, F. Mitsugi, T. Ikegami and N. Ishikawa
Angular dependences of critical current density and n-value in YBCO thin films at high density of columnar defects
The proceedings of the 24th International Cryogenic Engineering Conference and the International Cryogenic Materials Conference 2012, 829-832.

Meetings

K.Yasuda, M. Etoh, K. Sawada, T. Yamamoto, K. Yasunaga, S. Matsumura and N. Ishikawa
Defect formation and accumulation in CeO_2 irradiated with swift heavy ions
8th International Symposium on Swift Heavy Ions in Matter (SHIM2012), Kyoto, Japan (Oct. 24-27, 2012).

T. Yamamoto, K.Yasuda, S. Matsumuraa and N. Ishikawa
TEM analysis of ion tracks in $MgAl_2O_4$
8th International Symposium on Swift Heavy Ions in Matter (SHIM2012), Kyoto, Japan (Oct. 24-27, 2012).

K.Yasuda, M. Etoh, K. Yasunaga, T. Yamamoto, S. Matsumura and N. Ishikawa
S*ynergistic ittadiation effects of electronic/lattice excitation in CeO_2 irradiated with swift heavy ions*
152th Spring Meeting of Japan Institute of Metals, March 27-29, Tokyo.

S. Matsumura, T. Yamamoto, K. Yasuda and S. Takaki (Invited Talk)
Transmission electron microscopy study of defect formation and accumulation in ceramic oxides irradiated with swift heavy ions
MRS Fall Meeting 2012, Nov.27-Dec.1, 2012, Boston.

K. Shimizu, T. Kishino Y. Tahara, K. Yasunaga, N. Ishikawa, Y. Okamoto, Y. Baba, N. Hirao, Y. Saitoh, F. Hori, T. Matsui and A. Iwase
Effects of swift heavy ion irradiation and high temperature annealing on the structure and magnetic propeties of CeO_2
8th International Symposium on Swift Heavy Ions in Matter (SHIM2012), Kyoto, Japan (Oct. 24-27, 2012).

M. Hayashi, M. Matsuda, T. Asozu, M. Sataka, M. Nakamura and A. Iwase
In-situ RBS measurements for the effect of swift heavy ion irradiation on metal-insulator interfaces
8th International Symposium on Swift Heavy Ions in Matter (SHIM2012), Kyoto, Japan (Oct. 24-27, 2012).

Y. Sasajima, T. Osada, N. Ishikawa and A. Iwase
Computer simulation of high-energy-ion irradiation of uranium dioxide
8th International Symposium on Swift Heavy Ions in Matter (SHIM2012), Kyoto, Japan (Oct. 24-27, 2012).

Y. Sasajima, N. Ajima, T. Osada, N. Ishikawa and A. Iwase
Computer simulation of high-energy-beam of ceria
8th International Symposium on Swift Heavy Ions in Matter (SHIM2012), Kyoto, Japan (Oct. 24-27, 2012).

K. Nakano, T. Kojima and A. Iwase
Radiation effects in yttria-stabilized zirconia
8th International Symposium on Swift Heavy Ions in Matter (SHIM2012), Kyoto, Japan (Oct. 24-27, 2012).

N. Ishikawa
Damages in UO_2 and CeO_2 irradiated with high-energy heavy ions
SHIMEC2012 (International Conference on Swift Heavy Ions in Materials Engineering and Characterization), New Delhi. India (Oct. 9-12, 2012).

N. Ishikawa, Y. Chimi, O. Michikami and A. Iwase
Electrical resistivity change due to high-energy X-ray irradiation of oxide ceramics
ICACS-25 (25th International Conference on Atomic Collisions in Solids). Kyoto, Japan(Oct. 21-25, 2012).

N. Ishikawa, T. Sonoda, T. Sawabe, H. Sugai and M. Sataka
Electronic stopping power dependence of ion-track size in UO_2 irradiated with heavy ions in the energy range of ~1MeV/u
8th International Symposium on Swift Heavy Ions in Matter (SHIM2012), Kyoto, Japan (Oct. 24-27, 2012).

N. Okubo, N. Ishikawa, M. Sataka and S. Jitsukawa
Surface amorphization in Al_2O_3 induced by swift heavy ion irradiation
8th International Symposium on Swift Heavy Ions in Matter (SHIM2012), Kyoto, Japan (Oct. 24-27, 2012).

Y.Sasaki, M. Kobayashi, H. Kita and S. Okayasu
Formation of metal microstructures induced by heavy ion irradiation in Ag-zeolite
AMTC2 (The 2nd International Symposium on Advanced Microscopy and Theoretical Calculations).

M. Fujimaki, M. Sataka and M. Matsuda
Formation of an ion beam for mass-productive nanofabrication technology
The 25th Meeting for Tandem Accelerators and their Associated Technologies, Nagoya, Nagoya univ. (July. 20-21, 2012).

T. Sueyoshi, T. Nishimura, T. Fujiyoshi, F. Mitsugi, T. Ikegami and N. Ishikawa
Angular dependences of critical current density and n-value in YBCO thin films at high density of columnar defects
24th International Cryogenic Engineering Conference and the International Cryogenic Materials Conference 2012 (ICEC24/ICMC2012), Fukuoka, Japan (May 14-18, 2012).

T. Sueyoshi, Y. Furuki, E. Tanaka, T. Fujiyoshi, F. Mitsugi, T. Ikegami and N. Ishikawa
Angular dependence of critical current density in YBCO films with columnar defects crossing at widespread angles
American Superconductivity Conference 2012 (ASC2012), Oregon, USA (Oct. 7-12, 2012).

T. Sueyoshi, T. Fujiyoshi, F. Mitsugi, T. Ikegami and N. Ishikawa
Influence of anisotropically splayed columnar defects on angular dependece of critical current density in YBCO thin films
8th International Symposium on Swift Heavy Ions in Matter (SHIM2012), Kyoto, Japan (Oct. 24-27, 2012).

T. Sueyoshi, T. Koutaki, T. Fujiyoshi, F. Mitsugi, T. Ikegami and N. Ishikawa
Angular dependence of critical current density in $BaZrO_3$ / $YBa_2Cu_3O_y$ quasi-multilayered films with columnar defects
25th International symposium on superconductivity (ISS2012), Tokyo, Japan (Dec. 3-5, 2012).

H. Amekura, N. Okubo, N. Ishikawa, S.A. Khan, U.B. Singh, D.K. Avasthi, K. Mitsuishi and Y. Nakayama
Critical evaluation of the synergy model for elongation of embedded nanoparticles by swift heavy ion irradiation
18th International Conference on Ion Beam Modification of Materials (IBMM 2012), Qingdao, China (Sep. 2-7, 2012).

H. Amekura, N. Okubo, N. Ishikawa, S.A. Khan, U.B. Singh, D.K. Avasthi, K. Mitsuishi and Y. Nakayama
Critical evaluation of the synergy model for elongation of embedded nanoparticles by swift heavy ion irradiation
International Union of Materials Research Societies, International Conference on electronic Materials 2012 (IUMRS-ICEM 2012), Yokohama, Japan (Sep. 23-28, 2012).

H. Amekura, N. Okubo, N. Ishikawa, D. Tsuya, Y. Nakayama and K. Mitsuishi
Embedded ZnO nanoparticles irradiated with swift heavy ions: Irradiation-induced formation of metal phase and elongation
25th International Conference on Atomic Collisions in Solids (ICACS 2012), Kyoto, Japan (Oct. 21-25, 2012).

H. Amekura, N. Okubo, N. Ishikawa, S.A. Khan, U.B. Singh, D.K. Avasthi, K. Mitsuishi and Y. Nakayama
Critical evaluation of the synergy model for elongation of embedded nanoparticles by swift heavy ion irradiation
8th International Symposium on Swift Heavy Ions in Matter (SHIM 2012), Kyoto, Japan (Oct. 24-27, 2012).

This is a blank page.

CHAPTER 9

Personnel and Committee

This is a blank page.

9.1 Personnel

Department of Research Reactor and Tandem Accelerator

Takeshi	Maruo	Director
Tetsuo	Ishii	Deputy Director
Yoji	Murayama	Deputy Director
Shuji	Yoshinari	Manager of Administration Section
Masao	Sataka	(Temporary Staff)

Department of Research Reactor and Tandem Accelerator

Tandem Accelerator Section (*General Manager)

Scientific Staff

Akihiko	Osa*
Makoto	Matsuda

Technical Staff

Shin-ichi	Abe	
Nobuhiro	Ishizaki	
Hidekazu	Tayama	
Takamitsu	Nakanoya	
Hiroshi	Kabumoto	
Masahiko	Nakamura	
Ken-ichi	Kutsukake	
Yoshinori	Otokawa	
Takuhiro	Asozu	
Susumu	Hanashima	(Temporary Staff)
Yoshihiro	Tsukihashi	(Temporary Staff)

Department of Radiation Protection

Facility Radiation Control Section I

Katsunori	Sawahata	
Teruhiko	Takahashi	
Yumi	Ueno	
Susumu	Kinase	
Yuriko	Kaneko	

Advanced Science Research Center

Sadamichi	Maekawa	Director
Yuichiro	Nagame	Deputy Director
Tomotsugu	Sawai	General Manager of Research Coordination and Promotion Office
Hiroshi	Ikezoe	(Temporary Staff)

Advanced Science Research Center

Research Group for Reactions involving Heavy Nuclei *(* Group Leader)*

Andrei	Andreyev*	
Katsuhisa	Nishio	
Ichiro	Nishinaka	
Hiroyuki	Koura	
Yutaka	Utsuno	
Hiroyuki	Makii	
Kentaro	Hirose	
Syuya	Ota	(Post Doc., JSPS)
Tatsuro	Nagayama	(Student)
Eita	Maeda	(Student)

Advanced Science Research Center

Research Group for Superheavy Elements *(* Group Leader)*

Matthias	Schädel*	
Kazuaki	Tsukada	
Masato	Asai	
Tetsuya K.	Sato	
Atsushi	Toyoshima	
Kazuhiro	Ooe	(Post Doc.)
Sunao	Miyashita	(Post Doc.)
Yusuke	Kaneya	(Student)

Advanced Science Research Center

Research Group for Mechanical Control of Materials and Spin Systems

Satoru	Okayasu	(Deputy Group Leader)

Nuclear Science and Engineering Directorate

Innovative Nuclear Science Research Group *(* Group Leader)*

Hideo	Harada*	
Hideki	Iimura	
Mitsuo	Koizumi	
Kazuyoshi	Furutaka	
Fumito	Kitatani	
Shoji	Nakamura	
Yosuke	Toh	
Atsushi	Kimura	
Kaoru	Hara	(Senior Post Doc.)
Masumi	Oshima	(Temporary Staff)

Nuclear Science and Engineering Directorate

Research Group for Radiation Materials Engineering

Norito	Ishikawa
Nariaki	Okubo

Quantum Beam Science Directorate

Neutron Imaging and Activation Analysis Group

Yuichi	Hatsukawa

9.2 Research Planning and Assessment Committee

Chairman	Kouichiro	Asahi	(Professor, Tokyo Institute of Technology)
Member	Tadashi	Kambara	(Senior Scientist, RIKEN)
	Kenji	Kimura	(Professor, Kyoto University)
	Shigeo	Tomita	(Associate Professor, University of Tsukuba)
	Toshiaki	Kaneko	(Professor, Okayama University of Science)
	Hisaaki	Kudo	(Professor, Niigata University)
	Eiji	Ideguchi	(Associate Professor, Osaka University)
	Hitoshi	Nakada	(Professor, Chiba University)
	Koichi	Hagino	(Associate Professor, Tohoku University)
	Tomotsugu	Sawai	(Advanced Science Research Center, JAEA)
	Hideo	Harada	(Nuclear Science and Engineering Directorate, JAEA)
	Yuichi	Hatsukawa	(Quantum Beam Science Directorate, JAEA)
	Tetsuro	Ishii	(Dep. Research Reactor and Tandem Accelerator, JAEA)
	Masao	Sataka	(Dep. Research Reactor and Tandem Accelerator, JAEA)
	Kiichi	Hojo	(Advanced Science Research Center, JAEA)
Organizer Secretary			
	Shin-ichi	Mitsuoka	(Advanced Science Research Center, JAEA)
	Norito	Ishikawa	(Nuclear Science and Engineering Directorate, JAEA)
	Masato	Asai	(Advanced Science Research Center, JAEA)
	Hiroshi	Ikezoe	(Advanced Science Research Center, JAEA)

CHAPTER 10

New Research Programs

10.1 New Research Programs Approved in the FY2012

This is a blank page.

10.1 New Research Programs Approved in the FY2012

Title	Spokesperson & Affiliation
1. Shape and property control of nanoparticles by swift heavy ions *	Hiroshi Amekura National Institute for Materials Science (NIMS)
2. Application of high-aspect-ratio nanoholes formed by etching of latent tracks for sensors *	Makoto Fujimaki National Institute of Advanced Industrial Science and Technology (AIST)
3. Irradiation influence evaluation of FRAM based microprocessor and consumer radio equipment for space application *	Toshihiro Kameda University of Tsukuba
4. 0-degree electron spectroscopy with fast cluster ions *	Shigeo Tomita University of Tsukuba
5. Study of microstructure formation in ion-irradiated uranium oxide in high-fluence region	Norito Ishikawa JAEA
6. Control of electronic and magnetic properties of heavy element oxides by using high density electronic excitation due to swift heavy ions	Akihiro Iwase Osaka Prefecture University
7. Electronic excitation effects and material modifications of ceramics by high-energy ions	Noriaki Matsunami Nagoya University
8. Charge state evolution of swift heavy ions passing through foil targets and charge exchange of ions passing through gas targets	Makoto Imai Kyoto University
9. Formation of nano-structure by high-energy heavy ions	Satoru Okayasu JAEA
10. Change in electrical conductivity and microstructure in ceramic materials by high-energy ion irradiation	Nariaki Okubo JAEA
11. Fission of proton-rich nucleus in the mercury region (2)	A. N. Andreyev University of the West of Scotland
12. Effect of projectile nucleus on heavy-ion fusion reaction for new element synthesis	Katsuhisa Nishio JAEA
13. Synthesis of a new isotope ^{216}U near $N = 126$ closed shell	Yasuo Wakabayashi JAEA
14. Development of an on-line gas cell for laser spectroscopy of the unstable nuclides in tungsten region	Hideki Iimura JAEA

15. Enhancement of critical current density by hybrid effect of flux pinning in heavy-ion irradiated high-T_c superconducting thin films *	Tetsuro Sueyoshi Kumamoto University
16. Application of high-aspect-ratio nanoholes formed by etching of latent tracks for sensors *	Makoto Fujimaki National Institute of Advanced Industrial Science and Technology (AIST)
17. Atomistic structure of ion tracks in ceramic compounds irradiated with swift heavy ions *	Kazuhiro Yasuda Kyushu University
18. Direct observation of ion tracks in amorphous thin films using TEM *	Kenji Kimura Kyoto University
19. Search for highly deformed states in A=30~40 nuclei *	Eiji Ideguchi Osaka University
20. Development for measurement of diffusion coefficients in Li ion battery material using ^{8}Li radioactive tracer *	Hironobu Ishiyama High Energy Accelerator Research Organization (KEK)
21. Synthesis of 211At labeled compound and evaluation of DNA damage in cancer cell for targeted radionuclide therapy	Shigeki Watanabe JAEA
22. Production of medical radioisotopes ^{95m}Tc	Yuichi Hatsukawa JAEA
23. Reduction and extraction behavior of Mo and W and development of a new chemistry apparatus for the redox potential measurement of seaborgium	Atsushi Toyoshima JAEA
24. Observation of fission mode with large mass asymmetry in iridium isotopes	Katsuhisa Nishio JAEA
25. Measurement of neutron capture cross sections using a surrogate reaction	Hiroyuki Makii JAEA
26. Measurement of branching ratio of ^{22}Ne(α,γ)^{26}Mg / ^{22}Ne(α,n)^{25}Mg reactions (2)	Shuya Ota JAEA
27. Measurement of ionization potential of Lr by surface ionization method (II)	Tetsuya K. Sato JAEA
28. *Projects not intended for public disclosure, [2012ADC1]* *	
29. Development of the accelerator system and the inventive ion beam application	Makoto Matsuda JAEA

30. Study of delayed-neutron yields for accurate evaluation of kinetics of high-burnup reactors **	Katsuhisa Nishio JAEA

* Approved as a Common Use Program of JAEA.

** Approved as a JST Innovative Nuclear Research and Development Program entrusted to JAEA.

This is a blank page.

国際単位系（SI）

表１．SI 基本単位

基本量	SI 基本単位	
	名称	記号
長さ	メートル	m
質量	キログラム	kg
時間	秒	s
電流	アンペア	A
熱力学温度	ケルビン	K
物質量	モル	mol
光度	カンデラ	cd

表２．基本単位を用いて表されるSI組立単位の例

組立量	SI 基本単位	
	名称	記号
面積	平方メートル	m^2
体積	立法メートル	m^3
速さ，速度	メートル毎秒	m/s
加速度	メートル毎秒毎秒	m/s^2
波数	毎メートル	m^{-1}
密度，質量密度	キログラム毎立方メートル	kg/m^3
面積密度	キログラム毎平方メートル	kg/m^2
比体積	立方メートル毎キログラム	m^3/kg
電流密度	アンペア毎平方メートル	A/m^2
磁界の強さ	アンペア毎メートル	A/m
量濃度(a)，濃度	モル毎立方メートル	mol/m^3
質量濃度	キログラム毎立法メートル	kg/m^3
輝度	カンデラ毎平方メートル	cd/m^2
屈折率(b)	（数字の） 1	1
比透磁率(b)	（数字の） 1	1

(a) 量濃度（amount concentration）は臨床化学の分野では物質濃度（substance concentration）ともよばれる。
(b) これらは無次元量あるいは次元１をもつ量であるが、そのことを表す単位記号である数字の１は通常は表記しない。

表３．固有の名称と記号で表されるSI組立単位

組立量	SI 組立単位			
	名称	記号	他のSI単位による表し方	SI基本単位による表し方
平面角	ラジアン(b)	rad	1 (b)	m/m
立体角	ステラジアン(b)	sr(c)	1 (b)	m^2/m^2
周波数	ヘルツ(d)	Hz		s^{-1}
力	ニュートン	N		m kg s^{-2}
圧力，応力	パスカル	Pa	N/m^2	m^{-1} kg s^{-2}
エネルギー，仕事，熱量	ジュール	J	N m	m^2 kg s^{-2}
仕事率，工率，放射束	ワット	W	J/s	m^2 kg s^{-3}
電荷，電気量	クーロン	C		s A
電位差（電圧），起電力	ボルト	V	W/A	m^2 kg s^{-3} A^{-1}
静電容量	ファラド	F	C/V	m^{-2} kg^{-1} s^4 A^2
電気抵抗	オーム	Ω	V/A	m^2 kg s^{-3} A^{-2}
コンダクタンス	ジーメンス	S	A/V	m^{-2} kg^{-1} s^3 A^2
磁束	ウエーバ	Wb	Vs	m^2 kg s^{-2} A^{-1}
磁束密度	テスラ	T	Wb/m^2	kg s^{-2} A^{-1}
インダクタンス	ヘンリー	H	Wb/A	m^2 kg s^{-2} A^{-2}
セルシウス温度	セルシウス度(e)	℃		K
光束	ルーメン	lm	cd sr(c)	cd
照度	ルクス	lx	lm/m^2	m^{-2} cd
放射性核種の放射能(f)	ベクレル(d)	Bq		s^{-1}
吸収線量, 比エネルギー分与, カーマ	グレイ	Gy	J/kg	m^2 s^{-2}
線量当量, 周辺線量当量, 方向性線量当量, 個人線量当量	シーベルト(g)	Sv	J/kg	m^2 s^{-2}
酸素活性	カタール	kat		s^{-1} mol

(a)SI接頭語は固有の名称と記号を持つ組立単位と組み合わせても使用できる。しかし接頭語を付した単位はもはやコヒーレントではない。
(b)ラジアンとステラジアンは数字の１に対する単位の特別な名称で、量についての情報をつたえるために使われる。実際には、使用する時には記号radおよびsrが用いられるが、習慣として組立単位としての記号である数字の１は明示されない。
(c)測光学ではステラジアンという名称と記号srを単位の表し方の中に、そのまま維持している。
(d)ヘルツは周期現象についてのみ、ベクレルは放射性核種の統計的過程についてのみ使用される。
(e)セルシウス度はケルビンの特別な名称で、セルシウス温度を表すために使用される。セルシウス度とケルビンの単位の大きさは同一である。したがって、温度差や温度間隔を表す数値はどちらの単位で表しても同じである。
(f)放射性核種の放射能（activity referred to a radionuclide）は、しばしば誤った用語で"radioactivity"と記される。
(g)単位シーベルト（PV,2002,70,205）についてはCIPM勧告2（CI-2002）を参照。

表４．単位の中に固有の名称と記号を含むSI組立単位の例

組立量	SI 組立単位		
	名称	記号	SI 基本単位による表し方
粘度	パスカル秒	Pa s	m^{-1} kg s^{-1}
力のモーメント	ニュートンメートル	N m	m^2 kg s^{-2}
表面張力	ニュートン毎メートル	N/m	kg s^{-2}
角速度	ラジアン毎秒	rad/s	m m^{-1} s^{-1}=s^{-1}
角加速度	ラジアン毎秒毎秒	rad/s^2	m m^{-1} s^{-2}=s^{-2}
熱流密度，放射照度	ワット毎平方メートル	W/m^2	kg s^{-3}
熱容量，エントロピー	ジュール毎ケルビン	J/K	m^2 kg s^{-2} K^{-1}
比熱容量，比エントロピー	ジュール毎キログラム毎ケルビン	J/(kg K)	m^2 s^{-2} K^{-1}
比エネルギー	ジュール毎キログラム	J/kg	m^2 s^{-2}
熱伝導率	ワット毎メートル毎ケルビン	W/(m K)	m kg s^{-3} K^{-1}
体積エネルギー	ジュール毎立方メートル	J/m^3	m^{-1} kg s^{-2}
電界の強さ	ボルト毎メートル	V/m	m kg s^{-3} A^{-1}
電荷密度	クーロン毎立方メートル	C/m^3	m^{-3} sA
表面電荷	クーロン毎平方メートル	C/m^2	m^{-2} sA
電束密度，電気変位	クーロン毎平方メートル	C/m^2	m^{-2} sA
誘電率	ファラド毎メートル	F/m	m^{-3} kg^{-1} s^4 A^2
透磁率	ヘンリー毎メートル	H/m	m kg s^{-2} A^{-2}
モルエネルギー	ジュール毎モル	J/mol	m^2 kg s^{-2} mol^{-1}
モルエントロピー, モル熱容量	ジュール毎モル毎ケルビン	J/(mol K)	m^2 kg s^{-2} K^{-1} mol^{-1}
照射線量（X線及びγ線）	クーロン毎キログラム	C/kg	kg^{-1} sA
吸収線量率	グレイ毎秒	Gy/s	m^2 s^{-3}
放射強度	ワット毎ステラジアン	W/sr	m^4 m^{-2} kg s^{-3}=m^2 kg s^{-3}
放射輝度	ワット毎平方メートル毎ステラジアン	$W/(m^2$ sr)	m^2 m^{-2} kg s^{-3}=kg s^{-3}
酵素活性濃度	カタール毎立方メートル	kat/m^3	m^{-3} s^{-1} mol

表５．SI 接頭語

乗数	接頭語	記号	乗数	接頭語	記号
10^{24}	ヨタ	Y	10^{-1}	デシ	d
10^{21}	ゼタ	Z	10^{-2}	センチ	c
10^{18}	エクサ	E	10^{-3}	ミリ	m
10^{15}	ペタ	P	10^{-6}	マイクロ	μ
10^{12}	テラ	T	10^{-9}	ナノ	n
10^9	ギガ	G	10^{-12}	ピコ	p
10^6	メガ	M	10^{-15}	フェムト	f
10^3	キロ	k	10^{-18}	アト	a
10^2	ヘクト	h	10^{-21}	ゼプト	z
10^1	デカ	da	10^{-24}	ヨクト	y

表６．SIに属さないが、SIと併用される単位

名称	記号	SI 単位による値
分	min	1 min=60s
時	h	1h =60 min=3600 s
日	d	1 d=24 h=86 400 s
度	°	1°=(π/180) rad
分	’	1’=(1/60)°=(π/10800) rad
秒	”	1”=(1/60)’=(π/648000) rad
ヘクタール	ha	$1ha=1hm^2=10^4m^2$
リットル	L, l	$1L=11=1dm^3=10^3cm^3=10^{-3}m^3$
トン	t	$1t=10^3$ kg

表７．SIに属さないが、SIと併用される単位で、SI単位で表される数値が実験的に得られるもの

名称	記号	SI 単位で表される数値
電子ボルト	eV	$1eV=1.602\ 176\ 53(14)\times10^{-19}J$
ダルトン	Da	$1Da=1.660\ 538\ 86(28)\times10^{-27}kg$
統一原子質量単位	u	1u=1 Da
天文単位	ua	$1ua=1.495\ 978\ 706\ 91(6)\times10^{11}m$

表８．SIに属さないが、SIと併用されるその他の単位

名称	記号	SI 単位で表される数値
バール	bar	1 bar=0.1MPa=100kPa=10^5Pa
水銀柱ミリメートル	mmHg	1mmHg=133.322Pa
オングストローム	Å	1 Å=0.1nm=100pm=10^{-10}m
海里	M	1 M=1852m
バーン	b	$1\ b=100fm^2=(10^{-12}cm)2=10^{-28}m^2$
ノット	kn	1 kn=(1852/3600)m/s
ネーパ	Np	SI単位との数値的な関係は、対数量の定義に依存。
ベル	B	
デジベル	dB	

表９．固有の名称をもつCGS組立単位

名称	記号	SI 単位で表される数値
エルグ	erg	$1\ erg=10^{-7}$ J
ダイン	dyn	$1\ dyn=10^{-5}$N
ポアズ	P	1 P=1 dyn s cm^{-2}=0.1Pa s
ストークス	St	1 St =$1cm^2$ s^{-1}=$10^{-4}m^2$ s^{-1}
スチルブ	sb	1 sb =1cd cm^{-2}=10^4cd m^{-2}
フォト	ph	1 ph=1cd sr cm^{-2} 10^4lx
ガル	Gal	1 Gal =1cm s^{-2}=$10^{-2}ms^{-2}$
マクスウェル	Mx	1 Mx = 1G cm^2=10^{-8}Wb
ガウス	G	1 G =1Mx cm^{-2} =10^{-4}T
エルステッド(c)	Oe	1 Oe≙ $(10^3/4\pi)$A m^{-1}

(c) ３元系のCGS単位系とSIでは直接比較できないため、等号「 ≙ 」は対応関係を示すものである。

表10．SIに属さないその他の単位の例

名称	記号	SI 単位で表される数値
キュリー	Ci	$1\ Ci=3.7\times10^{10}Bq$
レントゲン	R	$1\ R = 2.58\times10^{-4}C/kg$
ラド	rad	$1\ rad=1cGy=10^{-2}Gy$
レム	rem	$1\ rem=1\ cSv=10^{-2}Sv$
ガンマ	γ	1γ=1 nT=10-9T
フェルミ		1フェルミ=1 fm=10-15m
メートル系カラット		1メートル系カラット = 200 mg = 2×10-4kg
トル	Torr	1 Torr = (101 325/760) Pa
標準大気圧	atm	1 atm = 101 325 Pa
カロリー	cal	1cal=4.1858J（「15℃」カロリー），4.1868J（「IT」カロリー）4.184J（「熱化学」カロリー）
ミクロン	μ	1 μ =1μm=10^{-6}m

（第8版，2006年改訂）

この印刷物は再生紙を使用しています